

AN INVESTIGATION INTO WETTING AND TWO PHASE HEAT TRANSFER ON
REETRANT TEXTURED SURFACES

By

EDWARD MICHAEL MCKENNA III

A DISSERTATION PRESENTED TO THE GRADUATE SCHOOL
OF THE UNIVERSITY OF FLORIDA IN PARTIAL FULFILLMENT
OF THE REQUIREMENTS FOR THE DEGREE OF
DOCTOR OF PHILOSOPHY

UNIVERSITY OF FLORIDA

2011

© 2011 Edward M McKenna III

To my family

ACKNOWLEDGMENTS

I would like to thank my committee especially my advisor Dr. Ronald Baney. Without his patient support, I would not be where I am today. I would also like to thank my group members for making my time working with them relaxing, enjoyable, and educational. I would also like to thank my family for always encouraging me in my education and being there for support. I would especially like to thank my father who was always so proud and supportive of my education. I wish he could have been with me for the end of my academic education. Most importantly, I would like to thank both Ravikumar Vasudevan and Bradley Bon for their collaboration with my doctoral work. Much of our work has been a collaboration, which has resulted in more interesting and educational research. I would also like to thank Dr James Klausner for the use of his lab and for his guidance.

TABLE OF CONTENTS

	<u>page</u>
ACKNOWLEDGMENTS.....	4
LIST OF TABLES.....	7
LIST OF FIGURES.....	8
LIST OF ABBREVIATIONS.....	14
ABSTRACT	15
CHAPTER	
1 INTRODUCTION	17
Introduction to Wetting.....	17
Introduction to Boiling Heat Transfer	26
2 SURFACE FABRICATION.....	33
Design.....	33
Fabrication	39
Characterization and Results.....	42
3 WETTING ON REENTRANT UNDERCUT SURFACE STRUCTURES.....	45
Literature Review	45
Wetting on Ideal Surfaces	46
Wetting on Real Surfaces.....	49
Wetting on Rough and Textured Surfaces.....	51
The Debate over the Validity and Applicability of Wetting Laws	55
Hypothesis and Model.....	59
Calculation of Linear Wetted Fraction	61
Experimental Design.....	63
Contact Angle Measurement	63
Submerged Pressure Threshold.....	64
Results and Discussion.....	66
Contact Angle.....	66
Contact angles as a function of ϕ_{cl}	69
Generalized application to contact angle hysteresis on any surface	75
Breakthrough Pressure	75
Wetting Conclusion.....	79

4	POOL BOILING HEAT TRANSFER ON REENTRANT UNDERCUT SURFACE STRUCTURES	80
	Introduction to Enhanced Boiling Surfaces	80
	Goals	81
	Literature Review	82
	Pool Boiling Apparatus.....	85
	Heater Assembly	85
	Pool Boiling Chamber.....	87
	Data and Image Acquisition.....	88
	Procedure.....	89
	Results and Discussion.....	90
	Size and Spacing Variation	91
	Copper Coating	98
	Etching Variations	98
	Boiling Conclusion	100
5	CONCLUSION AND FUTURE WORK.....	101
APPENDIX		
A	FABRICATION STEPS	102
B	SCANNING ELECTRON MICROSCOPY	104
C	MATLAB CODE	126
D	Φ PLOTS	129
E	BOILING REPRODUCIBILITY	137
	BIBLIOGRAPHY	139
	BIOGRAPHICAL SKETCH.....	146

LIST OF TABLES

<u>Table</u>		<u>page</u>
3-1	Tukey's range test of ANOVA data for breakthrough as a function of etch profile.....	77
2-1	Variations in dry etching conditions.	103

LIST OF FIGURES

<u>Figure</u>	<u>page</u>
1-1 Contact angles (θ) for non-wetting droplet (A) through highly wetting droplet(C).....	18
1-2 How air composite surfaces decrease wetting.....	20
1-3 Simulated droplet on a solid surface.....	21
1-4 As the volume of a droplet is increased, the contact line will become pinned at edges resulting in an increase in contact angle from equilibrium.....	22
1-5 Three-dimensional rendering of the type of discrete reentrant structure used in this work.....	23
1-6 Number of times cited per year for three of the most commonly cited papers in the field of wetting.....	26
1-7 Idealized boiling curve	27
1-8 Film boiling after surpassing the critical heat flux on smooth silicon.....	28
1-9 Expected mechanisms of boiling enhancement on discrete reentrant structures.....	31
1-10 Conditions for a stable vapor pocket at temperatures less than the boiling point.....	32
2-1 SEM image of one of the patterns produced in this work	33
2-2 Radial symmetry in regular two-dimensional shapes.....	34
2-3 Plan view representation of a hexagonal array of surface structures	36
2-4 Interface curvature as a function of the gap between structures	36
2-5 Range of receding contact angles produced by surfaces in this work	37
2-6 Schematic of planned etch variations.....	38
2-7 Schematic of the fabrication process for surfaces composed of discrete reentrant surface structures.....	40
2-8 To scale schematic of actual height and undercut for each of the etch variations	43
2-9 Plot of the undercut and height variations for the 10 μ m pattern cross section ...	44

3-1	Components of Young's contact angle	46
3-2	Basis of local derivation of Young's equation not taking into account the non-local effects of altering the length of the three-phase line.....	48
3-3	Alteration of the droplet surface with an increase in the length of the three-phase line	49
3-4	Line energy as calculated by Tadmor	50
3-5	Graphic representation of surface energy minimization according to Cassie and Baxter	52
3-6	Contributions to the surface energy from molecular scale variations and structure	60
3-6	Cad generated image (compressed from ~68 million pixels) of a surface based on SEM measurements	61
3-7	Zoomed in plot of ϕ_{cl} and mock hexagonally structured surface.....	63
3-8	Side view of breakthrough pressure apparatus	65
3-9	Pressure apparatus during a run	65
3-10	Contact angle versus cap size at 3 μ m spacing.	67
3-11	Contact angle versus spacing at 20 μ m feature width.	68
3-12	20 μ m cap size spaced by 6 μ m ϕ -plot.....	70
3-13	Average receding contact angle versus the ratio between spacing and cap width, compared to predictions for the variation in cap size	71
3-14	Average receding contact angle versus the ratio between spacing and cap width, compared to predictions for the variation in spacing	72
3-15	Comparison of predictions to data for the square, star and inverse patterns.....	73
3-16	Goodness of fit comparison (R^2) of all data points compared to the predictions	74
3-17	Average breakthrough pressure for 30-100 μ m cap sizes.....	76
3-18	Initial and final breakthrough pressures for the four patterns with the highest breakthrough	78
3-19	Final breakthrough of the three patterns with the highest pressures	78

4-1	Heater Assembly	86
4-2	Pool boiling chamber	88
4-3	Boiling curves for the enhanced surfaces produced by Honda and Wei, Anderson and Mudawar, and O'Connor	91
4-4	Boiling curves for the various cap sizes at a constant spacing of 3 μ m.	92
4-5	Expected trends as a function of the measured cap sizes with constant spacing of 3 μ m	92
4-6	Heat transfer coefficient for constant cap size at three different heat fluxes as a function of the number of cavities on the surface.	93
4-7	Expected trends in boiling as a function of spacing.	94
4-8	Boiling curves for the variation in spacing with 20 μ m cap size	95
4-9	Heat transfer coefficient for constant spacing at three different heat fluxes as a function of the number of cavities on the surface.	95
4-10	Critical heat flux variation as a function of cap size. No trend is apparent.	96
4-11	Improvement in CHF as a function of spacing for the 20 μ m cap size	97
4-12	Images taken with long shutter lengths, of boiling near the critical heat flux	97
4-13	Boiling curves for the 20 μ m cap size spaced by 3 μ m with and without a copper coating	98
4-14	Boiling curves for the etching variations.	99
A-1	Standard 20x20 μ m square pattern	104
A-2	Standard 10 μ m cap size with 3 μ m spacing in tilted view	104
A-3	Standard 20 μ m cap size with 3 μ m spacing	105
A-4	Standard 60 μ m cap size with 3 μ m spacing	105
A-5	Tall 10 μ m cap size with 3 μ m spacing, cross section	106
A-6	Short 10 μ m cap size with 3 μ m spacing, cross section	106
A-7	Less undercut 10 μ m cap size with 3 μ m spacing, cross section	107
A-8	No undercut 10 μ m cap size with 3 μ m spacing, cross section	107

A-9	Standard 10 μ m cap size with 3 μ m spacing, cross section with 500nm thick caps.....	108
A-10	5 μ m cap size with 3 μ m spacing, plan view.....	108
A-11	5 μ m cap size with 3 μ m spacing, plan view (2)	109
A-12	10 μ m cap size with 3 μ m spacing, plan view (short)	109
A-13	10 μ m cap size with 3 μ m spacing, plan view (2) (short).....	110
A-14	10 μ m cap size with 3 μ m spacing, plan view (3) (short).....	110
A-15	20 μ m cap size with 3 μ m spacing, plan view (standard).....	111
A-16	20 μ m cap size with 3 μ m spacing, plan view (2) (standard)	111
A-17	20 μ m cap size with 3 μ m spacing, plan view (3) (standard)	112
A-18	20 μ m cap size with 3 μ m spacing, plan view (4) (short)	112
A-19	20 μ m cap size with 3 μ m spacing, plan view (5) (short).....	113
A-20	30 μ m cap size with 3 μ m spacing, plan view (standard).....	113
A-21	30 μ m cap size with 3 μ m spacing, plan view (2) (short)	114
A-22	40 μ m cap size with 3 μ m spacing, plan view (standard).....	114
A-23	40 μ m cap size with 3 μ m spacing, plan view (2) (short).....	115
A-24	60 μ m cap size with 3 μ m spacing, plan view (standard).....	115
A-25	60 μ m cap size with 3 μ m spacing, plan view (2) (short)	116
A-26	80 μ m cap size with 3 μ m spacing, plan view (standard).....	116
A-27	80 μ m cap size with 3 μ m spacing, plan view (2) (short)	117
A-28	100 μ m cap size with 3 μ m spacing, plan view (standard)	117
A-29	100 μ m cap size with 3 μ m spacing, plan view (2) (short)	118
A-30	20 μ m cap size spaced by 6 μ m plan view (standard).....	118
A-31	20 μ m cap size spaced by 6 μ m plan view (2) (short)	119
A-32	20 μ m cap size spaced by 12 μ m plan view (standard).....	119
A-33	20 μ m cap size spaced by 12 μ m plan view (2) (short)	120

A-34	20 μ m cap size spaced by 24 μ m plan view (standard).....	120
A-35	20 μ m cap size spaced by 24 μ m plan view (2) (short)	121
A-36	20 μ m cap size spaced by 48 μ m plan view (standard).....	121
A-37	20 μ m cap size spaced by 48 μ m plan view (2) (short)	122
A-38	20 μ m cap size spaced by 96 μ m plan view (standard).....	122
A-39	20 μ m cap size spaced by 96 μ m plan view (2) (short)	123
A-40	Standard 20x20 μ m square cap plan view.....	123
A-41	Star cap plan view	124
A-42	Star cap plan view (2).....	124
A-43	Inverse pattern plan view.....	125
B-1	5 μ m ϕ -plot.....	129
B-2	10 μ m ϕ -plot.....	129
B-3	20 μ m ϕ -plot.....	130
B-4	30 μ m ϕ -plot.....	130
B-5	40 μ m ϕ -plot.....	131
B-6	60 μ m ϕ -plot.....	131
B-7	80 μ m ϕ -plot.....	132
B-8	100 μ m ϕ -plot.....	132
B-9	20 μ m cap size spaced by 12 μ m ϕ -plot.....	133
B-10	20 μ m cap size spaced by 24 μ m ϕ -plot.....	133
B-11	20 μ m cap size spaced by 48 μ m ϕ -plot.....	134
B-12	20 μ m cap size spaced by 96 μ m ϕ -plot.....	134
B-13	20 μ m cap size spaced by 20 μ m square ϕ -plot.....	135
B-15	20 μ m square equivalent inverse ϕ -plot	136
D-1	Three run repeatability for the 20 μ m cap size with 300 and 500 μ m caps.....	137

D-2	Two run repeatability for the 30µm cap size	137
D-3	Two run repeatability for the 40µm cap size	138
D-4	Two run repeatability for the 60µm cap size	138

LIST OF ABBREVIATIONS

CHF	Critical heat flux
DRIE	Deep reactive ion etching
HTC	Heat transfer coefficient
ICP	Inductively coupled plasma
ONB	Onset of Nucleate Boiling
φ_{CL}	The fraction along the contact line of a droplet that contacts the solid
PEEK	Polyether ether ketone
RIE	Reactive ion etching
SEM	Scanning electron microscopy

Abstract of Dissertation Presented to the Graduate School
of the University of Florida in Partial Fulfillment of the
Requirements for the Degree of Doctor of Philosophy

AN INVESTIGATION INTO WETTING AND TWO PHASE HEAT TRANSFER ON
REETRANT TEXTURED SURFACES

By

Edward McKenna

August 2011

Chair: Ronald Baney

Major: Materials Science and Engineering

A novel pattern of undercut nano/microscopic surface features has been developed. These patterns feature simple hexagonally periodic surface composed of a Silicon stem and a thin Silicon Dioxide Cap.

The first task of this work was to measure wetting properties including advancing, receding and sessile contact angles as well as breakthrough pressure. These results were used to create a model based on the fraction of the droplet periphery that wets the surface, as opposed to using the entire fraction of wetted surface area beneath a droplet. This model predicts contact angles more accurately than existing equations. These equations, specifically Cassie's and Wenzel's law, are in common use even though some of their basic underpinnings are debated to be fundamentally flawed. The results of this work will also act to clear up this ongoing debate.

The second task was to test the hypothesis that these periodic undercut patterns could be used as a more efficient nucleate boiling surface due to vapor trapping and liquid entrainment into the network of structures. This type of liquid entrainment effect was expected to be similar to that previously proposed to explain the enhanced boiling on pore and tunnel type surfaces. However, these surfaces can be produced on a

smaller scale, which adds to the liquid entrainment by enhancing capillary wicking. The result was a significant increase in critical heat flux due to small vortices pulling liquid into the surface. The parametric variations in the surfaces provided insight into the size scales that will maximize the intended effects. The influence of feature height, depth of undercut, cap thickness, size and spacing were all determined.

CHAPTER 1 INTRODUCTION

Chapter 1 is intended to define reentrant cavities, describe the type of reentrant surfaces used in this work, and explain how they are useful and related to the two objectives of this work (wetting and pool boiling). Chapter 1 will also introduce the topics of wetting and pool boiling. Chapter 2 will discuss the fabrication and characterization of these surfaces. Reviews of the literature, results, and discussion of the wetting and boiling work will be discussed in Chapters 3 and 4 respectively.

A reentrant cavity is one whose inner surfaces surpass a 90° angle to the plane of the surface (see Figures 1-3 and 1-4). Reentrant cavities can be useful in both non-wetting applications and for vapor trapping for wetting fluids in pool boiling.

Introduction to Wetting

The degree of wetting is the measured angle at which the liquid resides in reference to the solid, called contact angle. If the contact angle is large, there is little solid-liquid contact, therefore the conditions are non-wetting. As the contact angle decreases, and the solid-liquid contact increases, the conditions become wetting (Figure 1-1). The contact angle will depend on a balance between the adhesive and cohesive forces within the system.

High and low energy solid surfaces. When dealing with wetting, solid surfaces are traditionally broken down into two categories, high energy and low energy. The energy of a solid surface is related to the bulk nature of the solid. High-energy solids generally include hard materials with ionic, covalent, or metallic bonds. It takes a relatively large amount of energy to break these bonds and thus the surface produced is at a high-energy state. Low energy solids include materials that are held together by

weak forces such as hydrogen bonds or Van der Waals bonds. This weak bonding requires relatively little force to break resulting in a surface in a low energy state. Most high-energy surfaces are easily wet by most fluids where as low energy surfaces (depending on the fluid) display a range of wettability, from full wetting to almost completely non-wetting. When dealing with water low energy surfaces can be referred to as hydrophobic and high energy surfaces as hydrophilic.

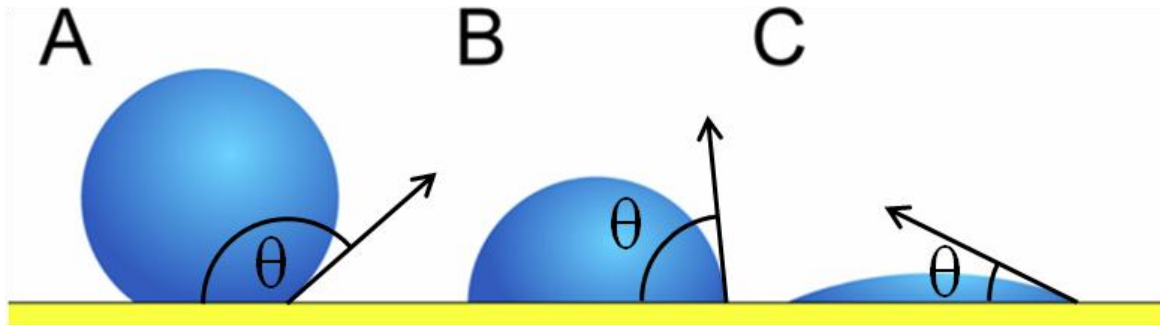


Figure 1-1. Contact angles (θ) for non-wetting droplet (A) through highly wetting droplet(C).

Traditionally surfaces with a 0° contact angle are referred to as fully wetting, between 0° and 90° as partially wetting and greater than 90° as non-wetting or hydrophobic surfaces. Special surfaces that are designed to be highly non-wetting for water are called superhydrophobic if their contact angle with water is defined as greater than 150° . There are also highly wetting fluids, which will completely wet the surface of many solids.

Contact angles and contact angle hysteresis. On an ideal surface as shown in Figure 1-1, the contact angle is only a function the surface energy (or surface tension) of the three interfaces involved. However, droplets on real surfaces can display a range of contact angles. Only two angles can actually be measured, the advancing and receding. The advancing angle is measured by inserting a needle into the droplet and

slowly increasing the volume. As the volume is increased, the contact angle will increase until it reaches the advancing angle. Any further increase in volume of the droplet at this point will result in the contact line (see Figure 1-3) of the droplet increasing and the contact angle relaxing. The same method can be applied for measuring the receding contact angle with removal of fluid from the droplet instead of addition. The dynamics of these contact angles and their hysteresis will be the focus of this work.

Why is non-wetting important and how is it achieved? Non-wetting surfaces find use due to their ability to stay dry, reduce adhesion, and allow for fluids to easily bead and roll off them. The design and manufacture of non-wetting surfaces has become important due to their use in painting, drying, heat transfer, adhesion, corrosion, biofilm formation and for practical purposes such as water beading windows. One example is that the wettability of a surface affects the radius of curvature of droplets. The radius of curvature can be related to vapor pressure and evaporation rates through the Young-Laplace equation. The difference between the advancing and receding contact angles and their magnitudes can be related to the angle at which drops roll off a surface[1]. Another example is researchers tuning the wettability of surfaces to allow for a mixture of hydrocarbons and water to be poured over a material the beads the water away and allows the hydrocarbon to drip through [2, 3].

The typical pathway to producing non-wetting surfaces is by altering the chemistry of the solid surface to reduce surface energy. The lower surface energy results in a higher contact angle and thereby less wetting. Further, new techniques have recently begun to be applied in composite surfaces. By producing a surface with wetted areas

and air pockets, which have an extremely low surface energy, the total surface energy is reduced. For the same solid surface, replacing a fraction of the solid with air will significantly decrease the surface energy per area and produce larger contact angles tending towards non-wetting surfaces. Figure 1-2 illustrates this principle.

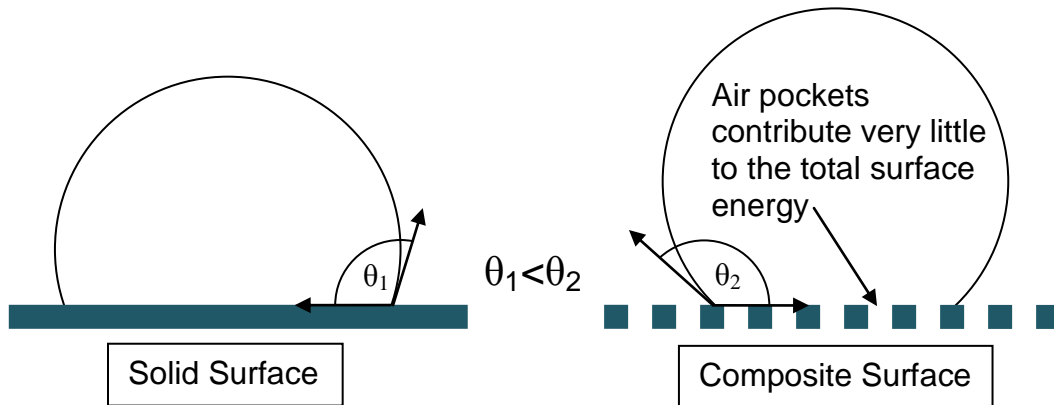


Figure 1-2. How air composite surfaces decrease wetting. A solid has excess surface energy due to unsatisfied bonds at the surface. An interface composed of solid and air patches will reduce this total energy per unit area resulting in a lower total surface energy and less wetting by liquid droplets.

While this principle has been applied in the past, this work improves upon the theory originally produced by Wenzel for rough surfaces and Cassie and Baxter for structured surfaces. Their original proposals focused on the area under the droplet. However, this work will show that it is the perimeter of the wetted area that controls wetting. To illustrate, Figure 1-3 shows a droplet on a surface. The arrows point to the perimeter, referred to as the triple point line. A detailed analysis will follow in Chapter 3.

How is wetting affected by reentrance? When the contact line of a droplet approaches the edge of a cavity (or air pocket) on a non-wetting surface it becomes pinned. This is seen in Figure 1-4. Both the left and right part of the diagram show a droplet whose volume is being increased. The forces that are important for this discussion are the additional hydrostatic pressure (which tends to expand the droplet

and increase the diameter of the contact line) and the surface tension of the liquid-vapor interface acting in both the vertical and horizontal directions

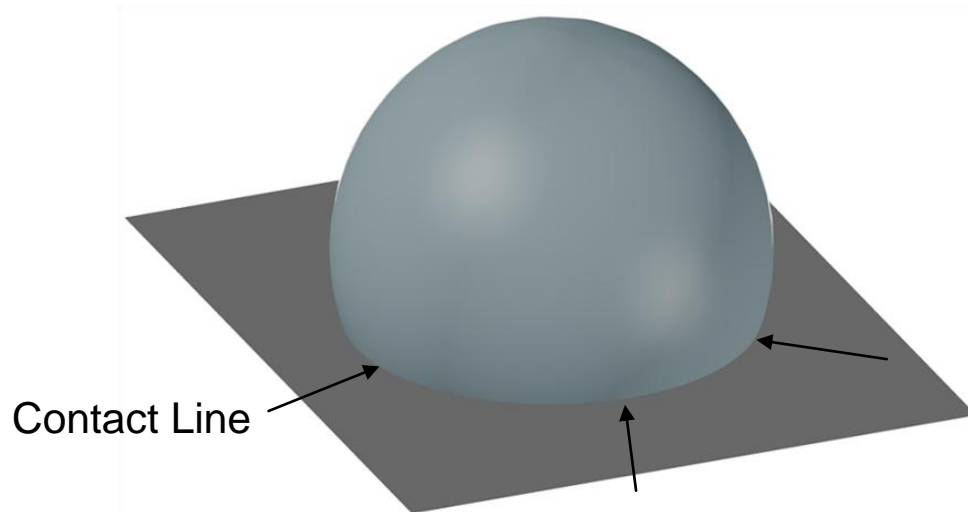


Figure 1-3. Simulated droplet on a solid surface. The contact line of a droplet (sometimes referred to as the three-phase contact line) is the intersection of the droplet and the plane of the surface. In the case of structured surfaces discussed later, a portion of this contact line can lie over air pockets.

While not a rigorous definition, it is common to imagine the surface tension of the fluid as a force per unit length. This force can be thought of as acting on the contact line of a droplet, which can be broken down into horizontal and vertical component forces. When the contact line reaches an edge, the vertical component of the liquid-gas surface tension will prevent it from moving. An increase in hydrostatic pressure due to the addition of fluid causes an increase in the contact angle from the equilibrium angle. As the tangent to the liquid-vapor interface (at the intersection with the solid surface) approaches horizontal, there will no longer be a vertical component to the surface tension and the non-reentrant cavity will begin to wet. The reentrant cavity however will still have a pinned three-phase line. This is due to the cavity geometry only allowing the contact line to move back toward the center of the droplet, which is countered by the

horizontal component of fluid surface tension. A similar description was provided by Bormashenko[4]. Chapter 3 will discuss the modeling of contact angles measured on surfaces composed of discrete reentrant structures where the shape, size and spacing of the structures has been investigated.

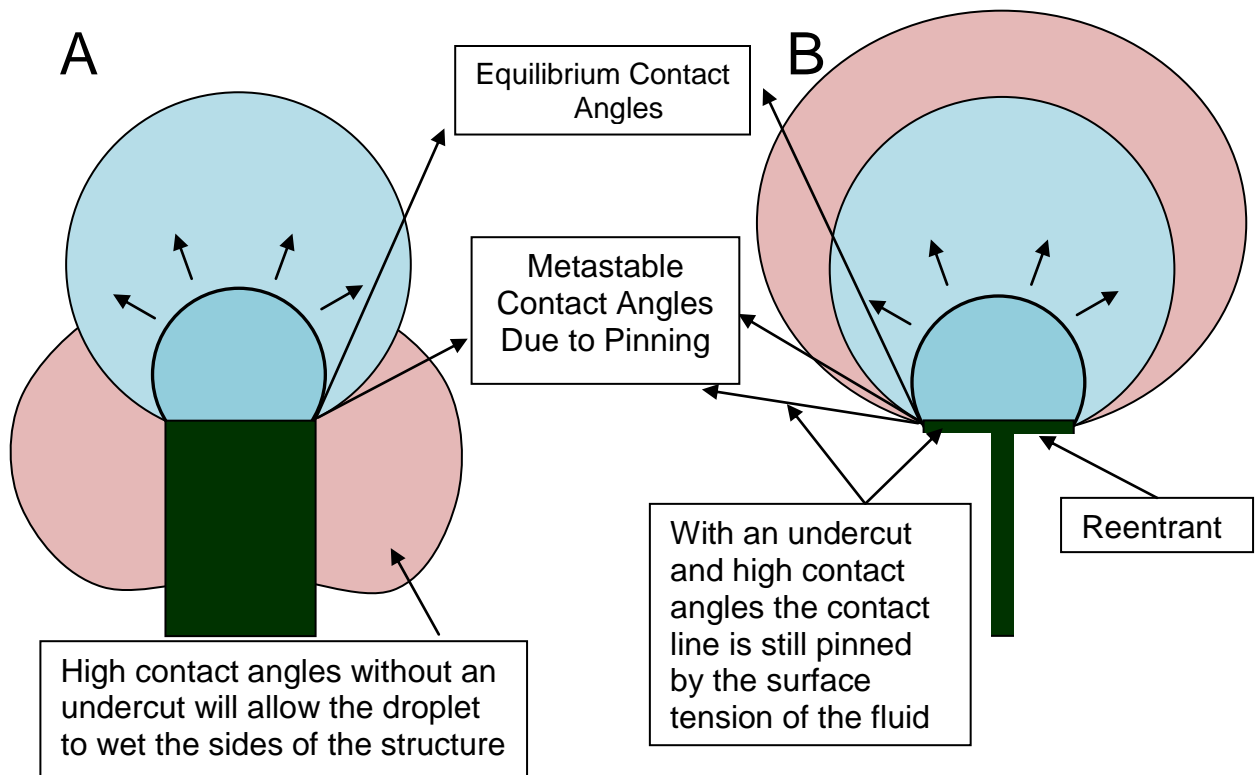


Figure 1-4. As the volume of a droplet is increased, the contact line will become pinned at edges resulting in an increase in contact angle from equilibrium. A) The sides of a non-reentrant structure become wetted as the contact angle nears 180° . B) For reentrant structures the surface tension acts oppositely to the only direction the contact line can move.

What type of discrete reentrant structures are being used in this work? In this study, surfaces are composed of between approximately 20,000 and 2,000,000 discrete reentrant structures. Each structure can be idealized as a nearly cylindrical stem with a very thin cap on it, as shown in Figure 1-5. These structures are created by depositing a thin film of SiO_2 and then removing the non-cap area using plasma etching

that only affects the SiO_2 . Anisotropic plasma etching is then used to etch down around the caps and an isotropic plasma etch is used to thin the stem. Both of these etch plasmas etch Si but not the SiO_2 caps. The detailed fabrication process for these structures is explained in Chapter 2 and the actual process recipe can be found in Appendix A.

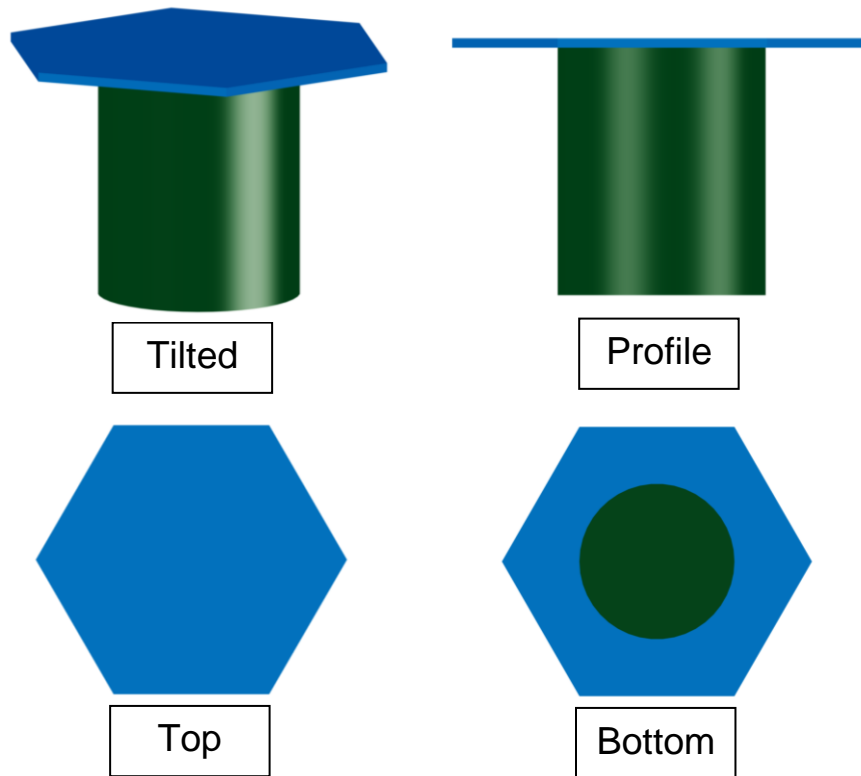


Figure 1-5. Three-dimensional rendering of the type of discrete reentrant structure used in this work. Structures are composed of a nearly cylindrical Si stem and a thin (300-500nm) cap made of SiO_2 .

What can be achieved by using well defined, flat capped, reentrant surfaces for non-wetting? Any wetting model used for composite surfaces (including air-solid, solid-solid etc.) will in some way be based on the fraction of the liquid-solid surface that encounters each component. By using a well-defined flat surface (see Figure 2-1); the calculation of the fraction of each component encountered by droplet becomes simple.

The use of reentrant geometry ensures that the surface will maintain the non-wetted state. The result being a surface that maintains a non-wetted state and has a well defined wetted fraction (calculated at either the contact line or the entire area of the droplet-solid surface) that can be used to test various models. The modeling of wetting on these surfaces will allow for the production of a significantly improved model to predict contact angles. It will also provide a concrete demonstration that proves that the accepted way wetting is taught and understood is invalid and that the energy of the contact line, not the area around the contact line or the area beneath a droplet affects its contact angle.

Why is it important to produce a more accurate model for non-wetting surfaces? Understanding the wetting of liquid on a solid surface is very important from the point of view of various biological and physical applications. These include painting, drying, heat transfer, adhesion, corrosion, microfluidic devices, biofilm formation[5]. This understanding is also important practically for the production of surfaces that have found many uses from waterproofing to water beading windows that help drivers to see during rain showers. Currently the majority of researchers rely on the Cassie-Baxter equation or the Wenzel equation (referred to as Cassie's and Wenzel's Laws) for prediction of contact angles on surfaces. These equations are based on using the fraction of the contact area underneath a droplet that contacts the solid surface. Results based on this method have been shown to be valid only in describing the equilibrium apparent contact angle if the droplets size and position were averaged over the whole surface. An example of a problem this can create would be if someone were to design a surface with a regular repeating pattern of a shape. Knowing the area of the shape and

the number of shapes per area would be all that is required to calculate the contact angle based on the Cassie-Baxter equation. In this work, it will be shown that if the area of the shape used was maintained, but the shape was changed in a way that spread the area out the contact angle would actually change. This results in researchers using often-inapplicable equations to predict contact angle when designing surfaces.

This issue is made further relevant as over the past decade, research on wetting topics has become increasingly popular. This is in part due to the ubiquitous nature of wetting but can be mostly attributed to the current popularity of superhydrophobicity. The popularity of superhydrophobicity began to take off in part due to attention brought to the naturally superhydrophobic surface of the lotus leaf by Barthlott in 1997[6]. Other authors began to investigate other naturally superhydrophobic surfaces such as water strider legs[7] and the wings of Cicada Orni[8] in 2004. This trend is shown in Figure 1-6 where the number of citings per year of the three most cited papers in the wetting field are plotted. Wenzel and Cassie's papers were cited 612 times from their publishing (1936 and 1944 respectively) through 2000 and 3,000 times in the last decade. This increase in popularity has correspondingly increased the need for accurate prediction methods of water repellency.

Goals. The specific goals of this work concerning wetting are to first provide concrete evidence that the use of the Wenzel or Cassie-Baxter equation should not be considered valid under any circumstance, although they may be used for simplicity as an approximation in many cases. Second, is to produce a modified version of these equations that is based on a fundamentally sound model that produces results that are

more accurate. Third, is to provide a simple method of numerically calculating the necessary parameters.

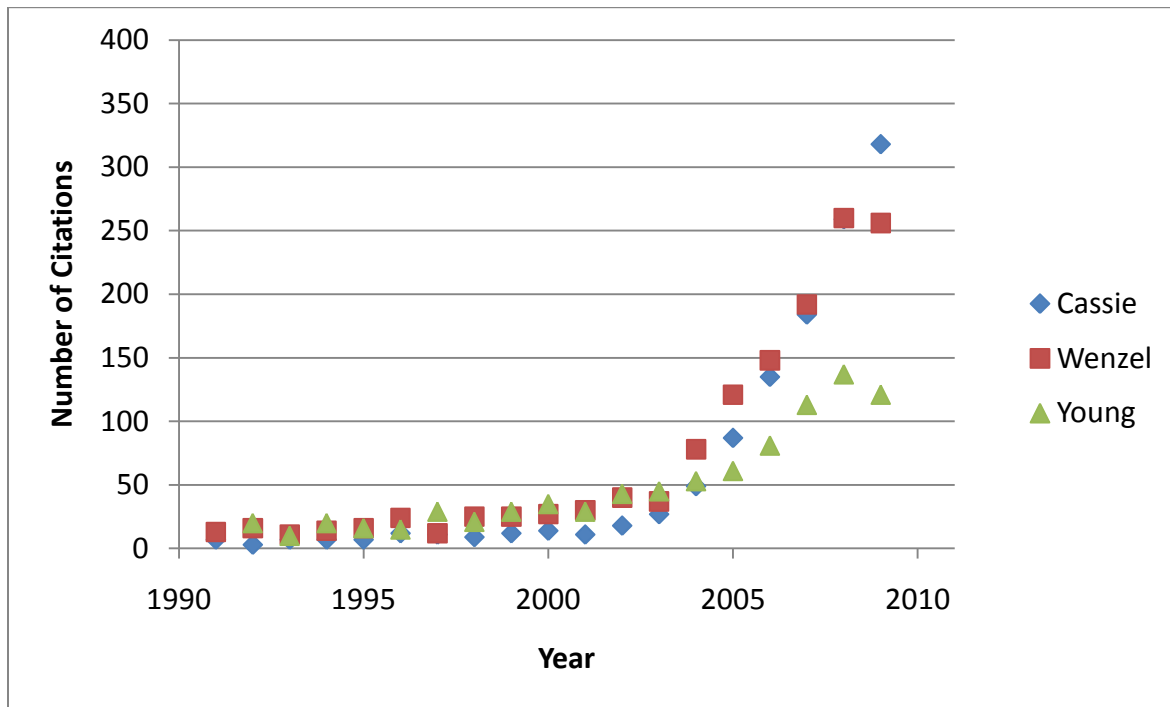


Figure 1-6. Number of times cited per year for three of the most commonly cited papers in the field of wetting [9-11]

Introduction to Boiling Heat Transfer

Why is pool boiling important? Pool boiling is a highly effective form of heat transfer that includes phase change (vaporization of a fluid) and subsequent convection of the vapor bubble away from the surface. Pool boiling is used to transport heat in many applications that require high heat flux such as electronics, nuclear reactors, and refrigerators. Another important application is cooling of computer chips. As transistors shrink and integrated circuits become more densely packed, the heat flux also increases. If the heat can be removed fast enough, the speed of the computer chip can be increased. The use of enhanced pool boiling heat transfer surfaces may provide a cooling solution to meet these demands. Research on enhanced boiling surfaces for

use in electronics cooling is focused on reduction of the temperature required to initiate boiling, maximizing critical heat flux (CHF) and on improving the slope of the boiling curve (see Figure 1-7 and the associated paragraph on boiling curves).

To introduce pool boiling, the basic heat transfer regimes and the boiling curve will be discussed. Then the basic parameters and the effects they have on boiling will be discussed to help describe why boiling is one of the most complex systems studied. Finally, those parameters that are of specific interest to this work will be discussed.

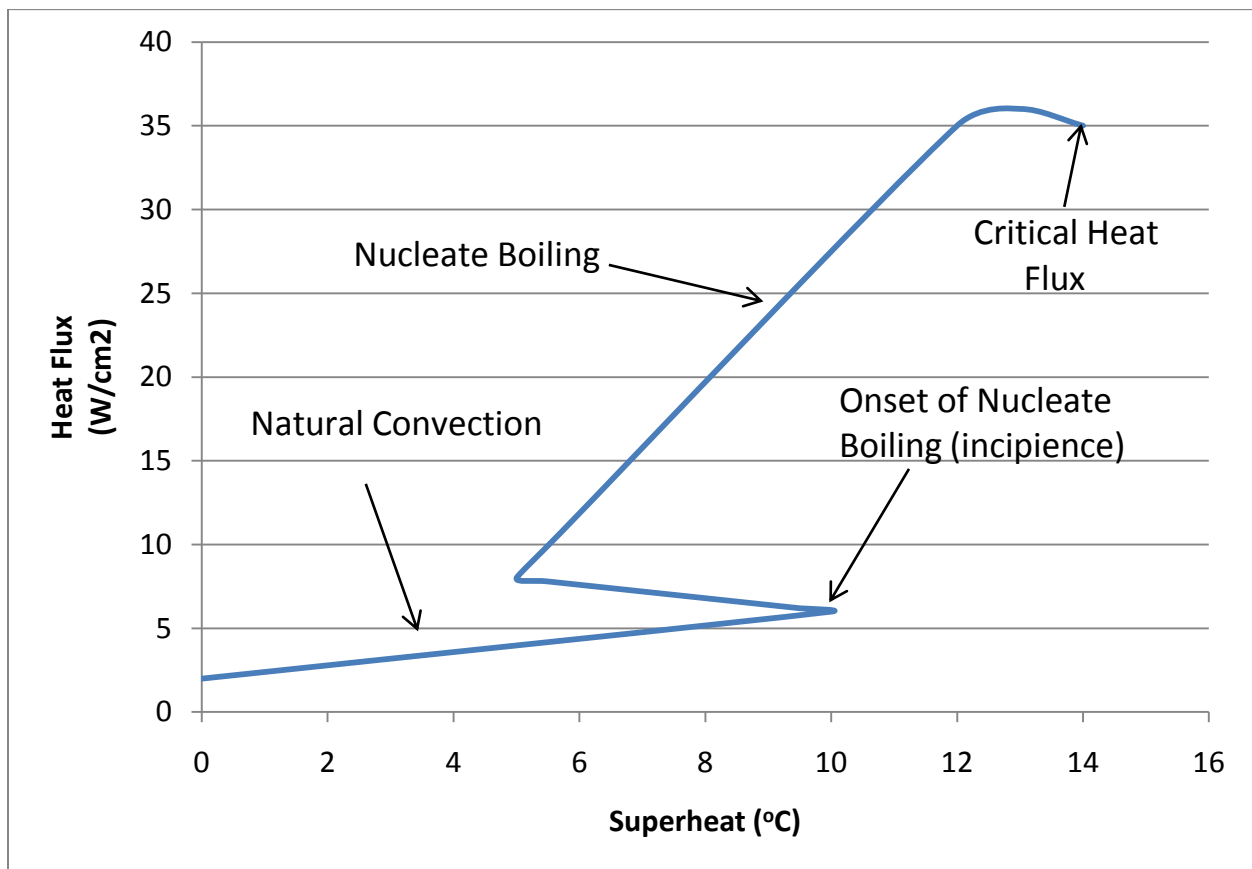


Figure 1-7. Idealized boiling curve. A plot of heat flux as a function of surface temperature can be analyzed to find the slope of heat flux versus surface temperature in the natural convection regime, the temperature at which stable vapor bubbles are first produced, the slope of the heat flux versus surface temperature for the nucleate boiling regime, and the critical heat flux. In a real boiling curve, there may be variation in the slopes.

Boiling curves. Boiling curves are standard plots of heat flux (ordinate) and superheat (abscissa). Superheat is the excess temperature above the boiling point. A standard boiling curve is shown in Figure 1-6. As shown in the diagram boiling curves have a number of distinct transition points and regimes. Upon initial heating, there is only natural convection, which requires large increases in surface temperature to increase the heat flux. Natural convection will continue until the onset of nucleate boiling (ONB). Nucleate boiling is a much more effective form of heat transfer and brings with it a drop in surface temperature and an increase in the slope of the heat flux versus superheat curve. This regime will continue until the vapor bubbles become large enough to coalesce at the surface into a film (the critical heat flux). The film will prevent fluid from reaching the surface and result in significantly diminished vapor productions as shown in Figure 1-8.

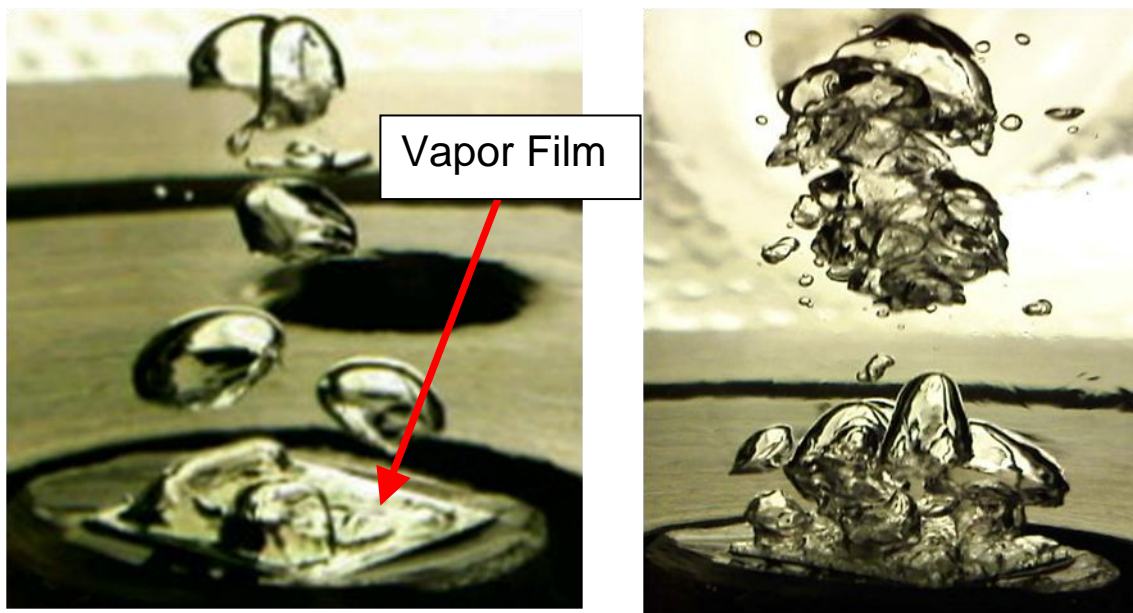


Figure 1-8. Film boiling after surpassing the critical heat flux on smooth silicon.

This will insulate the surface and significantly degrade the heat transfer causing a large drop in heat flux. The temperature on the surface will continue to increase until thermal

conductivity through the vapor phase can accommodate the required heat flux. This temperature can be very high relative to the boiling regime and may result in melting or unacceptable temperatures in the surface.

The fundamental parameters of pool boiling. The process of boiling is complex and is based on properties of both the working fluid and the heating surface. These properties and their effects are:

- Shape of cavities, size of cavities, equilibrium contact angle of the fluid and surface tension affect both the nucleation and trapping of vapor on the surface
- The number and distribution of cavities on a surface affect the number of vapor producing sites on the surface
- The surface tension of the liquid-gas interface affects bubble coalescence along the surface
- The thermal conductivity and structure of the surface affects the kinetics of lateral reheating of the cold spot left due to the creation of a bubble
- The contact angle of the bubble on the surface will affect the bubble departure dynamics
- Surface structure and thermal diffusivity, heat capacity and viscosity of the fluid affect flow patterns near the surface. Additionally density of bubbles on the surface, production frequency and size of bubbles and all of the properties that cause these effects all effect surface flow patterns by creating wake fields as the bubbles depart
- The wake field and all the properties that effect it will result in cool liquid from the bulk flowing toward the surface
- Bulk temperature of the fluid, surface temperature and thermal conductivity affect the thermal gradient of the fluid near the surface, which intern affects the bubble growth dynamics (for example if a bubble grows large enough to reach a cooler portion of the liquid it will begin to condense)
- Size of the heater affects the degree in which the disturbances caused by a single cavity affect the entire boiling curve

Details concerning these parameters and their affect on boiling can be found in "Liquid-Vapor Phase-Change Phenomena" by Carey[12].

This work focuses on a parametric study of discrete reentrant surfaces. The parameters of interest are the number of cavities on the surface, the size of cavities on the surface, and the effects of the shapes of the structures that make up the cavities.

Why are reentrant cavities important for boiling? Reentrant cavities are commonly discussed in pool boiling literature due to their ability to maintain a stable vapor pocket at temperatures lower than the saturated temperature. When wetting fluids (contact angle less than 90°) are boiled on non-reentrant surfaces, the fluid will flood all of the cavities when the temperature drops below the boiling point of the fluid. This is due to the increased pressure in the vapor pocket causing the pocket to continue condensing until there is no more vapor. Alternatively, if the fluid has a contact angle greater than 90° or the cavity is sufficiently reentrant, the pressure in the vapor pocket will be less than the surrounding fluid as shown in Figure 1-10. This will lead to a stable vapor pocket. This was first investigated by Griffith and Wallis[13] in 1958. A stable vapor pocket primarily benefits boiling because there is no need to nucleate vapor after the surface has been cooled.

Why use discrete reentrant structures instead of surfaces with reentrant cavities? The surfaces in this work are not covered in reentrant cavities; they are covered in discrete reentrant structures. It is expected that the suction created by rising droplets will create suction in the sub surface network formed by the structures (see Figure 2-1). This will induce liquid entrainment that will benefit boiling and increase the maximum heat flux in the boiling regime. This is similar to the effect described by Das for surfaces composed of pores and subsurface tunnels[14]. These types of surfaces have been shown to produce large enhancements in boiling performance [15-17]. The

enhanced liquid entrainment will benefit boiling by supplying liquid to the stems of the structures. The thin film area near the three-phase line of the stems is where vaporization actually occurs in boiling. Adding structures to the surface can also help to improve fluid supply by increasing wicking[18]. It is expected that the combination of wicking, liquid entrainment, and enhanced vapor trapping will enhance heat transfer. To compare boiling on discrete structured surfaces a couple of parameters have to be compared. The location of vapor nucleation will be assumed to be along the floor of the structure between three stems. This is because as the structures are heated, they will conduct heat into the fluid. The location between three structures will experience the highest flux of heat from the surface and structures and therefore have the highest driving force for creating stable vapor nuclei. This is shown in figure 1-9

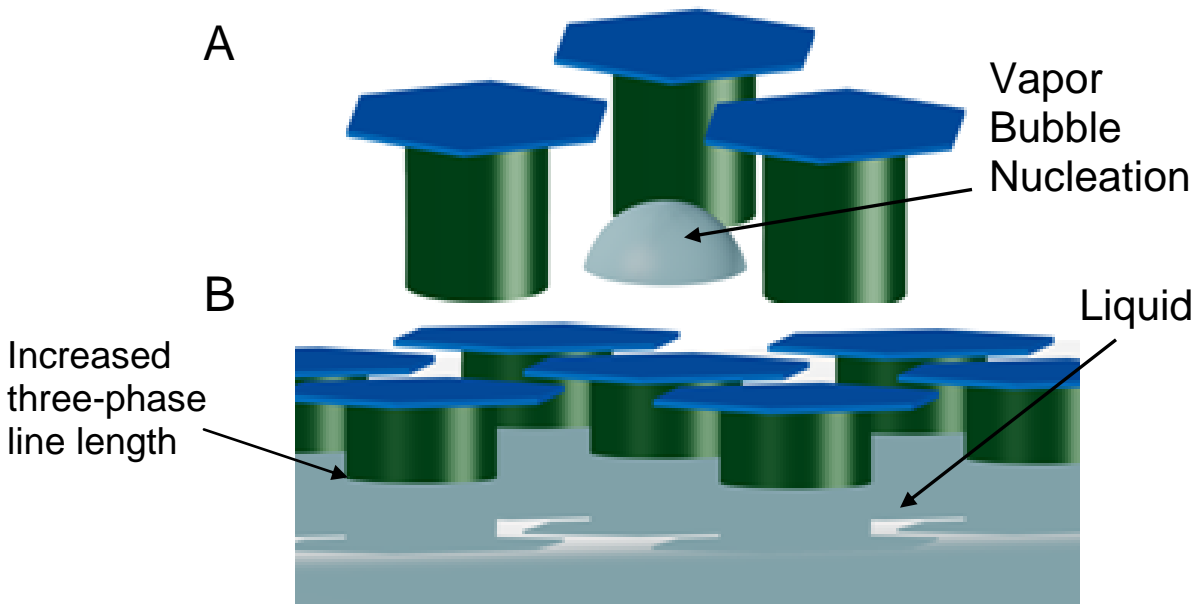


Figure 1-9. Expected mechanisms of boiling enhancement on discrete reentrant structures. A) It is expected that bubbles will nucleate near the surface between three structures. B) Enhancement in the nucleate boiling regime is expected due to the large increase in length of the three-phase contact line where vaporization takes place.

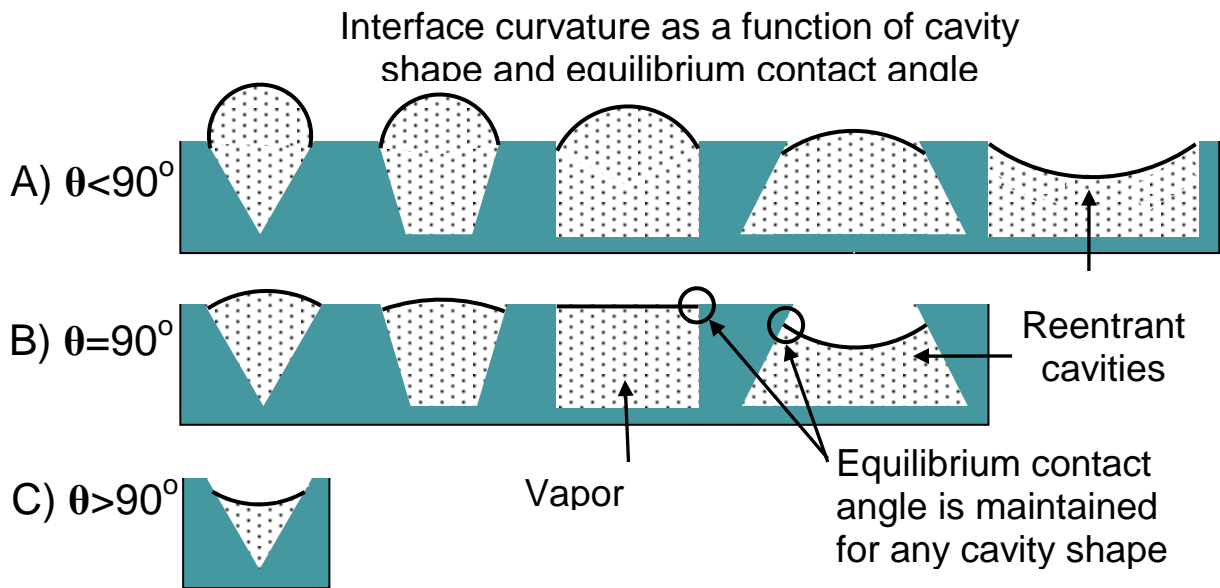
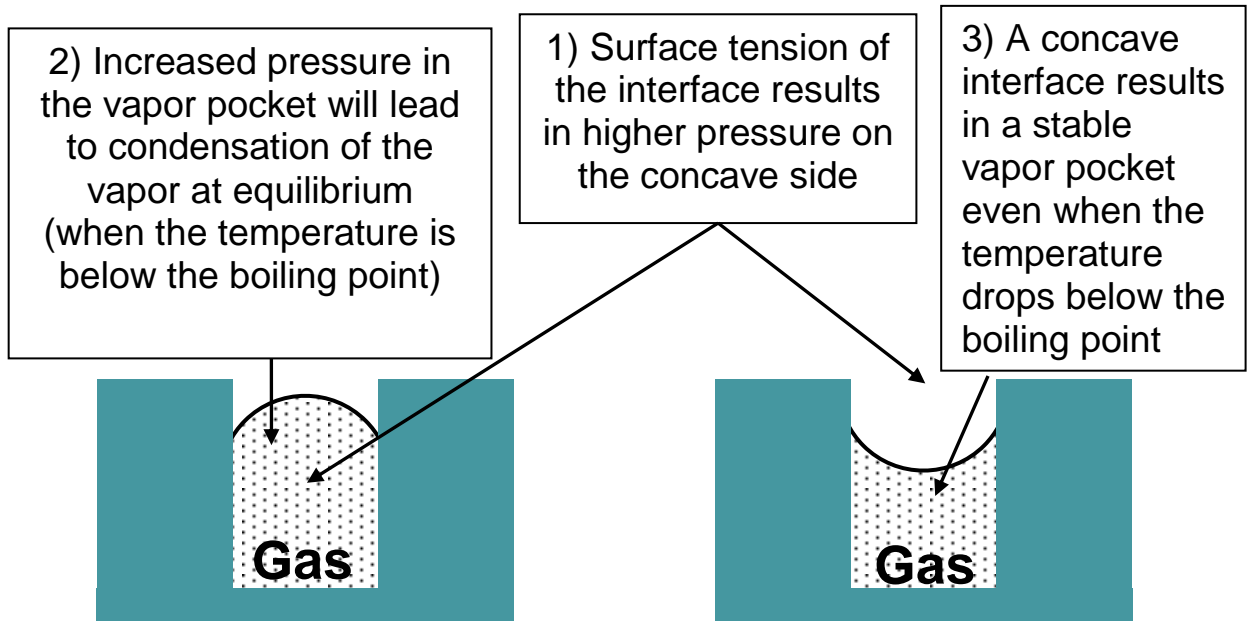


Figure 1-10. Conditions for a stable vapor pocket at temperatures less than the boiling point. Having vapor already trapped on the surface allows boiling heat transfer to start at the boiling point as opposed to requiring higher temperatures to nucleate vapor.

CHAPTER 2 SURFACE FABRICATION

Design

In Chapter 2, the fabrication of surfaces composed of discrete reentrant structures will be discussed. Figure 2-1 illustrates a reentrant surface produced in this work. This structure is a hexagonal cap attached to a stem. The dark spots in the center of each structure are due to electrons penetrating into the stems where as the lighter areas are thin and easily reflect electrons. These fabrication methods and results inform both the wetting work discussed in Chapter 3 and the pool boiling work discussed in Chapter 4.

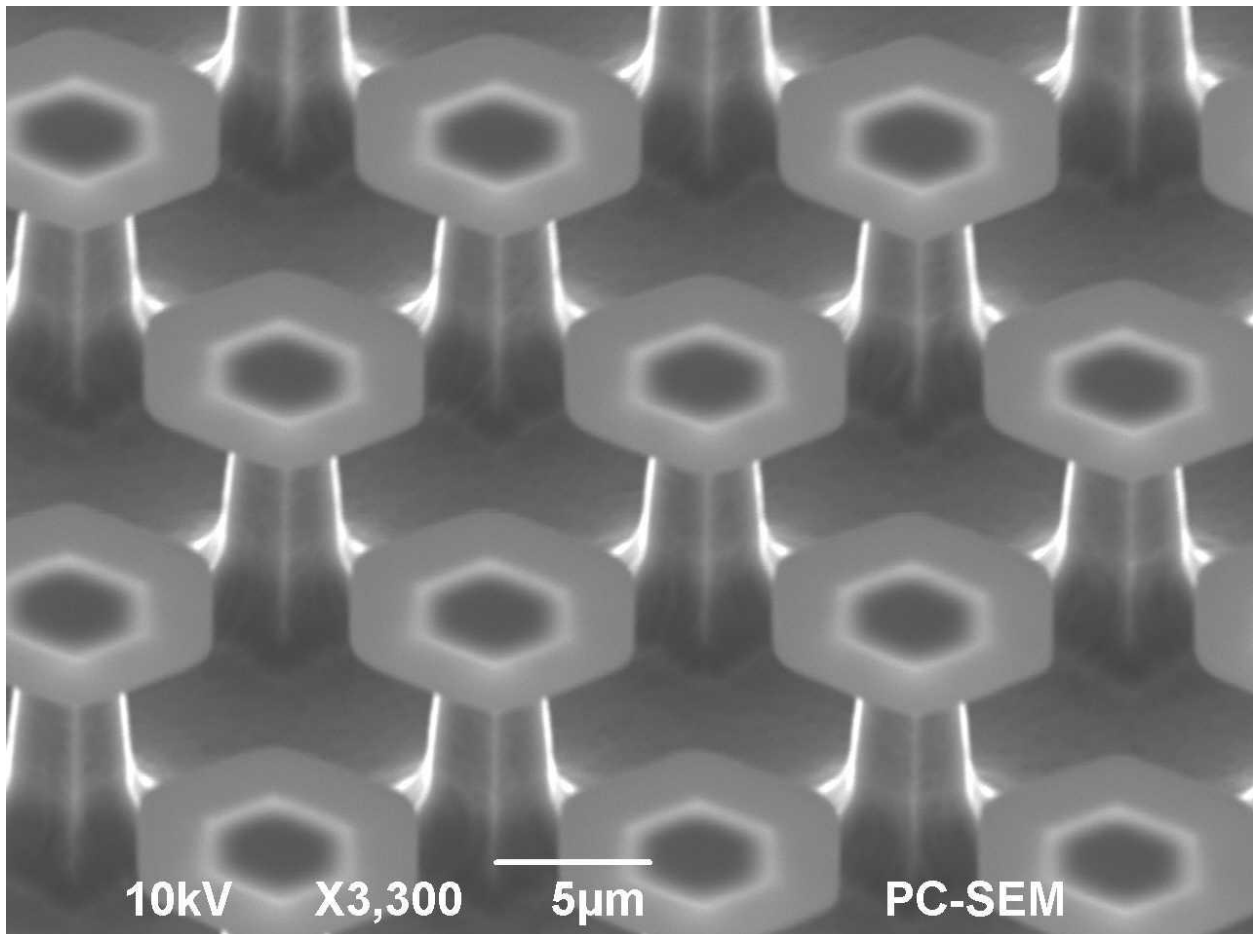


Figure 2-1. SEM image of one of the patterns produced in this work. This surface is composed of approximately $8.7\mu\text{m}$ wide SiO_2 caps on top of $4\mu\text{m}$ wide $8.3\mu\text{m}$ tall Si posts.

Why use hexagonal patterns? Previous reports in the literature discussed the use of similar reentrant non-wetting surfaces [19-21]. These researchers used square and circular features in a square array. However, it is more appropriate to use hexagonal features in a hexagonal grid. This can be explained by the higher level of radial symmetry present in a hexagon or in a tessellation of hexagons. Hexagons have a higher level of radial symmetry than any other simple shapes that can be tessellated (triangles, squares, hexagons).

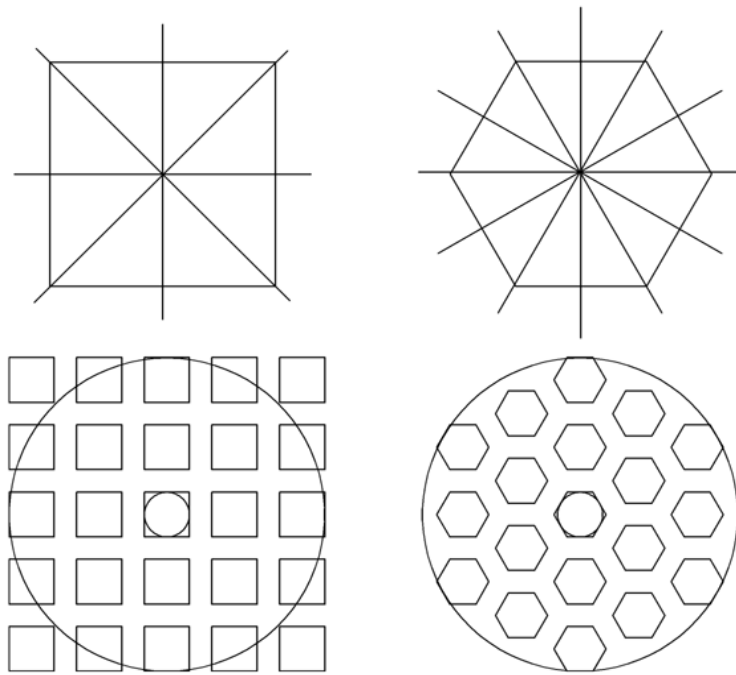


Figure 2-2. Radial symmetry in regular two-dimensional shapes. Hexagonal patterns of circles or hexagons have a higher degree of rotational symmetry. This allows patterns composed of hexagons in a hexagonal array to better line up with contact lines from droplets.

Squares and square patterns have four mirror planes while hexagons have six as seen in Figure 2-2. The higher level of radial symmetry is appropriate due to the radial symmetry of liquid droplets and vapor bubbles caused by the minimization of surface

area. The contact line of a droplet on a surface can more easily line up with the edge of the surface structures as seen in Figure 2-2. This will be made evident in Chapter 3 where we can see how this symmetry will result in a simpler variation in the fraction of a contact line that contacts the structures versus the air pockets.

Parametric variation in cap size and spacing. The design of a parametric variation of both size and spacing of these surfaces for the wetting and boiling work discussed in Chapter's 3 and 4 is now discussed. To study the variation in size of the hexagonal features with a constant spacing the cap sizes used were 3, 5, 10, 20, 30, 40, 60, 80 and 100 μm 's wide, all with 3 μm spacing. To study the variation in spacing 20 μm was chosen as the size with spacing of 3, 6, 12, 24, 48, 96 μm . Spacing in these patterns is defined as edge-to-edge distance, and size of the features is defined as the distance between two parallel edges as shown in Figure 2-3. These ranges were chosen based on the smallest features resolvable using the available photolithographic techniques described below and on the largest spacing and feature size that could have a reasonable effect on the wetting and boiling properties to be investigated. Reasonable effect meaning that for wetting the contact angle of a droplet will approach that of a smooth surface for the 100 μm cap size spaced by 3 μm . If the spacing between structures becomes too large, the liquid vapor interface may bow towards the surface due to the weight of the droplet as shown in Figure 2-4. At a spacing of approximately 100 μm , it is expected that this will cause the droplet to wet the surface. For the boiling work if one were to consider the number of gaps between three hexagonal structures as cavities, then the 100 μm structures spaced by 3 μm 's and the 20 μm structures spaced

by $96\mu\text{m}$'s would both approach the low end of nucleation site density typically studied[22].

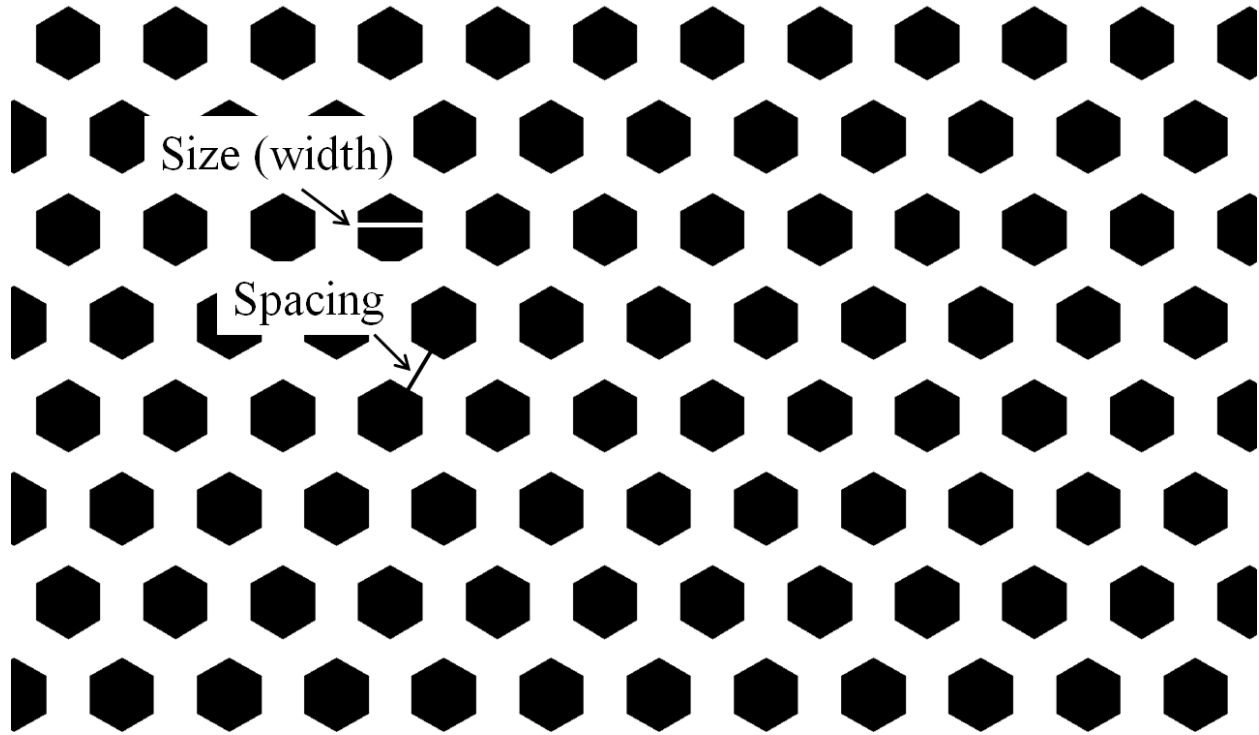


Figure 2-3. Plan view representation of a hexagonal array of surface structures. The size or width of the cap refers to the edge-to-edge distance within a feature while the edge-to-edge distance between two is the spacing.

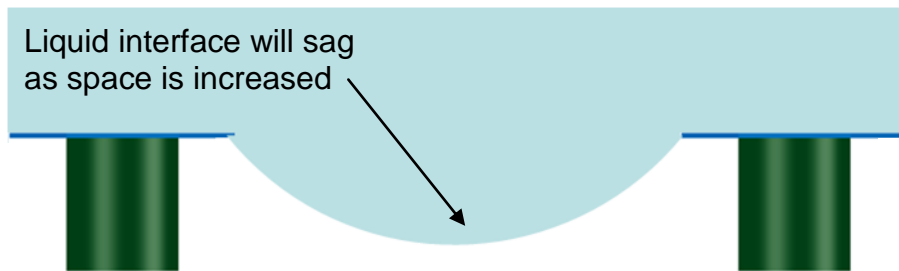


Figure 2-4. Interface curvature as a function of the gap between structures. As the structures are spaced further apart, the interface begins to bend. At a large spacing, the liquid interface will penetrate and fully wet the structure.

To illustrate this for the wetting work Figure 2-5 shows a plot of apparent contact angle on a structured surface as a function of the equilibrium contact angle of a similar smooth surface and the fraction of the surface beneath a droplet that is wetted according to the

work of Cassis and Baxter[9]. Using the range of size and spacing in this work results in a range of contact angles shown as the white line, which covers nearly the entire range of non-wetting contact angles.

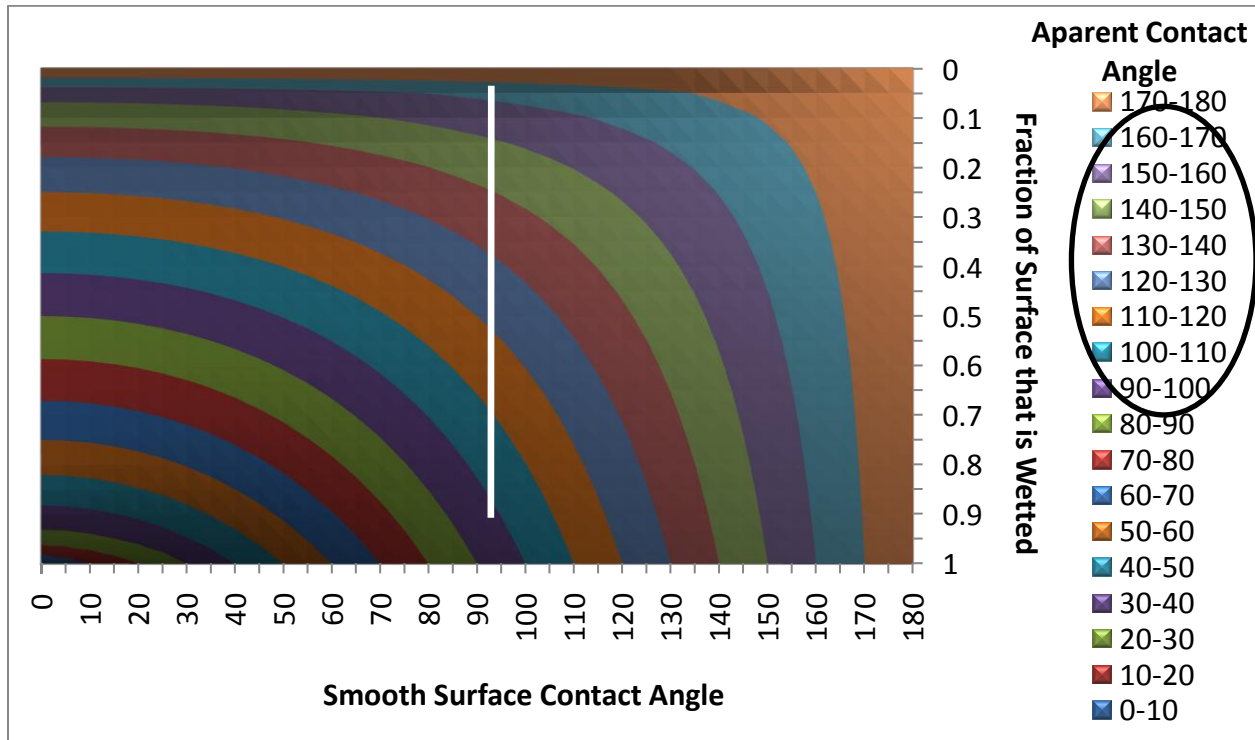


Figure 2-5. Range of receding contact angles produced by surfaces in this work. This is a function of the fraction of the surface under a droplet that is wetted and the contact angle on a corresponding smooth surface as described by Cassie[9].

Variation in structure profile. Aside from altering the size and spacing of the pattern, the cross section geometry of each structure was also varied. Processing conditions were set up to produce a range of undercuts and heights for each pattern as shown in Figure 2-6. These variations are referred to as standard, tall, short, less undercut, more undercut, and no undercut. The height and undercut variations were especially important for later testing of the non-wetting robustness of the surface. Due to mechanical failure of the SiO₂ caps in some of the tests performed in Chapters 3 and 4 the thickness of the SiO₂ caps were increased from 300-500nm.

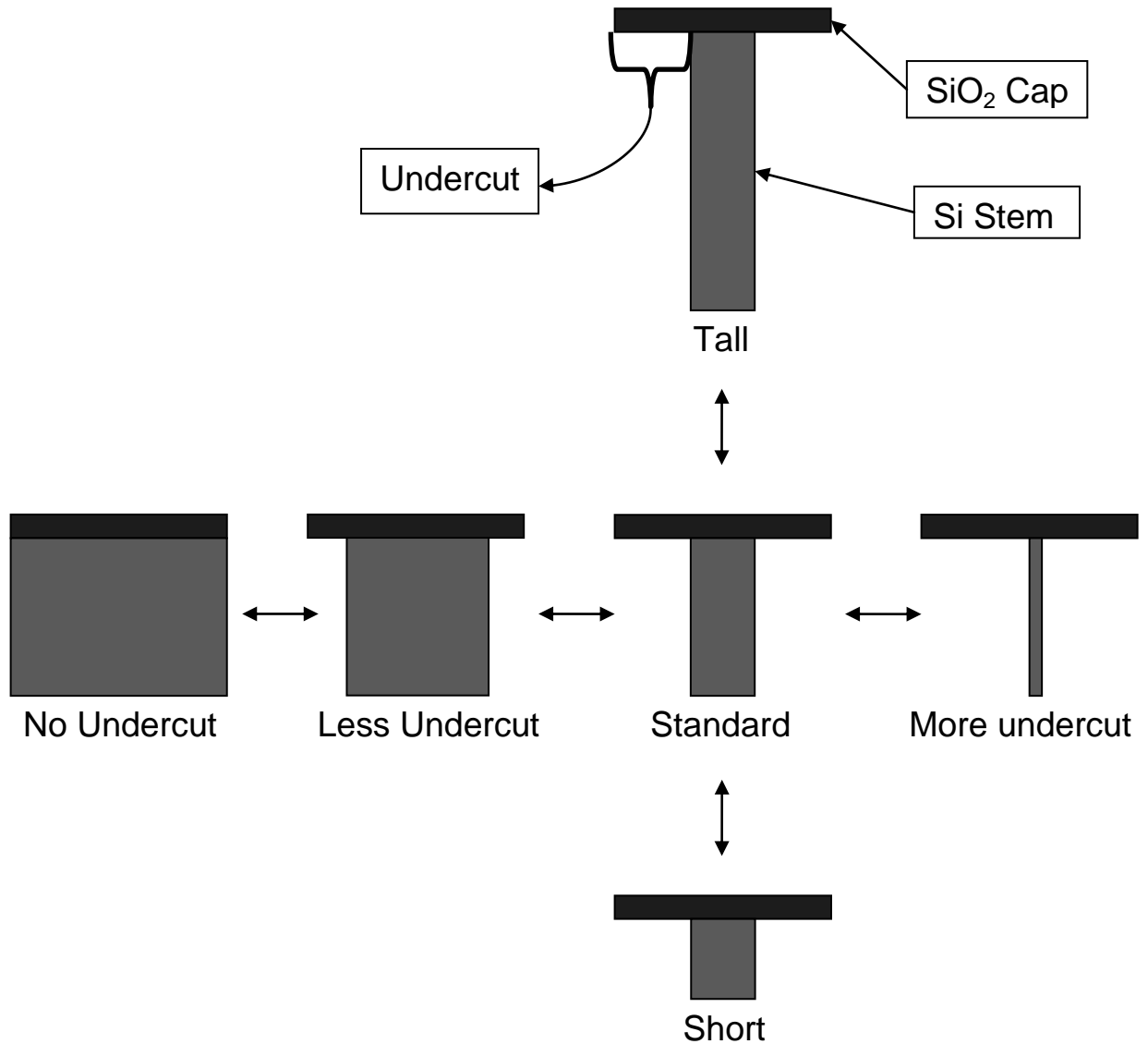


Figure 2-6. Schematic of planned etch variations. All of the etch variations are in comparison with the standard profile with either a change in the degree of undercut or the height of the structure.

Additional patterns to address specific questions. Three additional patterns were created to address specific questions raised in Chapter 3. One pattern consisted of 20 μ m square caps spaced by 20 μ m. Another pattern was made resembling a hash pattern or the inverse of a square array of squares. The width of the bars in the structure was set at 20 μ m's to maintain similarity to the 20 μ m square caps. The spacing

was set at $129.29\mu\text{m}$'s to maintain the same areal fraction of surface to air as for the square pattern (0.25). Finally, a star pattern was created with each star maintaining the same area as a $20\mu\text{m}$ hexagon and the exact spacing of the $20\mu\text{m}$ hexagon spaced by $24\mu\text{m}$ pattern. The star shape was composed of a hexagon and six triangles with heights twice that of the triangles composing the hexagon. The reasons for these patterns and their dimensions will be discussed in Chapter 3.

Fabrication

The undercut reentrant surfaces were fabricated using a combination of plasma enhanced chemical vapor deposition (PECVD), g-line photolithography, and reactive ion etching (RIE) as shown in Figure 2-7. An integral part of this process is the use of deep reactive ion etching (DRIE). DRIE allows for anisotropic (vertical) etching by cycling between an etching plasma and a passivating plasma. After passivation, the sidewalls of the structure are protected from reactive ion etching. The passivation material on the floor of the structure however, is quickly removed due to vertical bombardment of the surface by the plasma due to a vertically generated capacitive coupling in the plasma.

Variation in plasma etch rates between patterns. Plasma etch rates are dependent on not only the plasma conditions but also the wafer being etched. There are two ways the wafer itself affects the etch rate, micro and macro loading. Macro loading is based on the total exposed area that is being etched on the wafer while micro loading is based on the local area being etched. With more area being etched, more reactant ions in the plasma are consumed and more product ions are being created. This leads to a slower etching rate. The result in this work could be that for the same etching conditions the further spaced samples might have lower etch rates. However, this would not be the result because the DRIE process constantly cycles between etchant gasses

every 5-15 seconds. This allows any etch reaction products to be removed periodically and results in a diminished loading effect.

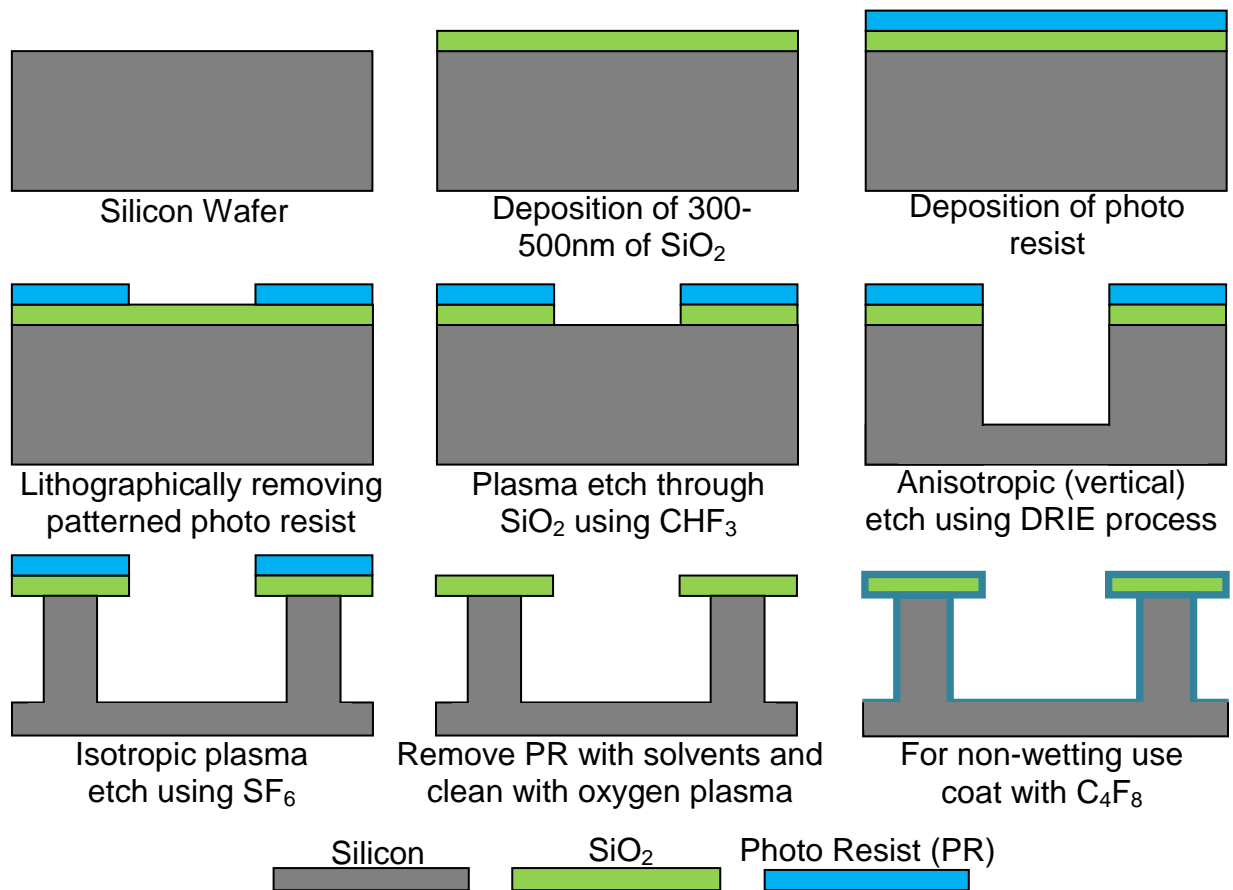


Figure 2-7. Schematic of the fabrication process for surfaces composed of discrete reentrant surface structures. This process results in the deposition of SiO₂, removal of the SiO₂ in areas not intended to be the caps of structures and finally etching down around and then under the remaining SiO₂ caps with a plasma that etches Silicon but not SiO₂.

Producing vertical sidewalls. For the wetting work discussed in Chapter 3, it was important to have relatively vertical sidewalls on the structures. Typically, an isotropic undercut process shown in Figure 2-7 would result in slower etching near the base of the structure. This is because the base of the structure is cooler (closer to the bottom of the wafer that is gas cooled during etching) which results in slower etch rates. It is also partly due to the micro loading effect discussed above. Both of these problems are

solved by using the DRIE set-up and changing the passivate pause cycle. By etching for 5-second intervals and pausing for 10-second intervals, the sidewalls remained vertical after the isotropic etch as the heat and reaction products were allowed to dissipate.

The surfaces were fabricated on single side polished, <100> oriented, p-type, 100mm diameter, 500 μ m thick, 0-100 ohm-cm wafers purchased from University Wafer. The photo masks, composed of separate 1cm patterned areas, were designed on Autocad. The masks were fabricated on soda-lime glass using a Heidelberg DWL 66FS and by Photo Sciences Inc.

Once the wafers were processed and cleaned, those that were going to be used in the wetting study were passivated with a layer of octafluorocyclobutane (C₄F₈). This was used due to convenience as the DRIE equipment used for processing already uses this material to passivate the sidewalls during each etch cycle. The plasma-polymerized layer of C₄F₈ does not produce as non-wetting of a surface as a number of other fluoro-coatings, but worked well for the purposes of this study.

The original mask containing all of the patterns (except for the 20x1.5 μ m, star, and inverse) was designed for deposition and liftoff. The deposition layer was Aluminum. The first test samples that were run in the boiling chamber showed copper growing on the aluminum. To avoid this issue, the process was redesigned to deposit SiO₂ before the lithography and remove it after. This required the addition of an image reversal step to the process to account for the mask being the incorrect polarity.

The fabrication steps used in this process can be found in Appendix A. The variations of etching conditions leading to normal, tall, short, less undercut, more undercut and no undercut structures can be found in Table A-1 in Appendix A.

Characterization and Results

The 3 and 5 μm cap sizes proved difficult to undercut significantly without removing the caps. To address this issue a separate etching condition was set up for these surfaces although the 3 μm cap size still did not survive. The conditions chosen for creating the more undercut structures resulted in the 10 μm and larger spaced 20 μm structures fully releasing the caps. These patterns were removed from further analysis.

SEM analysis was used to determine the actual size and spacing of all patterns. Since the size and spacing of the patterns should only be affected by the lithography and the CHF_3/O_2 etching, which are kept the same for all patterns, analysis was performed on each pattern from the normal and the short etching condition only. Multiple measurements were made and averaged to achieve the actual size used for all analysis. The SEM images including measurements can be found in Appendix B.

The height and undercut of each pattern and etch condition was more complicated. More importantly the variations in etch conditions did not produce exactly the intended effect. For instance, the tall condition uses twice as long an anisotropic etch to make the structure taller. The isotropic etch to produce the undercut was the same as for the standard etch condition but was hindered due to the increased sidewall area. This resulted in less undercut than the standard condition.

Another issue with the etch variations was that the isotropic etch used to produce the undercut also contributes to the height. This was not taken into account and resulted in the less undercut structures also being shorter than the standard structures, which was not intended. While it would be too cumbersome to image the cross section of every pattern for every etch condition, the 10 μm pattern cross sections were imaged to measure the exact heights and undercuts for each etch variation. Figure 2-8 shows a

diagram of the cross sections for the 10 μ m pattern. The actual cross section SEM images that these measurements were made on can be found in Appendix B. Figure 2-9 is a plot of the undercuts and heights of these variations. Undercut is measured as the distance from the edge of the cap to the stem of the structure. The naming scheme used for the intended variations will continue to be used in this work but the actual dimensions will be taken into account when making comparisons.

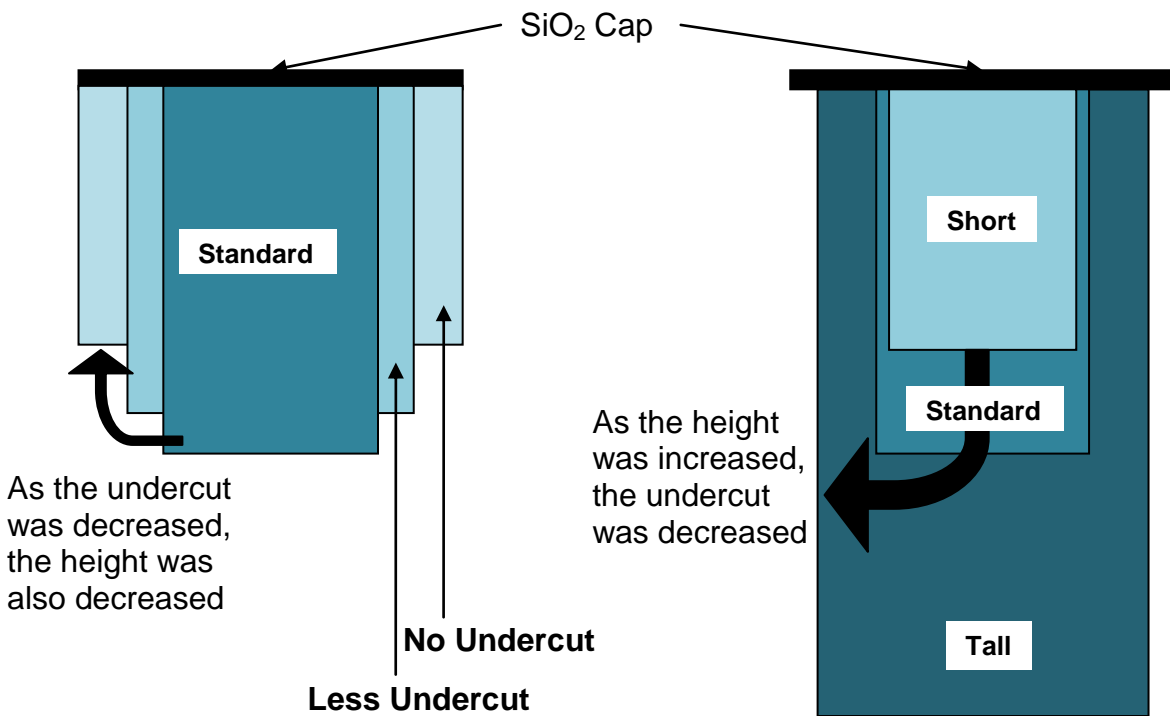


Figure 2-8. To scale schematic of actual height and undercut for each of the etch variations. The actual SEM measured cross sections can be found in Figure 2-8.

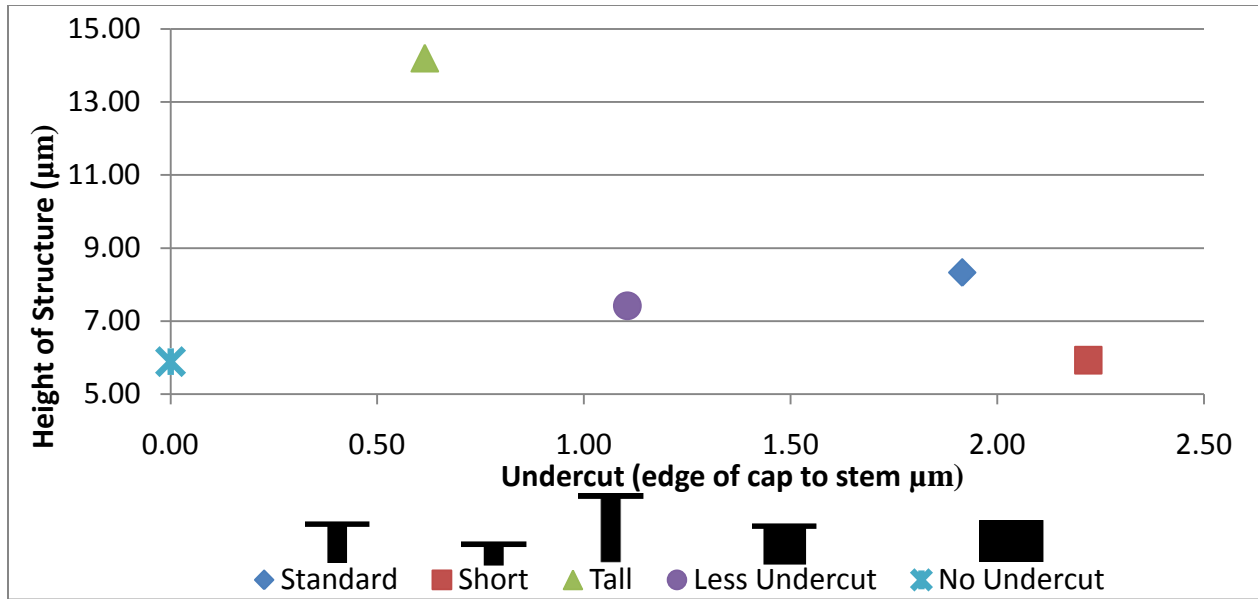


Figure 2-9. Plot of the undercut and height variations for the 10µm pattern cross section. Based on the actual results it appears that the only significant variations are in undercut with the tall structure having the only significant variation in height.

CHAPTER 3

WETTING ON REENTRANT UNDERCUT SURFACE STRUCTURES

In Chapter 3, a model will be developed to predict contact angles on well-defined structured surfaces. This model is based on a modified Cassie-Baxter equation, a radial plot of the fraction of the droplet surface interface that is wetted, and the advancing and receding contact angles measured on a similar smooth surface. This model be tested on the surfaces discussed in Chapter 2 and shown to be significantly more accurate than the Cassie-Baxter or modified Cassie-Baxter equations developed by Choi and Tuteja[9, 19]. This will provide support that the way wetting is often taught and conceptualized is incorrect. Specifically contact angle is a function of only the forces that act along the contact line of a droplet, not the forces that act on the entire underside of the droplet. An introduction to the relevant wetting concepts for this work can be found in Chapter 1.

Literature Review

During the literature review, the various derivations of wetting equations will be described and discussed. As a simplification, the subscripts will be kept the same throughout. The variable γ refers to surface tension (same as surface energy), W to the work of adhesion, E to Cassie and Baxter's energy of adhesion, and the subscripts L, G, and S are the liquid, gas, and solid phases or phase boundaries if combined as a subscript. This review of the literature is not meant to be exhaustive but instead to focus on those works that have had lasting or direct impacts on the current work. An exhaustive review would be nearly impossible considering the thousands of papers dealing with wetting and even the hundreds of papers dealing with contact angle prediction.

Wetting on Ideal Surfaces

Thomas Young was one of the first to understand that the contact angle of a droplet at rest on a solid surface is related to a force balance of the surface tensions of the three two-phase interfaces (solid-liquid, solid-gas, and liquid gas) in the plane of the surface[11]. This led to the development of the following equation relating the contact angle and the surface energies of the three two-phase boundaries:

$$\gamma_{SG} = \gamma_{SL} + \gamma_{LG} \cos(\theta) \quad (3-1)$$

The Young equation only applies to ideal surfaces that are rigid, smooth, and free of defects. Figure 3-2 shows a description of the three forces acting on the three-phase line as described by Young's equation.

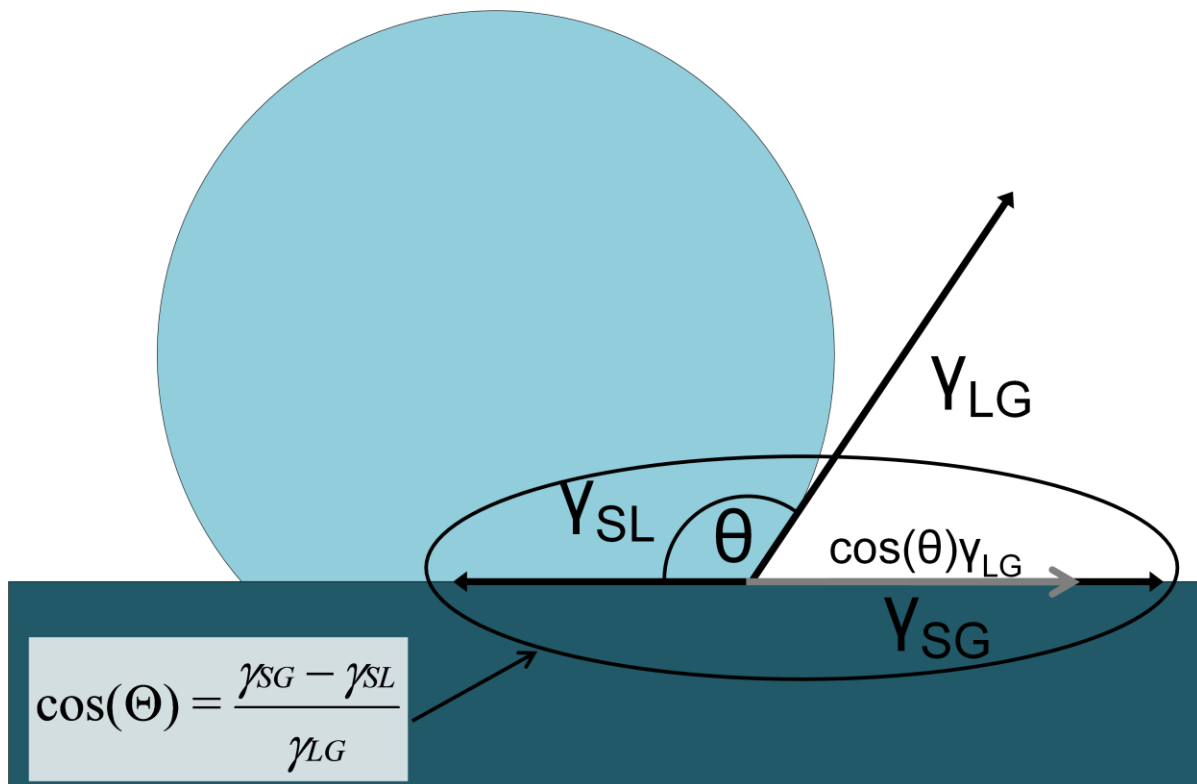


Figure 3-1. Components of Young's contact angle. Surface tensions when discussing Young's equation are described as forces per unit length. Balancing the horizontal forces imparted on the contact line of each of the three surface tensions results in Young's equation.

Athanase Dupré in his book *Théorie mécanique de la chaleur* (1869), expanded upon Young's work by further describing wetting in terms of the work required to adhere a droplet to a surface. Perhaps Dupré's most well known relation relates the work of adhesion to the surface energies of the phase boundaries before and after adhesion:

$$W = \gamma_1 + \gamma_2 - \gamma_{12} \quad (3-2)$$

Either Dupré originally published this theory incorrectly or with a typographical error that was later corrected by others in further publications. The original publication gave:

$$W = \gamma_1 + \gamma_2 - 2\gamma_{12} \quad (3-3)$$

When the Dupré equation (equation 3-3) is combined with the Young equation, the result is what is referred to as the Young-Dupré equation:

$$W = \gamma_L + \gamma_L \cos(\theta) \quad (3-4)$$

This equation relates the work of adhering a droplet to a flat solid surface to the surface tension of the liquid and the angle formed between the solid-liquid and liquid-gas interface. These equations have found wide use in many fields such as adhesives development and thin film deposition in the semiconductor industry.

Gibbs expands on the works of Young and Dupré in the process of developing the thermodynamics of solid-liquid-vapor systems[23]. His work was the first to describe the surface energies as being due to the excess free energies of the atoms in the surface. Gibbs work provided a very detailed derivation of Young's equation that is valid for any geometry and includes gravity. The numerous models that have been discussed and expanded upon over the past 70 years often leave out Gibbs' work. This is due to the cumbersome nature of the formalism, which allowed for a much larger scope than just wetting.

Roura[24] expanded on Gibbs work in the scope of wetting. He provided the most rigorous and general approach to date by combining both mechanical and thermodynamic terms. In his work Roura provides two figures, the first representing the basis of the most popular local derivation of Young's equation shown in Figure 3-3.

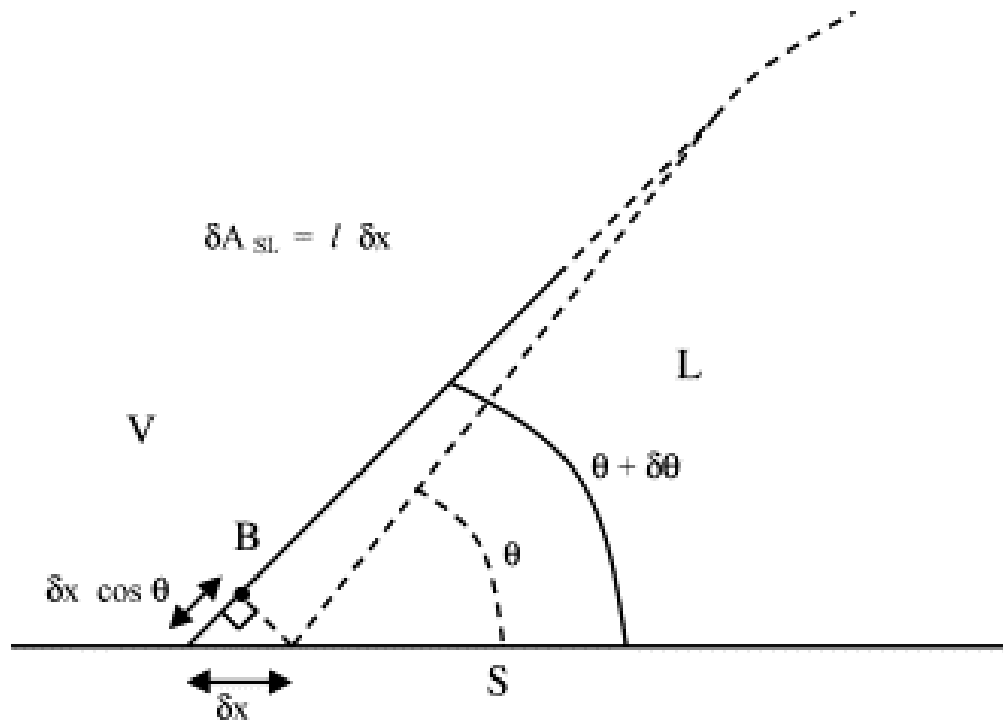


Figure 3-2. Basis of local derivation of Young's equation not taking into account the non-local effects of altering the length of the three-phase line

The second, shown in Figure 3-4, shows that any change in the length of the three-phase line is associated with a change in the curvature of the liquid droplet. This implies that any rigorous model cannot claim that the variation in the local energy of the three-phase line is equal to the total energy change. A term would have to be added to account for the energy associated with the change in curvature of the liquid-vapor interface. In most cases, the small size of the drops used will result in this term being very small and it is therefore reasonable to neglect it.

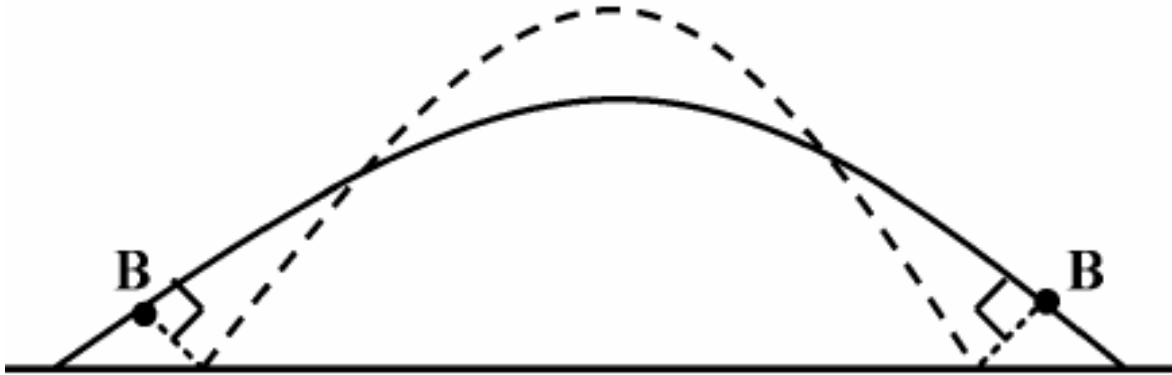


Figure 3-3. Alteration of the droplet surface with an increase in the length of the three-phase line

Wetting on Real Surfaces

Real surfaces differ from the idealized surfaces discussed previously in that they include defects, irregularities, surface functionality and so forth. More specifically, they do not display just one equilibrium contact angle. Instead, they display a range of stable contact angles varying from the receding to the advancing. In the 100-150 years after Thomas Young published his work there were many debates in the literature over which contact angle measurement should be applied.

Pease published a paper in 1945 attempting to clear up this debate[25]. Pease proposed that a solid surface is composed of varying areas of polar and non-polar groups. In terms of water wetting, he describes the tension at the triple-phase line as relating to the fraction of these groups it encounters. When the triple-phase line encounters a maximum fraction of polar groups, the contact angle would reach a minimum while a maximum would be achieved when the line encounters a maximum in the fraction of non-polar groups. This description has been largely ignored over the past 60 years. It will however be expanded upon in this work and shown to be the most accurate of the early models.

Tadmor[26] attempted to understand the hysteresis in contact by adding a term to Young's equation to represent the energy of the three-phase line. He equates the energy of this line to a pinning force that always acts contrary to the movement of the three-phase line. The plot of line energy as a function of equilibrium and apparent contact angle is shown in Figure 3-5. One of the flaws of Tadmor's work is that he does not take into account the non-local effects of increasing or decreasing the length of the triple-phase line as described by Roura.

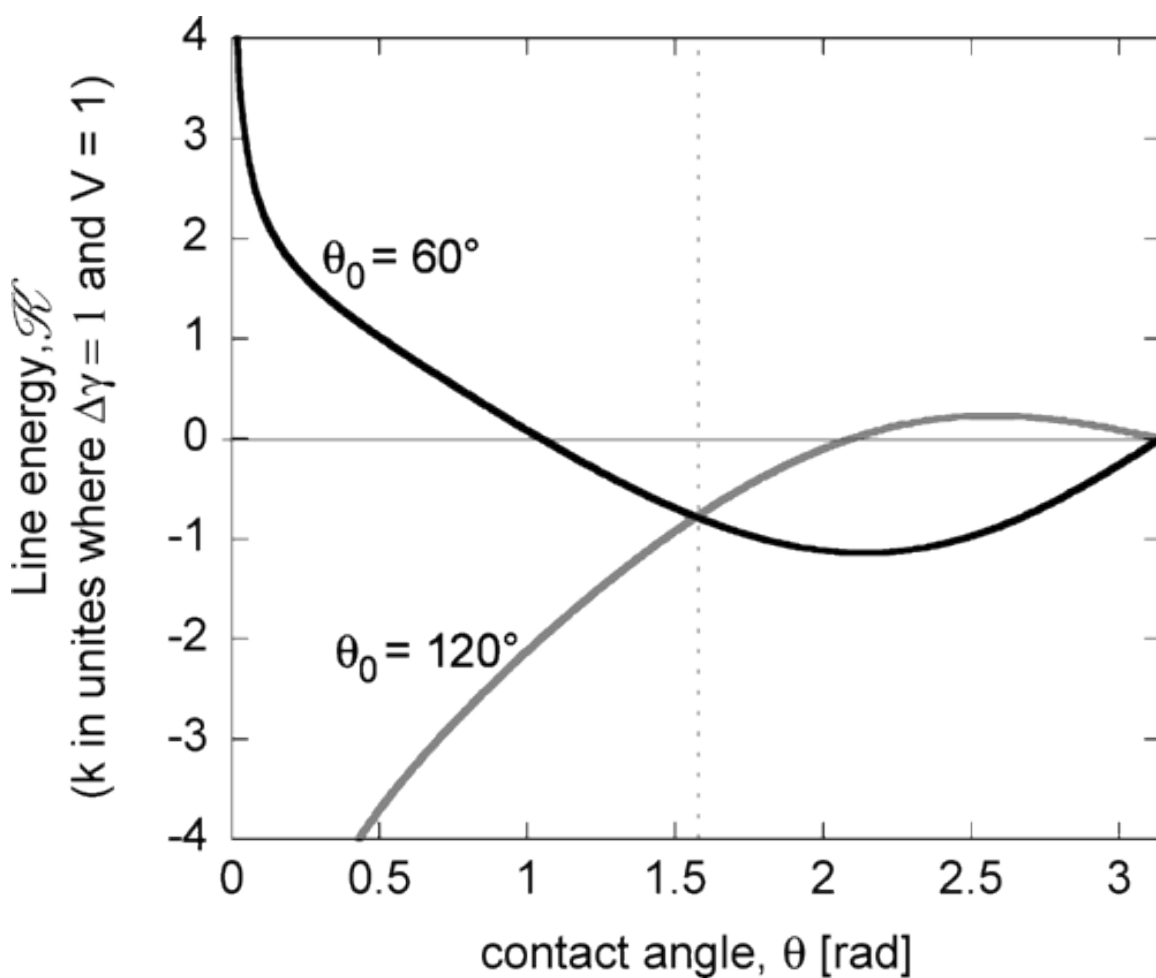


Figure 3-4. Line energy as calculated by Tadmor. Reprinted with permission from {Tadmor, R. (2004). "Line Energy and the Relation between Advancing, Receding, and Young Contact Angles." *Langmuir* **20**(18): 7659-7664}. Copyright {2011} American Chemical Society

Wetting on Rough and Textured Surfaces

The Wenzel equation for wetting on rough surfaces. Wenzel proposed the addition of a roughness factor that would account for the amplification of surface energy as a result of roughness increasing the area of the wetted surface compared to a planar area[10]. The roughness factor is equal to the true area of a solid surface divided by the planar area. The resulting equation gives the apparent contact angle as a function of the roughness factor and Young's contact angle based on an ideal smooth surface:

$$\cos(\theta^*) = r\cos(\theta) \quad (3-5)$$

This equation is intended to apply only to rough surfaces that are homogeneous.

The Cassie-Baxter equation for wetting on multi-component surfaces.

Further generalizations were made by Cassie and Baxter to allow for heterogeneous surfaces[9, 27]. They developed a net energy balance along the surface to describe the change in surface energy. This approach is based on the areal fraction of the surface beneath a droplet that encounters each component. There is special attention paid to the case of structured surfaces with one component being air (the interface lies over pockets of air). In this case, f_1 is the fraction of the droplet interface that sits on the solid surface and f_2 the fraction that lies over air pockets. They show that when a droplet is brought into contact with a surface the solid-gas interface is destroyed at the expense of the solid-liquid interface being created for each component. In the case of an air interface, there is no energy associated with destroying the air-air interface present before the droplet is deposited. The resulting change in net energy developed for the case of a composite between a solid surface and air pockets is shown in equation 3-6 and described in Figure 3-5.

$$E = f_1(\gamma_{LS} - \gamma_{SG}) + f_2\gamma_{LG} \quad (3-6)$$

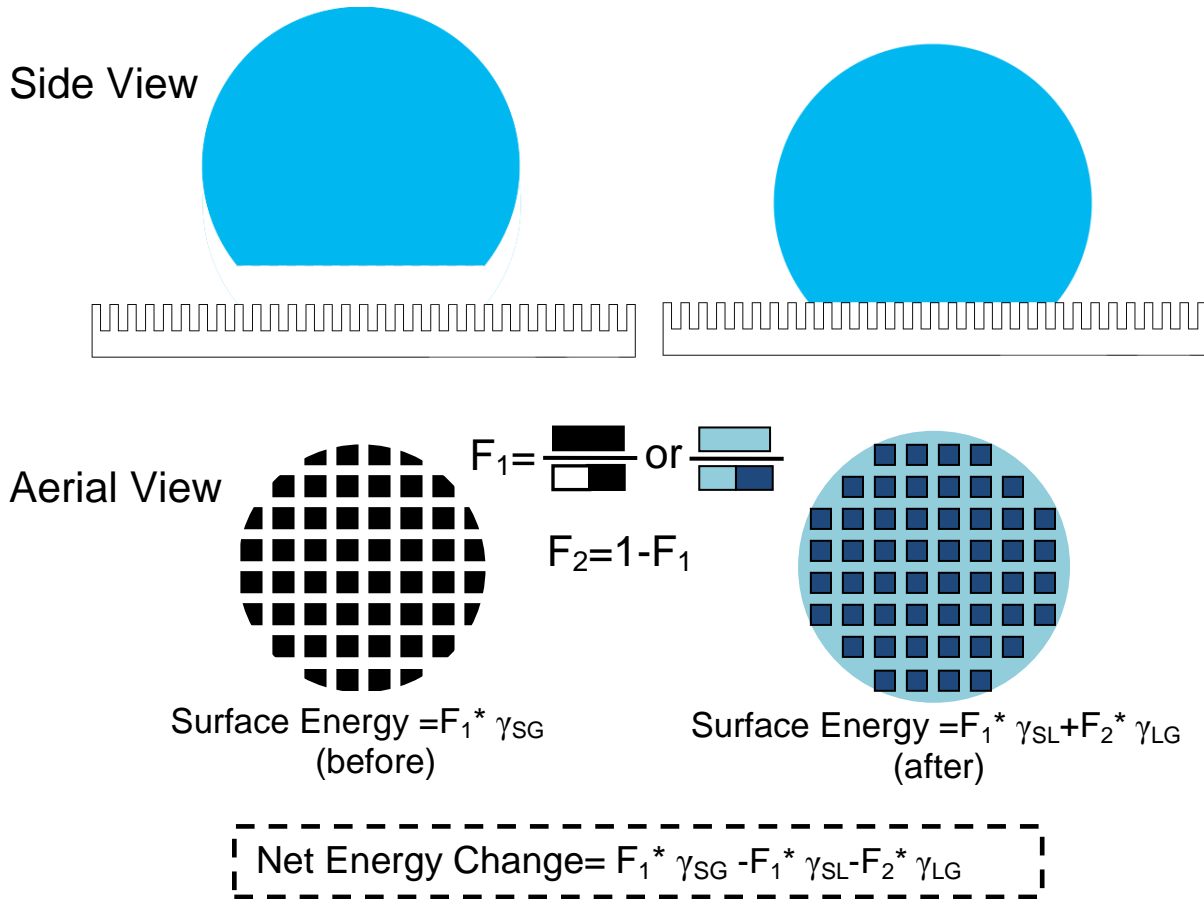


Figure 3-5. Graphic representation of surface energy minimization according to Cassie and Baxter. The energy balance is related to the areal fraction of each component on the surface.

Combining this equation with Young's equation results in equation 3-7.

$$E = \gamma_{LG}(f_2 - f_1 \cos(\theta_1)) \quad (3-7)$$

θ_1 is the contact angle on a surface composed only of component 1. Cassie and Baxter then describe the energy E required to wet unit surface of solid from Young's equation as $(\gamma_{LS} - \gamma_{SG})$, then rewrite Young's equation as:

$$\cos(\theta) = -E/\gamma_{LG} \quad (3-8)$$

Plugging equation 3-8 into equation 3-7 results in the well known Cassie-Baxter equation for wetting on solid air composite surfaces.

$$\cos(\theta_{cassie}) = f_1 \cos(\theta_1) - f_2 \quad (3-9)$$

Using the same derivation as Cassie and Baxter and allowing for a number of surface components results in the traditional general form of the Cassie Baxter equation (3-9).

$$\cos(\theta_{Cassie}) = f_1\cos(\theta_1) + f_2\cos(\theta_2) + f_3\cos(\theta_3) \dots \quad (3-10)$$

Gao and McCarthy have shown that the works of both Wenzel and Cassie and Baxter are fundamentally flawed. The flaw lies in the use of an areal wetted fractions to describe a phenomenon that is only related to the area near the contact line of a droplet. Gao and McCarthy devised a number of experiments where they alter the chemistry or texture of a surface in a small area, then measure the contact angles of droplets whose triple phase lines fall either inside or outside the altered area[28]. In all cases, the contact angle of the droplet is only affected by the surface area in contact with the triple phase region. In other words they have extensively shown that the thermodynamic arguments used by Wenzel, Cassie and Baxter that are based on minimizing the surface energy of the entire drop contact area cannot be used to reliably predict measured values of contact angle. The formulations of Wenzel and Cassie and Baxter indicate some form of long-range force or interaction occurring between any point along the surface droplet interface and the area where the contact angle is actually formed. Clearly no such force exists that would act over ranges greater than the millimeter scale. While Gao and McCarthy have shown that Wenzel and Cassie-Baxter equations do not relate to contact angle in some situations, they have not proposed a corrected model.

Tuteja produced simple reentrant structured surfaces using photolithography and dry etching [20, 21] similar to those that will be discussed in this work. The structures were fabricated by depositing a 300nm thick layer of SiO₂, using photolithography to

mask the structures, removing the SiO_2 from the exposed area using reactive ion etching (RIE) and dry etching using XeF_2 to undercut the structures. XeF_2 is a gas phase isotropic etchant. The surfaces were then coated with various fluorinated polyhedral oligomeric silsesquioxanes to reduce the surface energy. The patterns used for these structures consist of discrete squares on a square lattice, the inverse of discrete squares resembling a hash pattern, concentric circles, spirals, and parallel lines. Based on these structures Choi and Tuteja developed a modified Cassie-Baxter relationship to explain contact angle hysteresis on textured hydrophobic surfaces[19]. They calculate a term ϕ_d , a linear wetted fraction to be used in place of the areal wetted fraction used in Cassie and Baxter's work. ϕ_d in their work is tailored to various situations based on the observed movement of the three-phase line. This is useful in situations where there is anisotropy and a separate ϕ_d should be used in different directions or with unusual patterns such as spirals. The ϕ_d value is either set to the square root of the areal fraction in the case of patterns on a square lattice, the actual areal fraction in the case of stripes or zero.

In their work, Choi and Tuteja also attempt to validate the ability of Cassie and Baxter's model to predict equilibrium contact angles. This is done by vibrating a droplet at rest on an isotropic surface pattern. Before the vibration, the contact angle is anisotropic with contact angles of 165° in one direction and 119° in the other. After vibration, the contact angles are 119° and 113° . They propose that this is due to the vibration allowing the droplet to overcome local energy minima and conform to the global minima at the equilibrium contact angle of 114° .

Extrand also produced a very detailed model to predict contact angle hysteresis on well defined surfaces but the model often predicts contact angles worse than the Cassie Baxter model[29]. There is also interest in determining the equilibrium contact angle that would exist on a smooth surface only having knowledge of the advancing and receding contact angles on a structured surface[30].

The Debate over the Validity and Applicability of Wetting Laws

The validity of Cassie's and Wenzel's laws has recently been questioned by Gao and McCarthy in their paper "How Wenzel and Cassie Were Wrong"[28]. This is not the first time that papers have been published discussing contrary models to Cassie and Wenzel but it is the first time the issues have been plainly stated in an effort to correct a long-standing confusion in the field of wetting[25, 29, 31, 32]. This has led to an ongoing debate over both the validity and applicability of these equations.

According to Gao and McCarthy, the use of Wenzel's and Cassie's equations has been shown many times to be invalid [25, 28, 31-38]. Only the area near the three-phase contact line can have any effect on the contact angle. This should be obvious based solely on the fact that no known force could act in any significant way over the range of millimeters (from the area beneath the droplet to the boundary). Zhang proved this point using a mean-field free-energy lattice Boltzmann approach[39]. He found that Cassie's equation was "in general not valid". This is because the size scales of regular patches that can be patterned on a surface do not approach the small scale of the interfacial thickness.

Kwon found that his experimental data followed the trend of Cassie's equation except for situations that involve discrete pillars on a surface. His defense of Cassie and Baxter misses the point as it has been long established that in most cases the formula

matches experimental trends. The fundamental derivation and accuracy are being questioned not the trend of the results.

Panchagnula and Vedantam respond to "How Wenzel and Cassie got it Wrong" by twisting the wording and attempting to interpret the unstated intentions in Wenzel and Cassie and Baxter's works to conclude that they intended the wetted fraction to be that near the three-phase contact line[40]. This is mostly semantic and incorrect as it has always been clear that these works made use of the areal fractions not fractions near the triple-phase line. This was directly responded to in Gao and McCarthy's "Reply to "Comment on How Wenzel and Cassie Were Wrong by Gao and McCarthy"[41].

McHale responded to Gao and McCarthy in " Cassie and Wenzel: Were They Really So Wrong?"[42]. In this paper, they primarily defend the Wenzel and Cassie-Baxter derivations by claiming a number of assumptions or situations where the arguments are valid. The following quote defines his argument:

"Moreover, if the roughness of a substrate surface is constant, then there is no difference in the value obtained by calculating the roughness parameter using a small part of the surface at the periphery of the droplet, the whole of the substrate surface, or the specific area of surface wetted under a droplet. In this case, all of these calculational methods are equivalent."

This statement is incorrect. The results of Chapter 3 will show that even on surfaces that are constant and continuous by any definition the three-phase contact line wetted fraction is not only different from the areal fraction but is also different for the advancing and receding droplets. McHale also pointed out that when discussing the wetted fraction of the three-phase contact line one is actually discussing the portion of the drop periphery that is three-phase as opposed to two-phase in the case of a solid-air composite surface.

Bormashenko argues that taking into account a thin liquid precursor film around the droplet and a good relation to experimental results justifies the application of the Cassie-Baxter equation [43, 44]. This however, does not address the issue of accuracy or the results put forth by Gao and McCarthy.

Nosonovsky in "On the Range of Applicability of the Wenzel and Cassie Equations"[45], also attempts to determine under what conditions and assumptions the Cassie-Baxter and Wenzel equations are valid. To be clear, this is not a valid premise. Just because one can find certain circumstances where the global areal fraction is equal to the linear fraction, it is not acceptable to claim that the equations in question are valid under those circumstances. They may happen to provide accurate results but they are rooted in misunderstanding.

Marmur directly attacked Gao and McCarthy's paper [28] in two ways. He first claimed that they used too small drop sizes and that at larger drop sizes the contact angles would approach those predicted by Cassie's equation (if the wavelength of roughness was sufficiently small). Marmur also discussed a number of different contact angles and claimed that the most stable apparent contact angle is related to the areal fraction. This last point is incorrect while the first is irrelevant, only proving that the areal fraction happens to match the linear fraction under some conditions. Marmur's comments are specifically refuted in Gao's "An Attempt to Correct the Faulty Intuition Perpetuated by the Wenzel and Cassie "Laws""[46].

Tuteja and Choi seem to have misunderstood Cassie and Baxter's work as they claim that contact angle hysteresis cannot be determined using it. This is not the only case where this claim is made[47]. In their paper Cassie and Baxter clearly state, that

the use of $\theta_{\text{advancing}}$ or θ_{receding} from the smooth surface will give the corresponding apparent contact angle on the structured surface. Further, the general idea that the three-phase line's wetted fraction can be simply taken as the square root of the areal fraction is not valid. This would only hold true in four specific directions for a square lattice. An accurate determination of the fraction of the three phase wetted fraction would have to take into account an integration of the line passing through a structure from 0 to 360°. The idea that the minimum and maximum wetted fraction of the three-phase line should correspond to the advancing and receding contact angles is useful and will be expanded on in the work.

The claim, that the convergence of the anisotropic contact angles to the equilibrium angle after vibration is evidence in support of Cassie and Baxter's model, is not clear. First, the contact angles do converge toward the equilibrium angle but they do not reach it or become isotropic. Their argument is partially valid but the driving force is likely minimization of surface area of the droplet due to the anisotropic condition. It is also well known that the Cassie Baxter model predicts somewhat accurate contact angles in most situations.

Roach et al. and Ma put together excellent reviews including most of the superhydrophobic surface work that has been produced [48, 49]. It includes a large section on the use of a number of photolithographic techniques to produce superhydrophobic surfaces. A similar review was also produced by Crick[50].

A rigorous approach to this system would have to take into account the finite thickness of the triple line region due to the molecular distances over which forces are felt, however for the sake of this work it is a reasonable approximation to treat the triple

line as one-dimensional. This is because the scale in which molecular forces are felt is significantly smaller than the scale that the surface patterns vary over.[12]. Mognetti produced a mesoscale simulation describing the physics of pinning and dewetting on receding of a droplet [51]. Iwamatsu developed an analytical expression for translationally symmetric droplets based on the average contact angle of the droplet contact line[52].

Hypothesis and Model

Hypothesis. As discussed in the literature review, the Young equation describes the balance of forces related to an equilibrium contact angle on an ideal surface. The three forces are the surface tension of the liquid-solid interface, gas-solid interface, and liquid-gas interface. On a real surface, there is always a range of stable values ranging from the advancing to the receding angle. The reason for this is that on the microscopic scale as the three-phase line expands there will naturally be small fluctuations in the surface conditions (roughness, chemical composition, defects and/or air pockets). For a translationally symmetric surface, if the variation in surface chemistry, roughness and structure is known (as a function of radius) and the advancing and receding contact angles on a smooth surface of each component are known, it is possible to calculate the local advancing and receding angles for any drop size. The maximum contact angle of a droplet will occur at the radius with the lowest average energy. The receding contact angle will occur at the radius with the highest average energy. The variation of energy on a smooth surface is due to variations (defects, grain boundaries, irregularities) on the molecular scale, while variations on structured surfaces usually have much larger length scales. This allows for the assumption that an advancing or receding local minima in surface energy can always be found near any value of the

maxima or minima in surface energy due to the structure of the surface. This is shown in Figure 3-6.

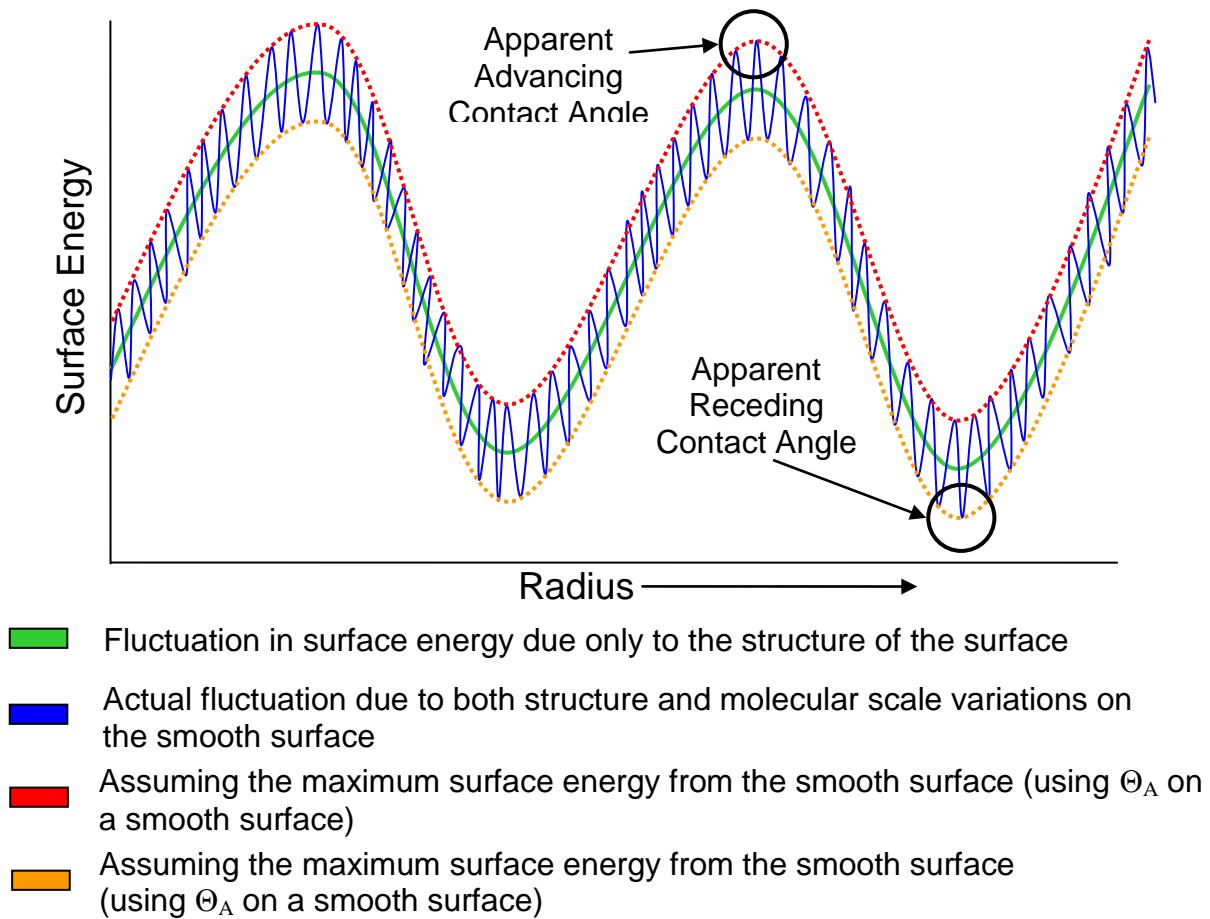


Figure 3-6. Contributions to the surface energy from molecular scale variations and structure. Contact angles are functions of radial fluctuations in surface energy. The molecular scale fluctuations on the smooth solid portion of a structured surface occur over a smaller length scale.

Modified Cassie-Baxter equation. The Cassie-Baxter equation predicts the contact angle that results in the lowest total energy based on the fraction of each component. By applying the same derivation as described by Figure 3-5 with the exception of using the fraction of the contact line (φ_{cl}) instead of the contact area we arrive at a modified Cassie-Baxter equation.

$$\cos(\theta_{Modified}) = \varphi_{cl} * \cos(\theta_1) + (1 - \varphi_{cl}) * \cos(\theta_2) \quad (3-11)$$

Applying the local minimum φ_{cl} and the smooth surface advancing contact angle (for each component of the surface) results in the apparent advancing contact angle.

Applying the local minima in φ_{cl} and the receding contact angle from the smooth surface (for each component of the surface) results in the apparent receding angle. This is due to the surface energy fluctuation argument described in Figure 3-6.

Calculation of Linear Wetted Fraction

As discussed previously the correction to the thermodynamic approach used by Cassie and Baxter involves the use of linear fraction of wetted area encountered by the three-phase line φ_{cl} . To calculate φ_{cl} as a function of the radius of the droplet, first black and white images were rendered of each surface in Autocad. Each image was set to have one pixel represent 250x250nm, which approximates a zero thickness line compared to size of the caps.

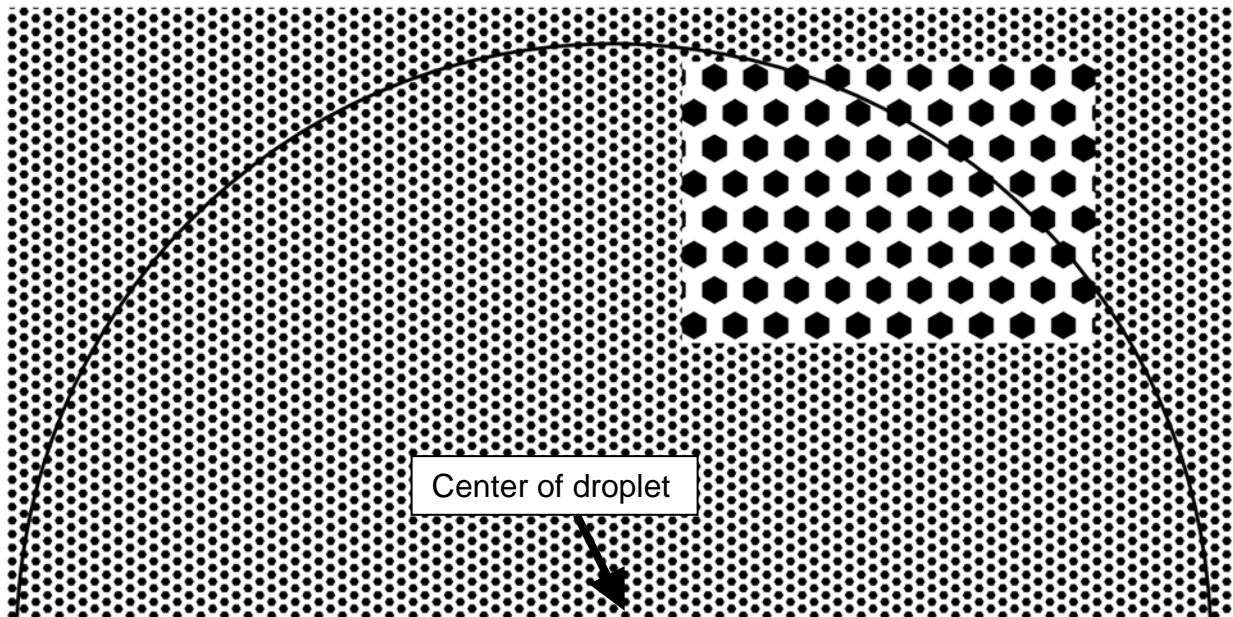


Figure 3-6. Cad generated image (compressed from ~68 million pixels) of a surface based on SEM measurements. This image is based on the 20 μ m hexagon surface with 12 μ m spacing. φ_{cl} is based on the fraction of black and white pixels as a function of the radius.

The wetted surface structures were black and the liquid-gas interface white. The size of the image was set to insure that the maximum radius would be greater than any droplet radius to be calculated within the experimental methods (5600x11200 pixels). This takes into account the fact that all surface structures investigated have at least one mirror plane in common allowing the measurement to be made using only 180° of the surface. Using only 180° of the image has no effect on the outcome of φ_{cl} but significantly reduces computation time considering the size of the images (~68Mpixels). Figure 3-6 shows an example image for the 20 μ m hexagon surface with 12 μ m spacing. The images were then analyzed by the Matlab code found in Appendix C. This code first finds the center of the black object nearest to the center of the image. It then truncates the slice of the image that is not part of the 180° to be analyzed. At this point, it calculates the distance to every pixel from this center point and adds it to one of two lists, black or white. These distance vectors are then converted to a histogram of white and black pixels by radius value and divided by each other giving a vector whose indices represent the radius and values represent φ_{cl} . A mock plot of φ_{cl} from a zoomed in hexagonal array can be found in Figure 3-7 along with the image used to generate the plot. The grey concentric rings in this plot represent minima and maxima in φ_{cl} . The green arrows point to the corresponding peaks in the φ_{cl} plot generated in MATLAB. The local maxima and the receding contact angle from a non-structured surface are then plugged into Equation 3-11 to give the apparent contact angle. Using the local minima and advancing angle gives the apparent advancing contact angle. Similar mathematics could be used for non-flat structures. Long described the analytical methods required to make calculations for surfaces with various contours[53].

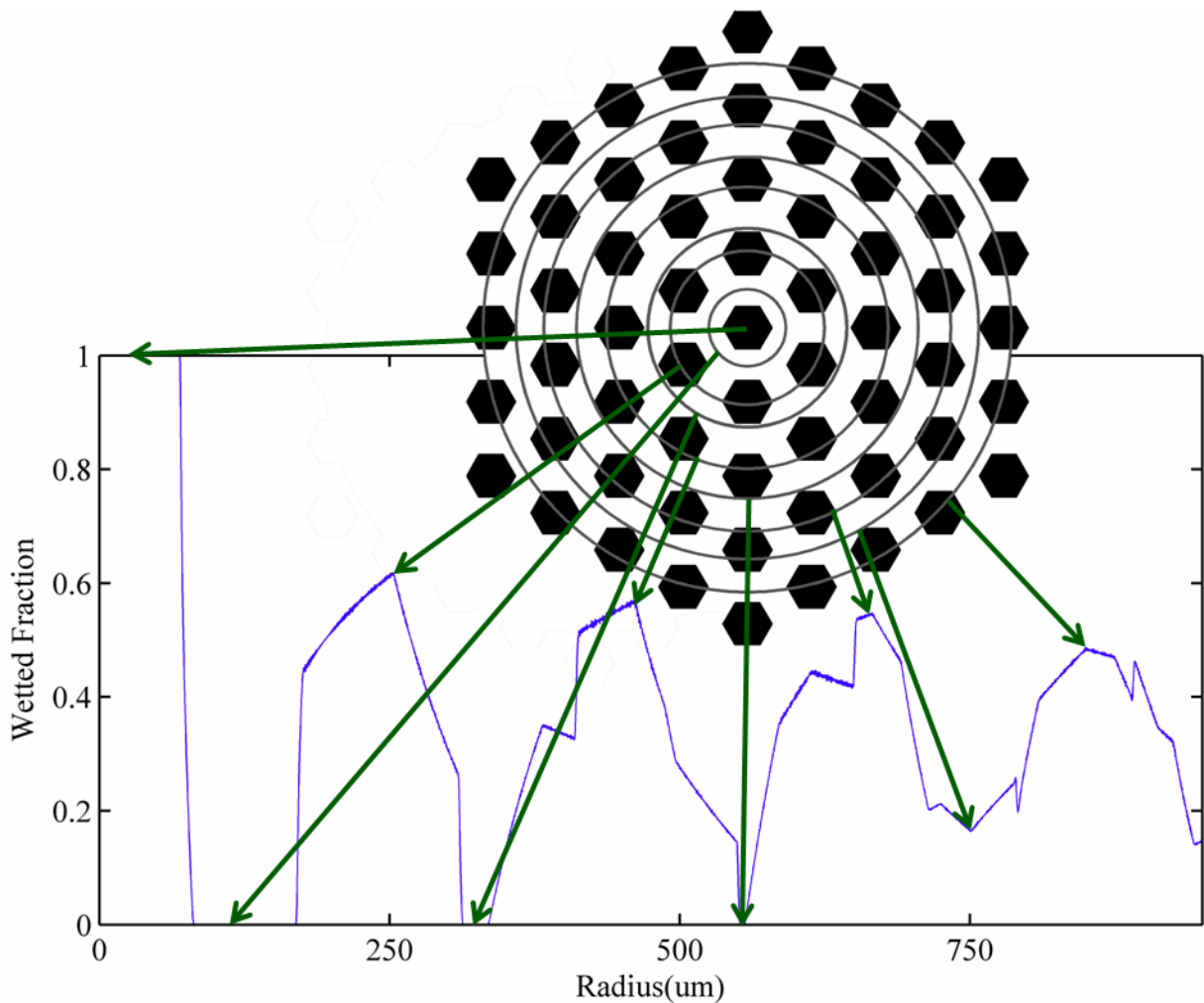


Figure 3-7. Zoomed in plot of ϕ_{cl} and mock hexagonally structured surface. As an example, the grey concentric rings in this plot represent minima and maxima in ϕ_{cl} . The green arrows point to the corresponding peaks in the ϕ_{cl} plot generated in MATLAB.

Experimental Design

Contact Angle Measurement

Advancing, receding and sessile droplets were imaged three times each in different areas of the surface using a Rame-Hart contact angle goniometer. In order to ensure reproducibility of results, the droplet volume and the manner in which the needle was inserted into the droplet were maintained the same, as closely as was possible. For advancing contact angle measurements, a 20 μ l droplet volume was the starting point.

Receding contact angle measurements started with a 45 μ l droplet. This resulted in similar final droplet volumes for both advancing and receding. The increment/decrement droplet volume was 0.2 μ l. For sessile drop measurements, a standard droplet size of 25 μ l was used. Between measurement sets, the surfaces were dried at 60°C for 5 minutes in a drying oven.

Contact Angles were measured using the drop snake B-spline method in Big Drop Analysis [26]. The external energy was set to 75/25 gradient/region and the region method to Gaussian. Each image was analyzed twice and averaged to reduce inconsistencies generated from vertex placement.

Submerged Pressure Threshold

One measure of stability of a non-wetting surface is the depth of water for which the surface remains non-wetted. In this case non-wetted refers to the fact that fluid does not penetrate beneath the caps of the structures. The majority of surfaces in this study however, would require depths in excess of those attainable in the lab. Instead, a small pressure chamber was built to allow excess pressure to be added with surfaces covered by approximately 1cm of 18M Ω deionized water. The apparatus can be seen in Figures 3-8 and Figure 3-9. The chamber consists of a glass dish with a pressure inlet on the bottom, an o-ring, and a glass plate all clamped together with two aluminum flanges and a set of screws and bolts. The chamber was originally intended to be used with a camera setup and image analysis to determine the fraction of the surface that had broken through as a function of pressure. Surfaces at partial breakthrough can be seen in Figure 3-9. It however, proved too difficult to get consistent images of the shimmer effect seen with partial breakthrough. Instead, each patterns points of initial and complete breakthrough were recorded based on visual observation.

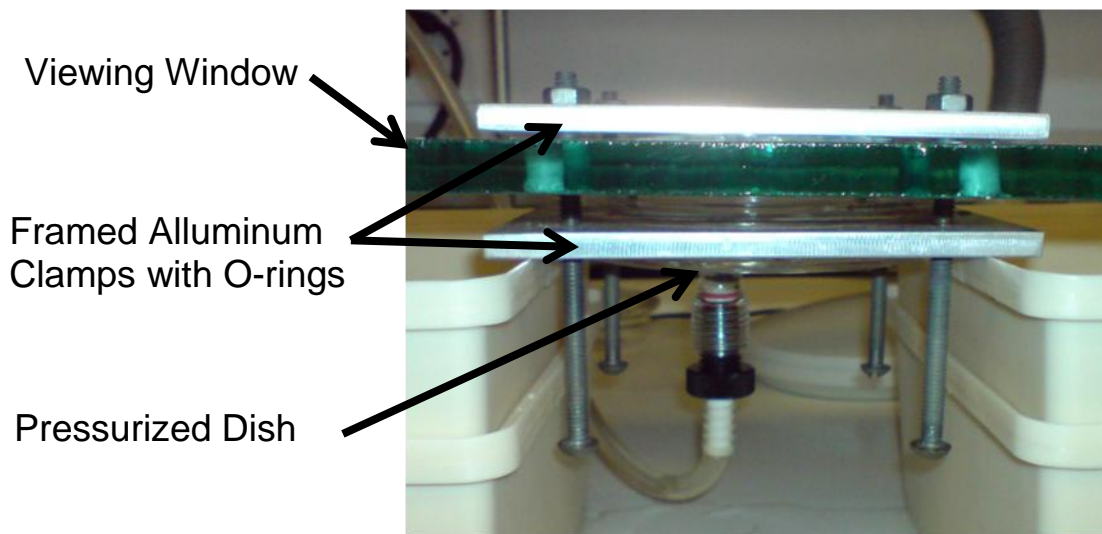


Figure 3-8. Side view of breakthrough pressure apparatus. The pressure vessel consists of a glass dish and viewing window clamped together with aluminum frames and O-rings. Pressure is increased by flowing compressed argon through a fitting added to the glass dish.

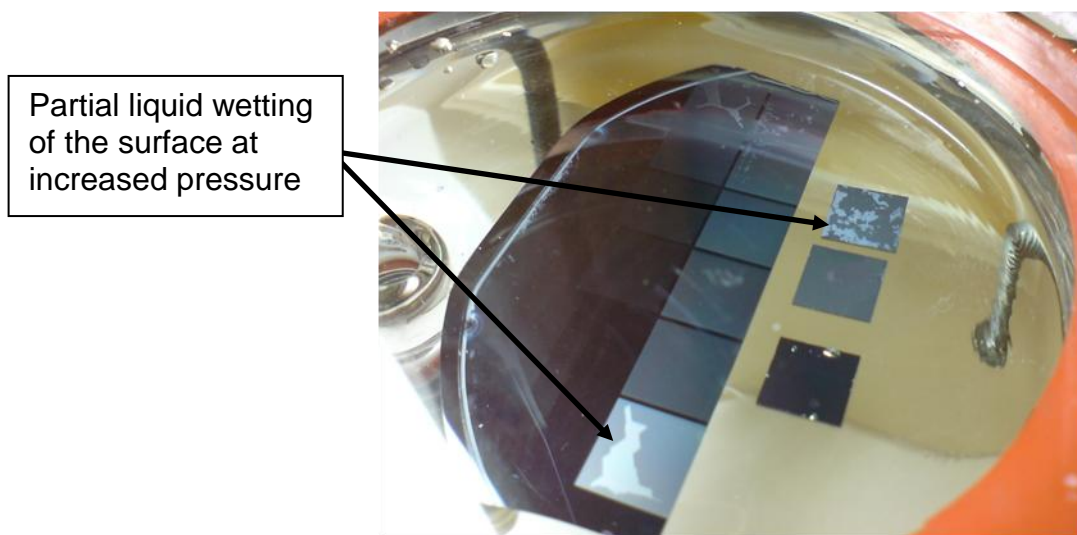


Figure 3-9. Pressure apparatus during a run. While increasing pressure the liquid-vapor interface will eventually wet the underside of the SiO_2 caps. The interface did not break through at a single pressure. The fraction of the surface that had broken through increased monotonically between an initial and final pressure.

A digital pressure transducer with an accuracy of 0.02psi was used. The pressure valve, however, was controlled manually and introduced significant error at the lower

pressures due to difficulty in controlling the rate. This issue was somewhat diminished by the use of replication and averaging of all of the patterns from each etching profile.

Results and Discussion

Contact Angle

Although the advancing and sessile values of the contact angle for these surfaces are expected to be high due to pinning, both were measured to see if any trends could be found. For the contact angle modeling in this work, only the receding values on the discrete surfaces can be used. Figures 3-10 and 3-11 show the combined results of the average advancing, sessile, and receding contact angles on each of the surface variations for the constant spacing series and the constant size series respectively. The lower values of the receding contact angles result in better reproducibility and show no variation due to the profile. This is expected as only the wetted portion of the structure should have an effect on the contact angle and the SiO₂ caps are unaffected by the variations in processing conditions. Contact angle standard deviations ranged from 0.18° to 4.14° with an average value of 1.52°.

The 96µm spacing in Figure 3-11 shows a greater than 40° difference in contact angle between the short and less undercut processing conditions and the standard and tall conditions. This indicates that the higher spacing allows the liquid-air interface between structures to breakthrough resulting in a Wenzel like wetting state.

The advancing contact angles are all in the superhydrophobic regime. This is consistent with the observation by Choi and Tuteja that all surfaces composed of discrete reentrant structures will have ideally 180° contact angles[19]. They attributed the 10-15° lower than expected angle to instabilities and vibrations. The trends in advancing contact angles due however show a slight decrease with the structures larger

than 30-40 μm for every set of measurements made. This indicates a weak but previously unseen relationship between the dimensions of discrete structures and the pinned contact angle values.

Sessile drop contact angles typically follow about 16 $^\circ$ below the advancing angles except in cases where the advancing angle approaches what appears to be a maximum around 166 $^\circ$. For these surfaces, the sessile and advancing angles begin to converge.

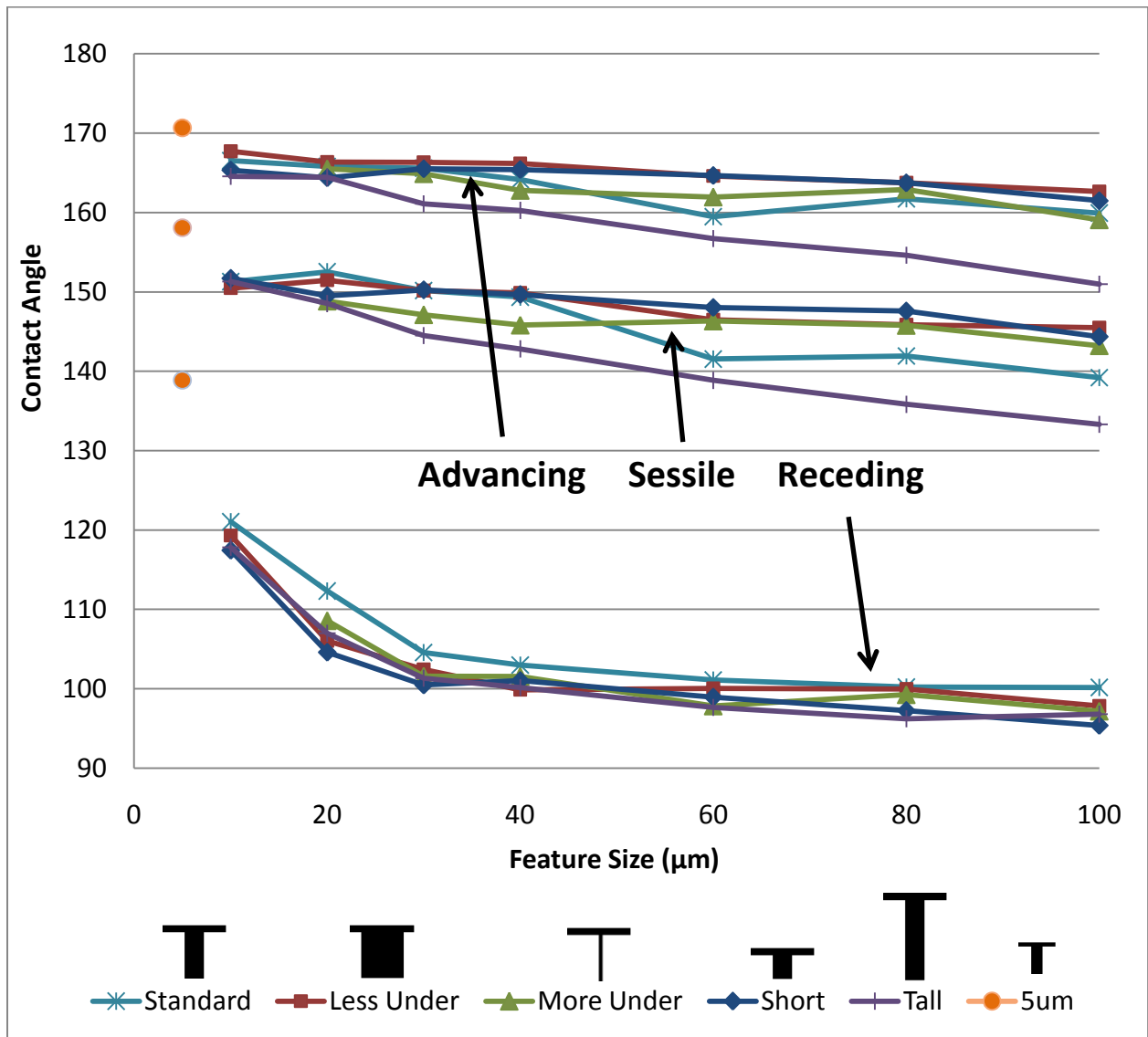


Figure 3-10. Contact angle versus cap size at 3 μm spacing.

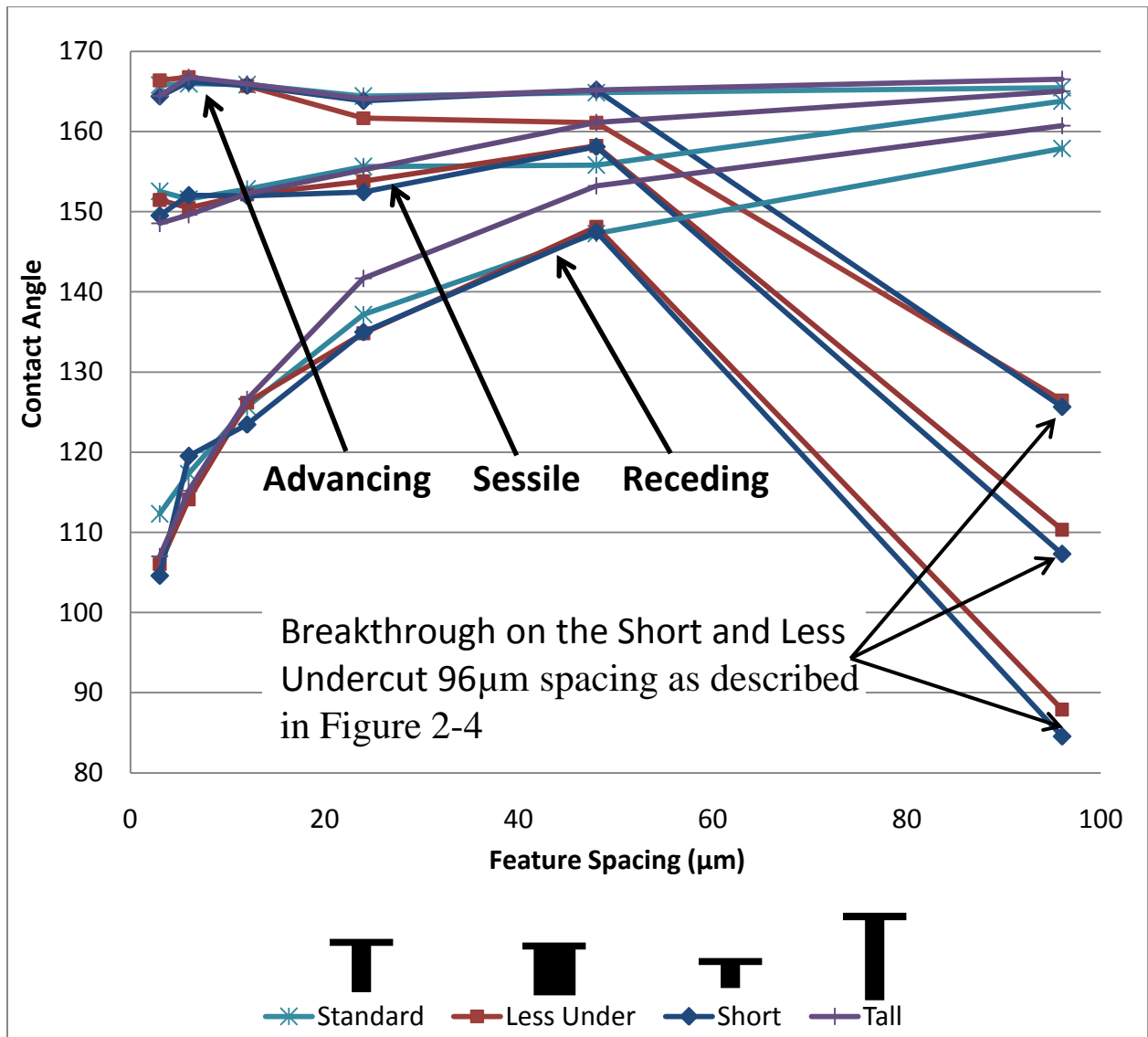


Figure 3-11. Contact angle versus spacing at 20μm feature width.

The relationship between advancing and sessile contact angles can be understood by looking at what happens to the three-phase line during the deposition and subsequent addition to or removal of liquid from a droplet. For sessile droplets when they are being deposited they first make contact with the surface at a single point. As the droplet moves lower, it is analogous to the advancing situation. The three-phase line will expand some distance allowing the contact angle to relax followed by the contact angle increasing again. This cycle will repeat some number of times until the droplet is

fully resting on the surface. At this point, the contact angle will lie somewhere in between the relaxed angle (at the point right after the three-phase line advances) and the advancing angle. This description explains why the sessile contact angles are similar to the advancing but always lower, they are non-maximized advancing angles. It is argued that this result shows that sessile contact angles do not represent one value but instead a value somewhere in a range and that it would be more constructive to use the advancing and receding values. That said the advancing value for discretely structured surfaces are clearly not indicative of the surface energetics or pattern so much as they are simply high due to pinning. This reiterates the previously stated claim that the only angles that are fixed are the advancing and receding.

Contact angles as a function of φ_{cl}

Figure 3-12 is a plot of the wetted fraction of the three-phase line as a function of the radius for the 20 μ m-sized features spaced by 6 μ m. The results for the remaining φ_{cl} -plots can be found in Appendix D. It is clear from all of the plots that the solid or wetted fraction as a function of radius resembles a gradually dampened oscillating system. This made the determination of φ_{cl} easy considering the magnitude and range of oscillation becomes constant before reaching the approximate diameter of droplets (approximately 2.3-2.6mm).

Figures 3-13 and 3-14 show the average receding angle measurements over all of the processing conditions as compared to the current model, the Cassie-Baxter equation, and the modified Cassie-Baxter equation using the square root of the areal fraction (SRA) produced by Choi and Tuteja. It is clear that the use of φ_{cl} in our new equation makes for a better prediction than either the Cassie-Baxter equation or the Cassie Baxter equation modified with the SRA. The use of the square root of the areal

fraction was only actually used by Choi and Tuteja for the square lattice patterns but Figure 3-15 will show that even those patterns do not agree.

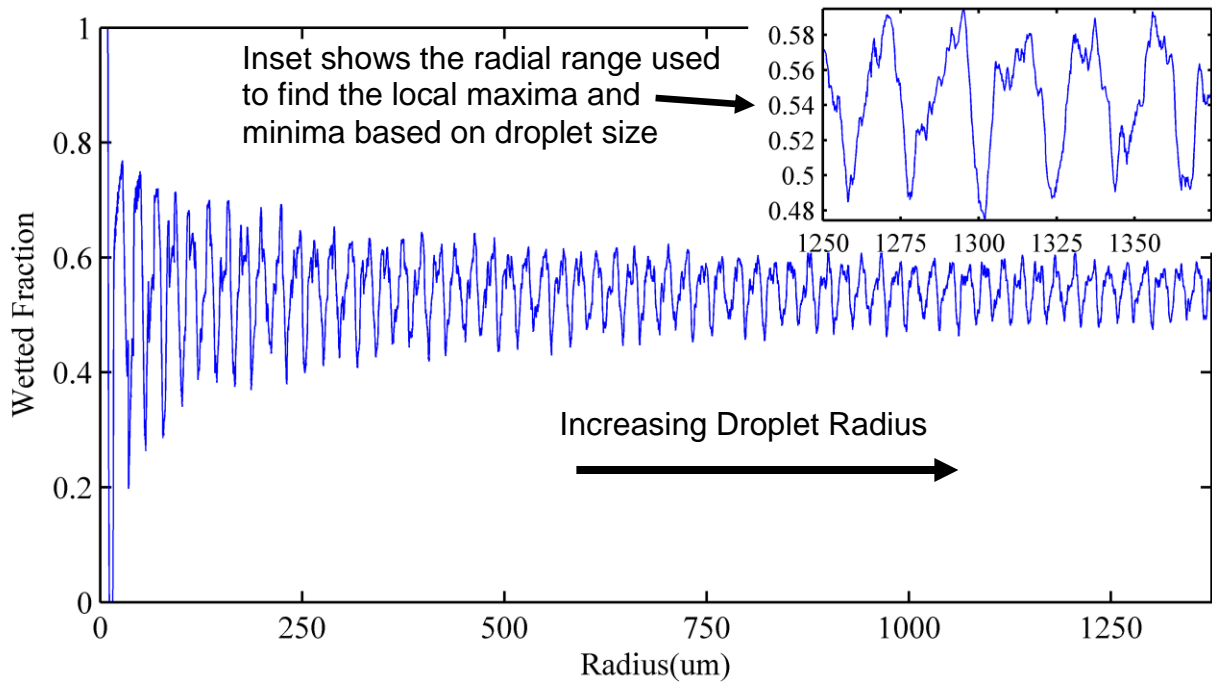


Figure 3-12. 20 μm cap size spaced by 6 μm ϕ -plot. Plot of the actual variation in contact line fraction as a function of radius. Taking the maximum and minimum values near the droplet radius is not sensitive to radial error for larger droplets than approximately 0.75mm.

Figure 3-15 shows the contact angle measurement compared to the predictions by the various models for the additional surface patterns produced. Each of these patterns was created to address a specific question. The square pattern was added as a comparison to the equation produced by Choi and Tuteja[19]. The contact angle is the average of both processing conditions used for the square pattern: standard and tall. This pattern has the same thickness SiO_2 caps, same width, and the same spacing as one of the surfaces that Choi and Tuteja produced to develop their modified Cassie-Baxter equation. The data shows the approximation in their model (equating the three-

phase line front to a straight line) is invalid. In reality the three-phase line will hit the square structures by all angles not just parallel to the flat.

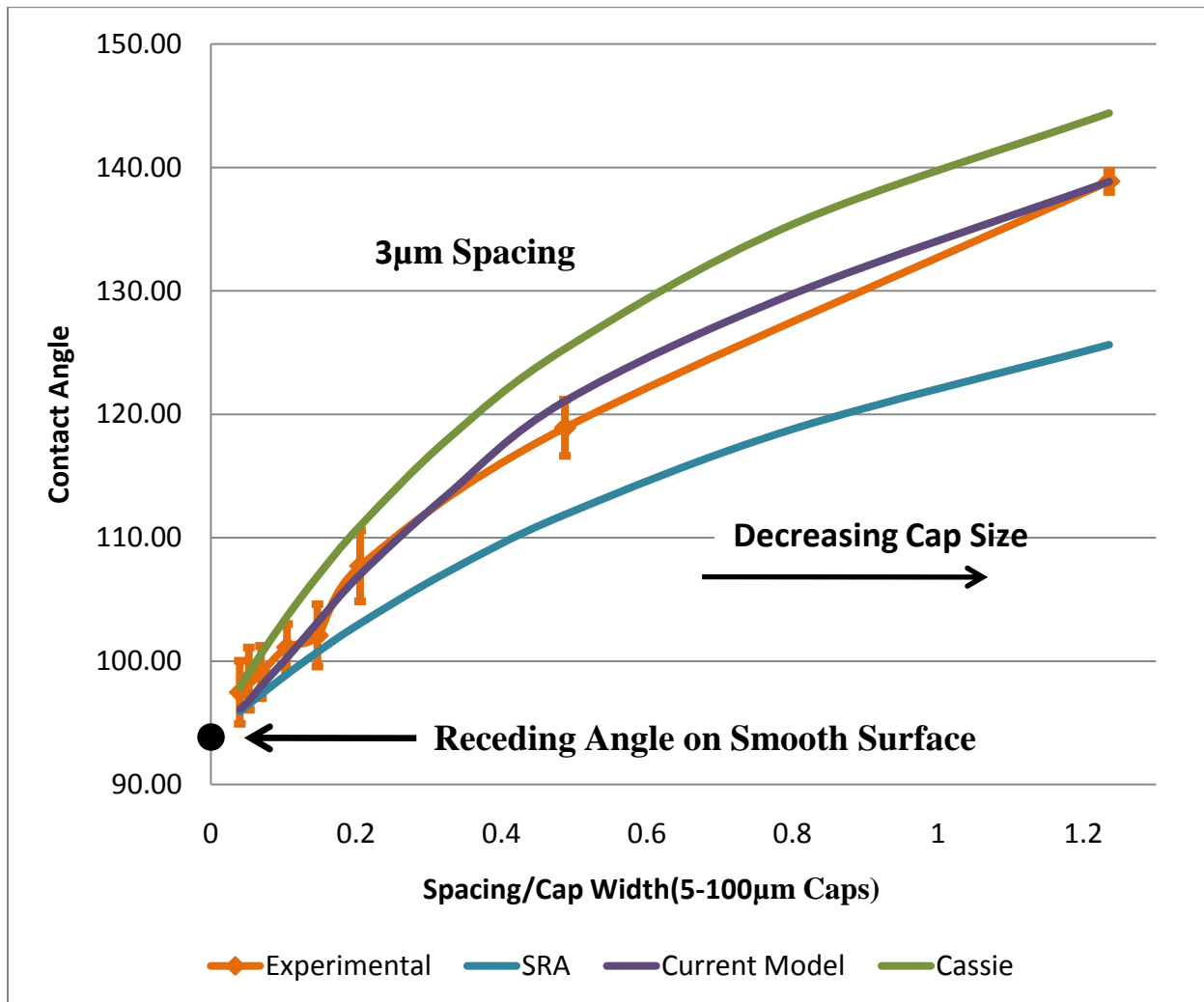


Figure 3-13. Average receding contact angle versus the ratio between spacing and cap width, compared to predictions for the variation in cap size. Comparing the various predictions show that the current model produces results within the standard deviation of each set of measurements while the other equations only fall within the standard deviation as the contact angles approach that of the smooth surface.

The star pattern was created to examine the effect of spreading the area of an individual structure out while maintaining the same areal fraction. The star pattern was intended to be compared to the 20µm hexagonal pattern with 24µm spacing, however,

the star pattern shrank more in processing. The results for the star surface based on SEM measurements are good, however it should be noted that as mentioned in the fabrication analysis the star pattern proved especially difficult to measure the actual dimensions. The tips of the star were reduced in dimension more than the rest of the structure due to the resolution limits of the lithography method used. For this reason the inside vertex measurement was weighted at 75% and the tip to tip length at 25%. This resulted in the best shape match when the SEM image was overlaid with the modeled image.

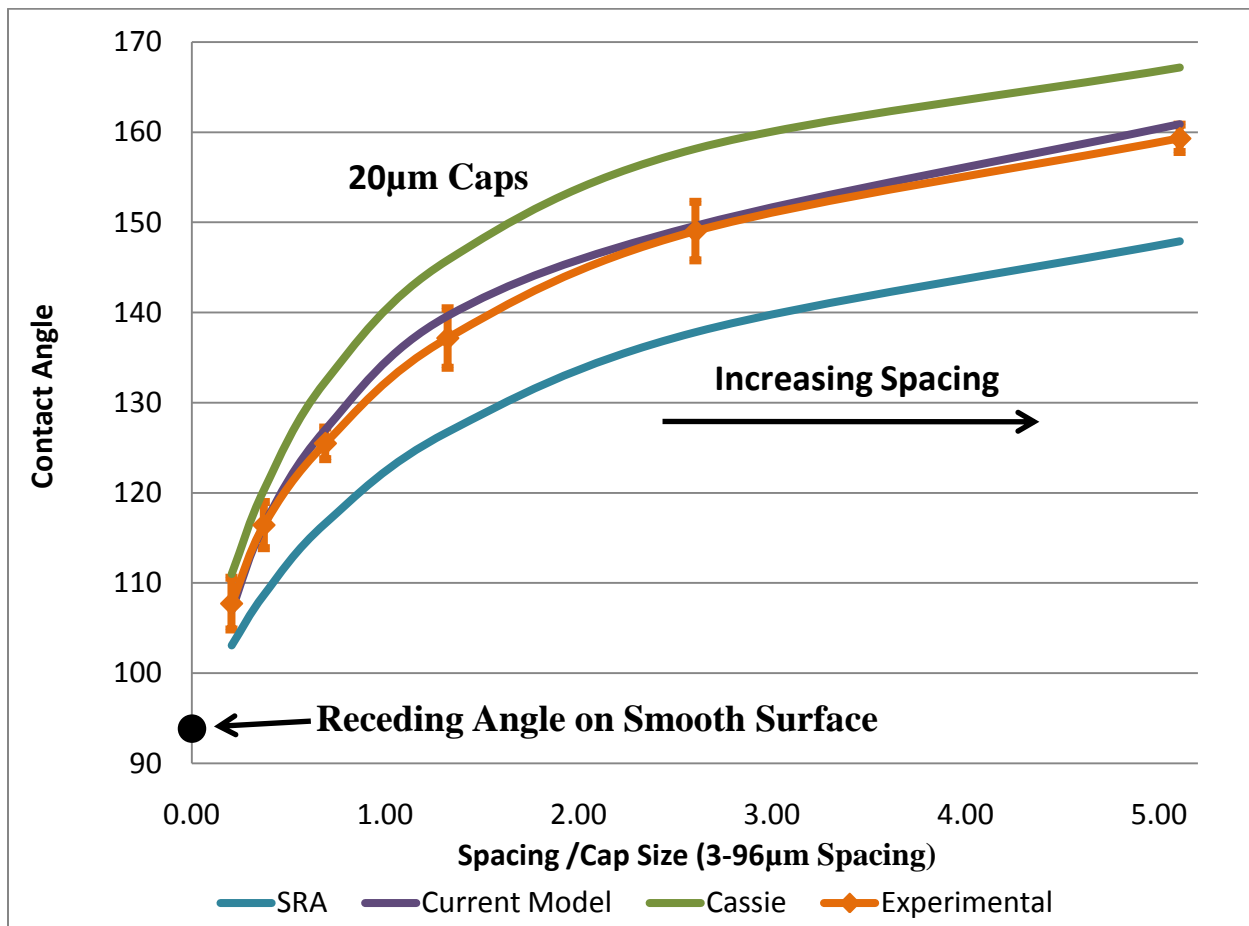


Figure 3-14. Average receding contact angle versus the ratio between spacing and cap width, compared to predictions for the variation in spacing. Comparing the various predictions show that the current model produces results within the standard deviation while the other equations do not.

The final pattern is shown with both the receding and the advancing contact angle. Up to this point no model has been presented for advancing contact angle. This is only due to the fact that all of the patterns thus far have involved discrete structures that pin the advancing angle. The inverse pattern was included for precisely this reason. By using the same method as for the receding angle except using the minimum in φ_{cl} and the advancing contact angle from the non-structured surface, we get a prediction that is very close to the measured value. It is however also very close to the Cassie Baxter equation.

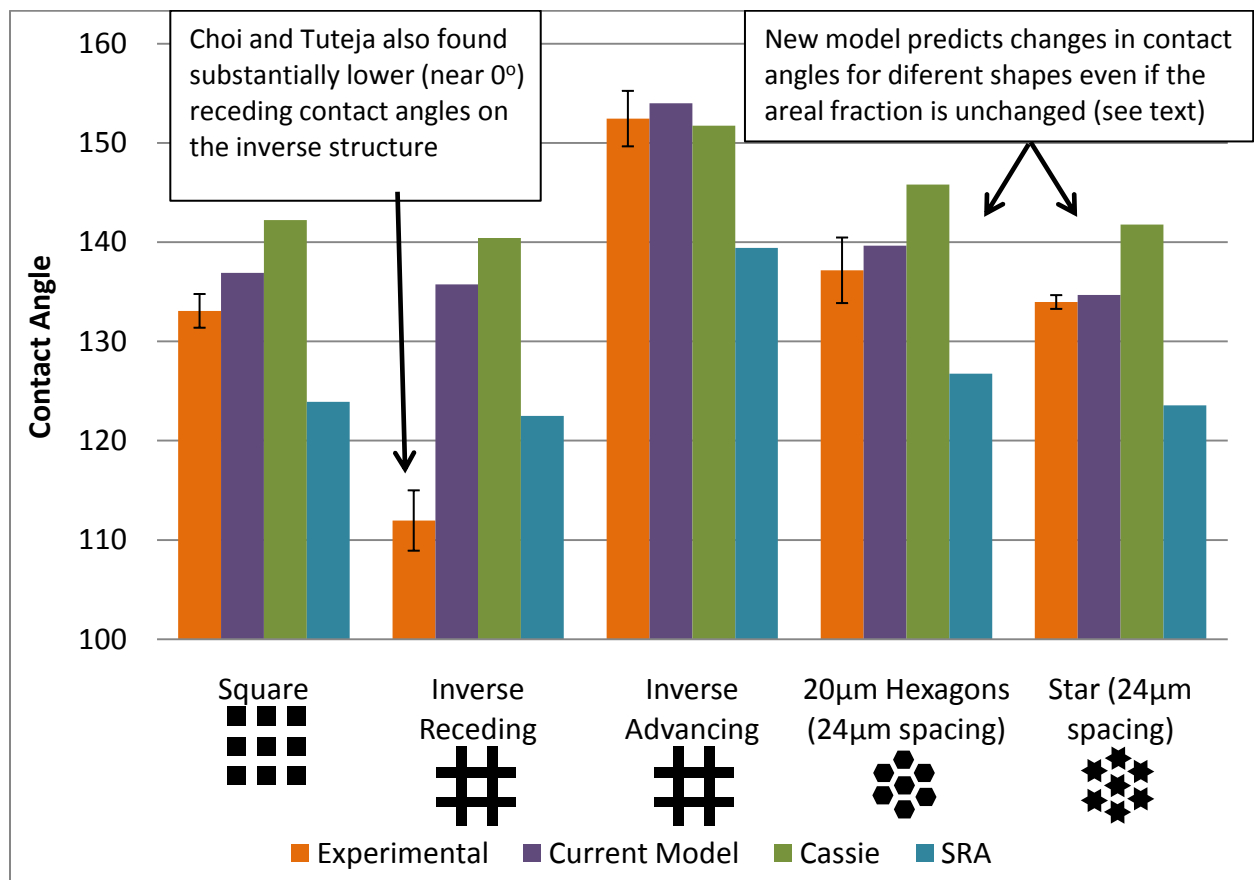


Figure 3-15. Comparison of predictions to data for the square, star and inverse patterns. The square root areal (SRA) fraction used by Choi and Tuteja was developed for surfaces with square geometries. Using replicas of their square and inverse surfaces it is clear that the assumptions made for using the SRA fraction is invalid.

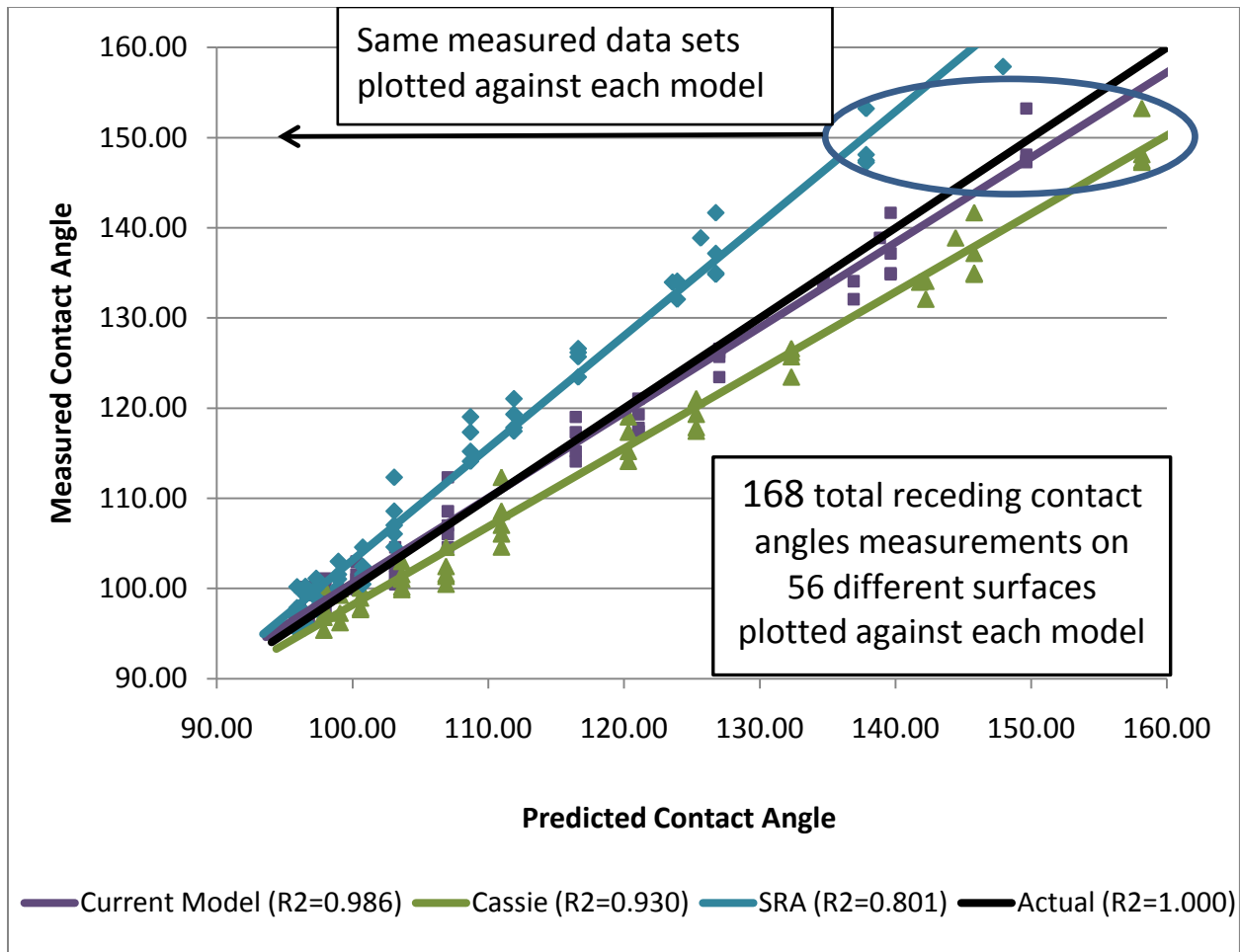


Figure 3-16. Goodness of fit comparison (R^2) of all data points compared to the predictions. The current model can be fit to all of the receding measurements made with significantly less error.

It is believed that running more varied pattern dimensions would also prove the current model to be correct and more accurate than the Cassie Baxter model for advancing angles. The receding angle on the inverse pattern is not well predicted by any of the models. A similar effect, although to a far greater degree, was noticed by Choi and Tuteja. They found that for a similar pattern with smaller dimensions the receding angle was close to 0° . This was believed to be due to a stable film of water forming over the air pockets as the droplet was receding. Further investigation is required to understand this phenomenon.

Figure 3-16 provides the final evidence that the current model is in fact, more correct. Taking all data points measured (excluding those that broke through at the 96 μm spacing) and graphing them against the predicted values it is clear that the current model is significantly better with an R^2 of 0.986 compared to 0.93 for the Cassie Baxter Model and 0.801 for the Tuteja model.

Generalized application to contact angle hysteresis on any surface

The description given for the mechanics of wetting based on minimization of ϕ_{CL} as a function of the radius of a droplet can be similarly applied to all real surfaces. If for instance a surface were coated with patches of different types of self assembled monolayers or atomic force microscopy were used to map out the distribution of defects on a smooth crystalline surface, one could apply the current model if the effect on contact angle of the various phases or defects was known.

Breakthrough Pressure

The results from the breakthrough pressure tests are complicated. Issues including mechanical failure of the SiO_2 caps, damaged samples, difficulty in visually determining the degree of breakthrough and difficulty in manual control of pressure at the low end have made a quantitative comparison difficult. The original idea was to add up or take an average of all of the patterns for a given etching condition and evaluate the effect on breakthrough pressure. A couple of lost patterns from the dicing saw made a global comparison impossible. Figure 3-17 shows the results of using only the 30-100 μm cap sizes for this comparison. Due to the relatively low breakthrough pressure and the similar nature of the patterns, no information can be gained due to similar results and high error.

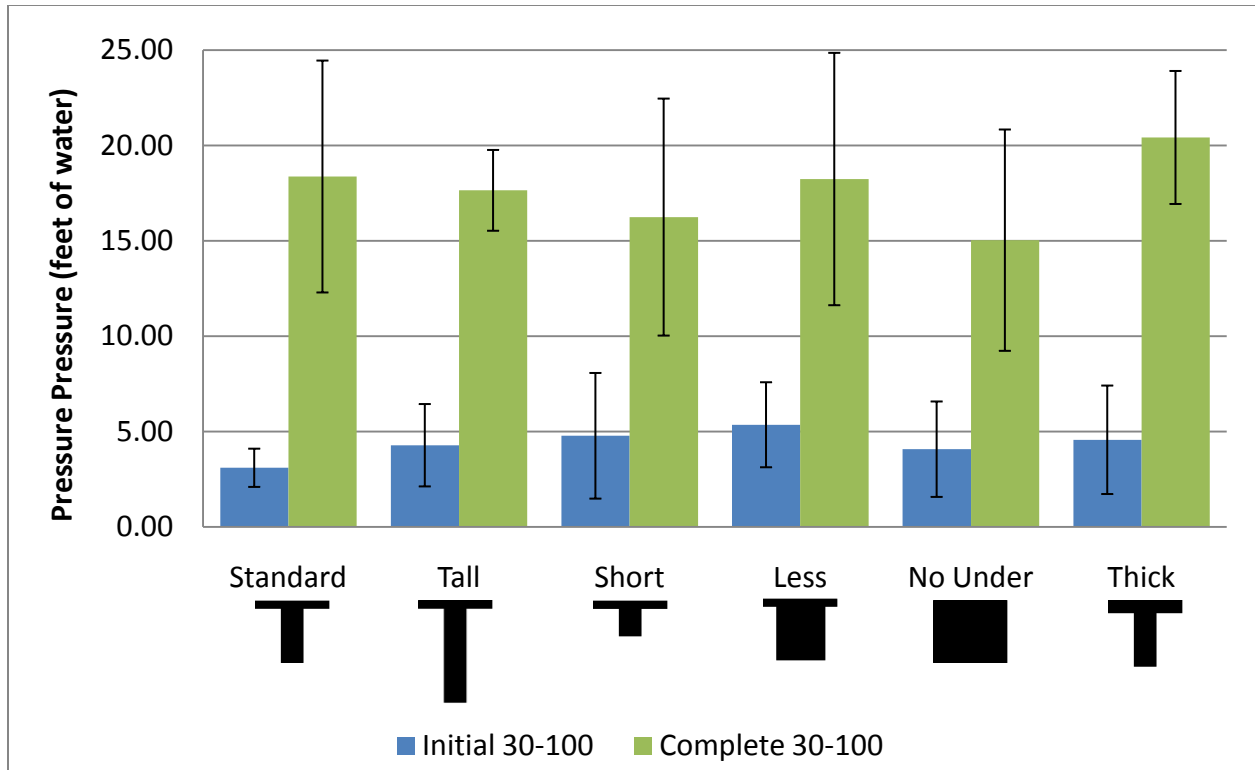


Figure 3-17. Average breakthrough pressure for 30-100µm cap sizes. Due to low breakthrough pressures and high error, no significant trend can be found.

The 20µm cap sizes with spacing between 24 and 96µm typically broke through at atmospheric pressure or slightly above. If however, only the 10µm and 20µm cap size spaced by 6 and 12µm are used then we see trends in the data. In Figure 3-18.

Removing the initial breakthrough values that were too low to show any significant trend gives Figure 319. Here it is appears that the tall structures are the most robust. This is followed by the standard and thick-capped standard structures. The thick-capped structures actually show slightly better average breakthrough pressure and this may be due to greater mechanical strength. The less undercut and shorter structures show the lowest average breakthrough pressures. Data for breakthrough on the more non-wetting surfaces always displayed the same trend. Using an analysis of variance (ANOVA) test combined with Tukey's method for determining significant differences in test results

gives us Table 3-1. Tukey's analysis shows the groupings for each pattern that cannot be said to be significantly different with 95% confidence.

Table 3-1. Tukey's range test of ANOVA data for breakthrough as a function of etch profile. Data for breakthrough on the more non-wetting surfaces always displayed the same trend. Tukey's analysis shows the groupings for each pattern that cannot be said to be significantly different with 95% confidence.

	Etch Condition	Mean Breakthrough Pressure	Grouping
10µm Cap Size	Tall	19.9	A
	Thick Caps	18.1	A B
	Less Undercut	15.8	A B
	Short	14.4	A B
	No Undercut	11.5	B
20x6µm Cap Size	Tall	18.9	A
	Thick Caps	16.1	A B
	Standard	14.5	B B
	Less Undercut	13.8	B B
	Short	13.3	B C
	No Undercut	6.9	C
20x12µm Cap Size	Tall	18.6	A
	Thick Caps	17.2	A
	Standard	15.8	A B
	Less Undercut	12.2	B C
	Short	10.7	C D
	No Undercut	6.3	D

Based on the Tukey results it appears that higher breakthrough pressures can be achieved through use of thicker more mechanically stable caps and taller structures.

The Tukey results for the 20µm cap sizes spaced by 6 and 12µm show that the no undercut profile is significantly worse for preventing liquid breakthrough than all but the short profile. Aside from the benefit of having an undercut, the size of the undercut does not seem to have any effect on breakthrough pressure.

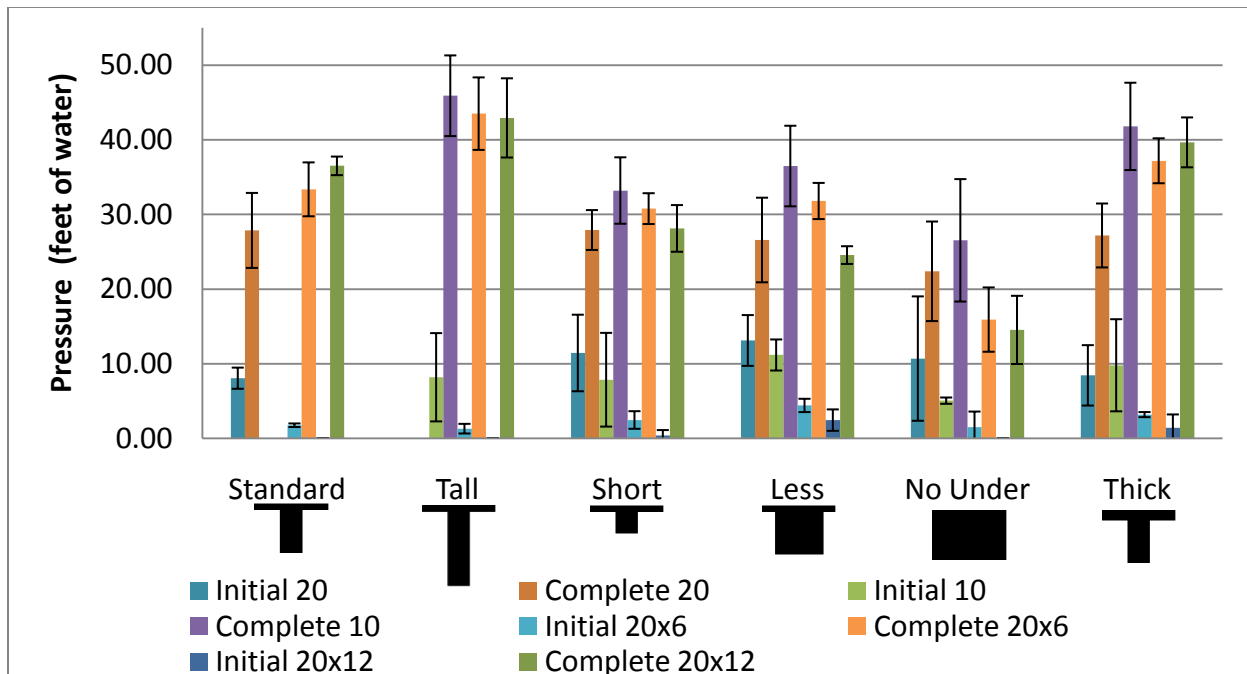


Figure 3-18. Initial and final breakthrough pressures for the four patterns with the highest breakthrough. Initial breakthrough pressures are too low to provide any significant data.

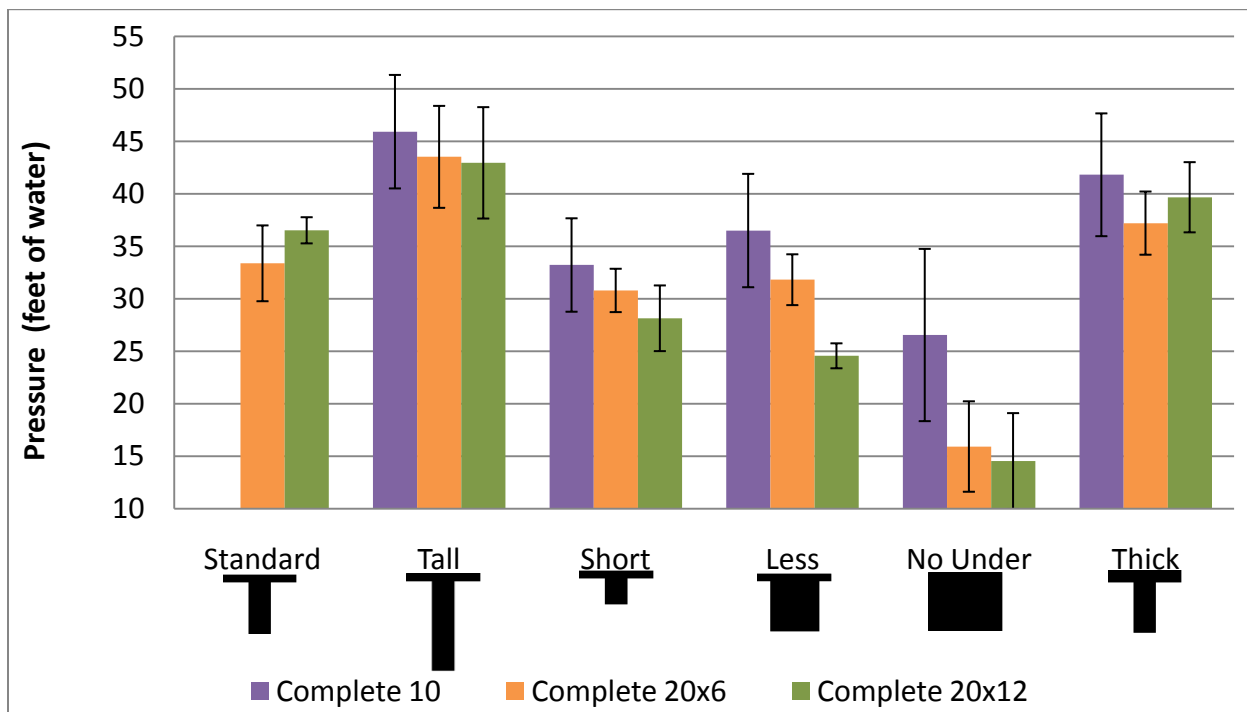


Figure 3-19. Final breakthrough of the three patterns with the highest pressures. Although the error is large some significant trends can be found based on the Tukey's analysis in Table 3-1.

In the future, an automated set-up with a pressure controller and camera will have to be used to reduce error and get results that are more conclusive. This may aid in producing a model to predict the pressure tolerance of non-wetting surfaces.

Wetting Conclusion

The wetting work described in Chapter 3 has demonstrated that a simple model based on numerical simulation of the wetted fraction of the triple point line has a significantly better relationship to the measured data than any model to date. This is significant due to the increasing demand for superhydrophobic surfaces. The ability to control the degree of contact angle hysteresis has also been demonstrated. This control will allow for the production of surfaces with tailored roll off angles, surfaces that will produce droplets with tailored radii of curvature etc.

The resulting accuracy of this model for the entire range of surface measured also supports the argument that the Cassie-Baxter equation is not a valid tool for the prediction of advancing and receding contact angles on structured surfaces. If necessary, the Cassie-Baxter equation can be employed for this purpose but only as a rough approximation. Although the Cassie-Baxter equation can be nearly accurate in certain situations, it is still an incorrect model used for this purpose and creates confusion regarding the mechanisms of wetting on structured surfaces.

Additionally, qualitative data is presented to help elucidate the elements of structure profile that most significantly affect the pressure threshold for submerged superhydrophobic surface. This data may be used for the production of robust biofilm resistant surfaces and anti fouling surfaces.

CHAPTER 4 POOL BOILING HEAT TRANSFER ON REENTRANT UNDERCUT SURFACE STRUCTURES

A general introduction to the applicable pool boiling concepts in this work was given in Chapter 1. In this chapter, we will discuss the evolution of enhanced pool boiling surfaces and investigate the use of discrete reentrant structures as a new type of enhanced pool boiling surface. The boiling fluid used in this work will be FC-72. It is an industrial refrigerant fluid composed of perflourohexanes. It is the most commonly used fluid for these types of boiling experiments due to its dielectric property and its low boiling point of 56°C. The boiling chamber was designed to allow for use with water but the high critical heat fluxes achieved by the enhanced surfaces would have resulted in surface temperatures that melt various bonding materials in the heater block.

Introduction to Enhanced Boiling Surfaces

Enhancements to surfaces used in pool boiling heat transfer can be achieved in many ways. It has long been known for instance that roughening a surface will result in increased heat transfer during boiling. This effect has been rigorously studied and surfaces can be achieved by adding artificial nucleation sites to a surface, and by increasing the total surface area. Simple techniques involving adding fins to tubing are already in use in the refrigeration in all water chillers. Higher efficiency surfaces have been sought for nearly 20 years to cope with the increasing heat flux produced by higher density microelectronics.

Using enhanced boiling surfaces to cool computer chips. Research on enhanced surfaces for use in chip cooling is focused on reduction of the incipience temperature, maximizing CHF and on improving the slope of the boiling curve.

The liquids used must be dielectrics in order to prevent possible electrical issues (particularly capacitors) and reduce possible interference with electronics. Liquids commonly used for cooling of electronics include various liquids invented and manufactured for this purpose by 3M, such as Fluorinert. One of the most common Fluorinert fluids is FC-72 (perfluorohexanes) due to its boiling point (56°C) in relation to typical maximum electronics temperatures (~85°C).

Goals

Chapter 4 will evaluate the discrete reentrant cavities discussed previously for use as enhanced nucleate boiling surfaces. These surfaces are fabricated on a silicon wafers and are therefore compatible with the electronics industry. It is the goal of this work to evaluate the general boiling performance trends and provide a hypothesis to explain the basic mechanisms of boiling on these novel surfaces. The evaluation of boiling trends on enhanced surfaces is often hypothetical due to the complexity and the number of interactions. This is common for enhanced boiling surfaces as exemplified by the conclusion to Anderson and Mudwar's investigation of surfaces covered in square pins (approximately 500µm tall and 300µm across)[54]. They concluded, "Common incipience theories based on cavity radius do not apply to highly wetting fluids such as FC-72" and "Incipience is sensitive to the value of the effective radius of vapor embryos existing within the surface; however, that radius may be a very complex function of surface microstructure and the temperature/pressure history prior to boiling"

Modeling of the parameters of nucleate boiling on enhanced boiling surfaces is typically relegated to simple surfaces with well-controlled and defined parameters, such as polished surfaces with well-defined conical cavities. Honda, in his conclusion to "Enhanced boiling heat transfer from electronic components by use of surface

microstructures ", concluded, "the mechanism of reduced boiling incipience superheat by the surface microstructure is not well understood"

Literature Review

Pool boiling for use in heat transfer is a concept that has been extensively studied starting primarily in the 1920's. Pool boiling heat transfer can depend on many properties including but not limited to: surface temperature, bulk fluid temperature, pressure, fluid properties, and surface properties. The idea that roughness and surface condition can have a major effect on pool boiling started with the works of Jacob and Fritz from 1931 to 1949[55]. In the 1950's, several researchers found that increasing the area density of stable nucleation sites would increase pool boiling efficiency [56-58]. Corty and Foust [57] and Bankoff [59] proposed that efficient bubble nucleation sites would have to trap vapor after the departure of a bubble. This led to relationships describing the minimum superheat (excess temperature above the boiling point) in the liquid required to maintain a convex liquid-vapor interface for a given cavity diameter. Westwater and his coworkers advanced the understanding of boiling on relatively smooth surfaces using high speed cameras and solutions of Nickel salts, which leave behind non-platted areas at nucleation sites, to study the nucleation site density as a function of heat flux[60, 61]. A fundamental understanding of individual nucleation sites was provided by Griffith and Wallis[13]. They studied the relationship between cavity size and superheat required to nucleate vapor from a single cavity after roughening surfaces with emery cloth. Specifically, they found that the shape of the cavity could affect the stability of the trapped vapor. They proposed that a reentrant cavity would possess a concave liquid-vapor interface and that this would allow for a stable vapor pocket even with a sub-cooled liquid. This was described in Chapter 1 Figure 1-9.

Benjamin and Westwater were the first to actually construct reentrant cavities and demonstrate their superior trapping ability[62]. Nakayama et al. worked on a pore and tunnel type surface formed by bending a notched fin until it contacted the next fin[63, 64]. They proposed three modes of boiling. The first is a low heat flux mode where the tunnel is flooded and vapor trapping and nucleation take place only near the pore itself. This is followed by a high heat flux mode where the departure of bubbles from pores causes a suction and intake of fluid at other pores. At very high heat flux, they propose the tunnel is dried out and the liquid supply only occurs at the mouth of the cavity.

In the 1960's commercial applications for enhanced boiling surfaces began with simple techniques such as adding a 0.25mm thick sintered Copper layer to a surface (HIGH-FLUX™) or by adding large fins to surfaces (such as the Thermoexcel™, GEWA™, and the ECR-40™). Since this time, extensive research has been performed leading to more detailed and often contradictory theories involving pool boiling. Webb provides a continued review of the macroscopic commercial approaches aimed at large scale industrial uses[65]. For a review of the current literature involving pool boiling fundamentals on polished and roughened surfaces, Piore and Rohsenow provide both the most accurate pool boiling model to date as well as a review of the previous literature[66, 67].

More efficient enhanced pool boiling surfaces have been studied extensively over the past 20 years. These surfaces include macroscopic cavities, pins and fins, fiber coated surfaces, porous surfaces, and microscopic structured surfaces made using microelectronics processing techniques.

Newer macroscopic techniques have been demonstrated including a parametric study of silicon and copper finned and multi layer finned surfaces by Ramaswamy[68]. Reed used layers of spheres pressed against flat smooth surfaces to produce a type of reentrant cavity boiling surface in an attempt to reduce the incipience temperature[69].

Messina[70] and Miller[71] used photolithography and chemical etching to produce cavities on boiling surfaces. Goyal used a similar technique but then bonded wafers together producing reentrant cavities[72]. Kubo produced reentrant cavities by coating the surface with a thin layer of a material (similar to the SiO₂ caps used in this work) and then etching small holes through the layer. He then isotropically etched into the surface through the holes using a plasma that would not etch the surface layer. Honda has published a number of papers describing boiling on micro pin fins[73, 74]. These are simple surfaces with raised square studs.

Bhavnani et al. have extensively studied boiling heat transfer as a solution to microelectronics cooling [75-79]. Most of this work involves flow boiling although Nimkar's paper[78] on the effect of nucleation site density on surfaces structured with reentrant cavities found average CHF values of 12.7W/m². This value is unusually low and near the CHF for smooth Silicon. Garimella et al. recently addressed the "Thermal changes in next-generation electronic systems"[76].

Fiber coated and porous surfaces have been of great interest over the past 10-15 years. This is attributed to the random distribution of effective pore sizes that allow stable nucleation at a range of superheats. Fiber coated surfaces have been produced using TiO₂ nanofibers[80], carbon nanotubes[81, 82], and carbon nanotubes on raised pin fin structures[83]. Porous surfaces have been produced using silver, diamond,

copper, and aluminum particles with a binding media [84-86]. Other porous surfaces have been produced using porous layers of graphite [87, 88]. The biggest issue with the current state of research is that micron scale porous and fiber coatings that have been produced up to this point are complex and nearly impossible to model other than using empirical approaches.

Pool Boiling Apparatus

Heater Assembly

The heater shown in Figure 4-1 is comprised of a copper block with a 1-cm² cross section. Four type E thermocouples are embedded 4 mm deep along the side of the heater at 2.5mm, 7.5mm, 12.5mm and 17.5mm from the surface. Solder (S-BOND 400) with a melting temperature of 400 °C, is used to bond the sample to the heater. The thermocouples were calibrated using a constant temperature bath. All of the thermocouples had an error in accordance with the NIST standard for type E thermocouples. A 100 W cartridge heater is inserted in the bottom of the heater block. For mounting to the chamber a PEEK flange is attached to the heater block near the top most thermocouple using a low thermal conductivity epoxy ($k=1.87\text{W/m-K}$). PEEK is a high temperature plastic with a low thermal conductivity ($k=0.25\text{W/m-K}$). This allowed helped to insulate the heat flow into the chamber other than through the substrate. Substrates were soldered to the top surface using another high temperature solder, S-BOND 220 with a melting temperature of 220°C. Again, this assures that there is excellent thermal contact between the heating block and the heating surface. After soldering the substrate onto the heating block the lateral portions of the heating block and substrate were encapsulated in a high temperature, low viscosity and low thermal conductivity epoxy Duralco 4460 from Cotronics ($k = 0.57 \text{ W/m-K}$). The low viscosity of

the epoxy assures adequate surface coverage for the lateral portions of the substrate. A second coat of epoxy was used to cover bubbles left from the first coat to prevent nucleation from cavities present in the epoxy.

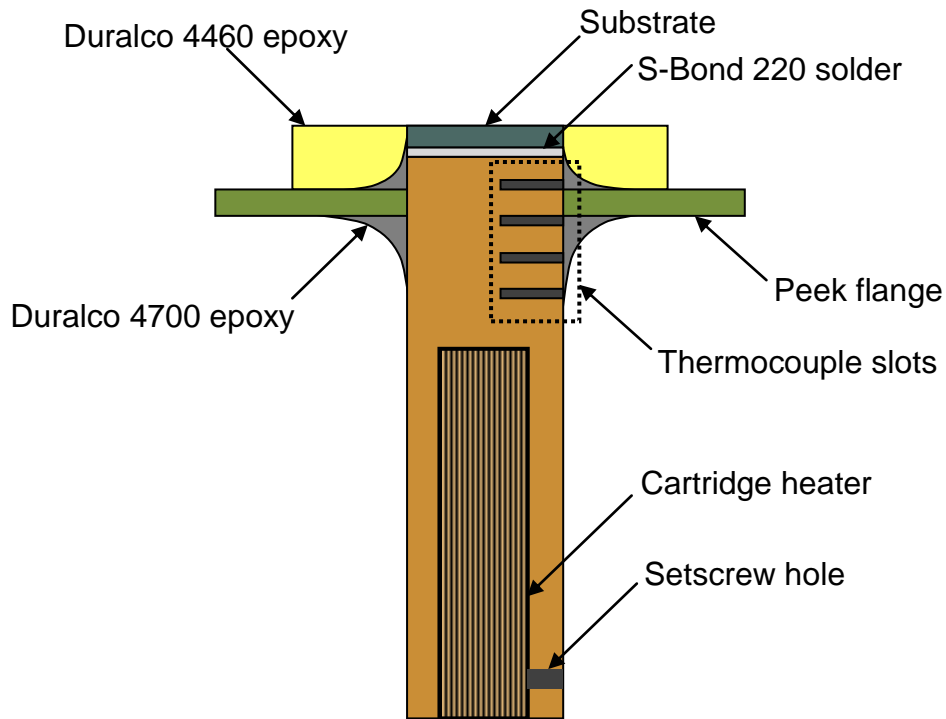


Figure 4-1. Heater Assembly. The heater is composed of a Copper block, cartridge heater, and various thermally insulating bonding materials to allow for attachment to the pool boiling chamber.

The lower portion of the heating block was wrapped in fiberglass insulation during the experiments to achieve low heat loss. At less than 5% loss, one-dimensional heat flow in the heating block can be assumed. The surface temperature was extrapolated using a least squares fit of the measured thermocouple temperatures with respect to location within the heating block. A small correction to the surface temperature was used to account for the thermal resistance across the solder and substrate; however, this was less than 5°C with the most extreme heat flux applied. The thermal resistance

was determined through calibration. The measured voltage and current supplied to the cartridge heater from the variable transformer is used to determine the applied heat flux.

These materials and the heating block configuration allowed for reuse of a single heater for multiple substrates. Attempts were made to use higher temperature bonding materials and solders but issues such as strength and the ability to remove or dissolve the material prevented their use. To achieve higher temperature tolerance and boiling fluids with higher boiling points it would be necessary to build and calibrate a new heater block for each sample.

Pool Boiling Chamber

The pool-boiling chamber shown in Figure 4-2 was constructed from two stainless steel plates and a Pyrex glass cylinder with viton o-rings to form a tight seal. A helical bulk fluid heater was inserted through an opening in the lower plate. This heater shape allows the fluid to reach saturation faster as well as minimize the strength of convection currents in the test chamber. A condensing coil was built into the chamber to maintain the desired pressure and maintain a constant liquid level height by adjusting the cooling flow. A needle valve located on the outlet of the condensing coil allowed for fine increments of the condenser flow rate. Additionally, the bulk heater power can be controlled with a variable transformer so that the minimum required power can be set to assure that background convective turbulence is minimized. Pressure in the chamber was measured with a pressure transducer that was calibrated for the desired pressure range in the chamber. Bulk fluid temperature was measured using a thermocouple located near the chamber floor; this assures that the measured bulk temperature was that near the heating surface. The bulk fluid thermocouple was also calibrated using a constant temperature bath. All thermocouples were in good agreement with their

standard curves.

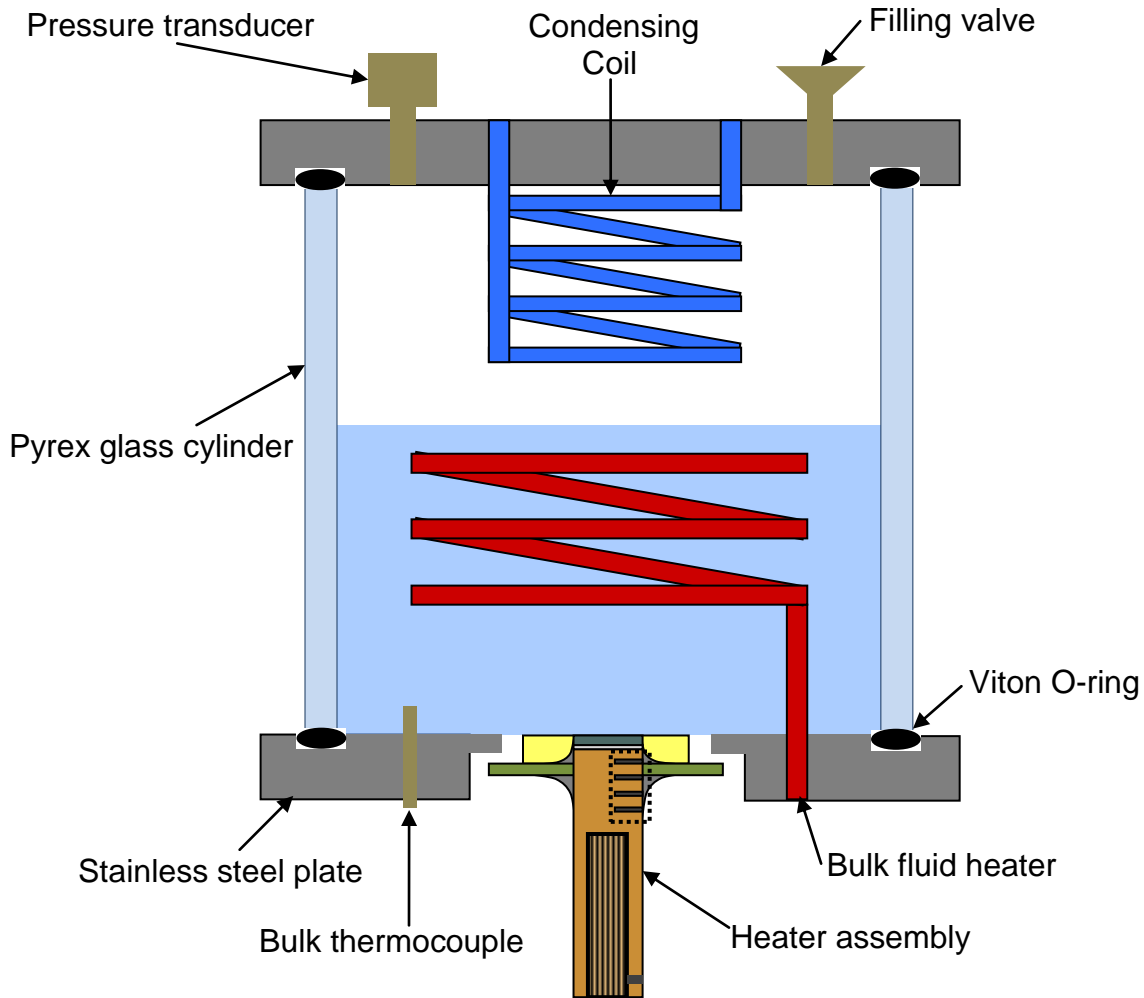


Figure 4-2. Pool boiling chamber. The pool boiling chamber provides a bath that is saturated at the boiling temperature, minimal fluid flow near the substrate (that is not produced by the heated substrate), and pressure control (by balancing the bulk fluid heater voltage and the condensing coil flow rate).

Data and Image Acquisition

A national instruments data acquisition board, NI-6218, is used to collect the thermocouple voltages and pressure voltage. A Labview virtual instrument is used to observe and collect the experimental data. A reference junction circuit is used to measure the junction temperature accurately. This is used to determine the true thermocouple temperatures. Data are sampled at 1 kHz to assure accurate

representation of any significant transient events. The voltage and current applied to the cartridge heaters is recorded at steady state for each point on the boiling curve. To assure quasi-steady conditions preceding transient events, like incipience and critical heat flux (CHF), voltage increments are kept to one volt until such events occur. All recorded data were then post-processed using MATLAB to produce the boiling curves. Additionally a NAC high-speed camera operating from 500 to 3000 fps is used to record the incipience events.

Procedure

After filling the chamber with the desired test fluid, the bulk heater is adjusted to a level sufficient to produce vigorous boiling. The condenser valve remains closed to prevent any excess water vapor from the air initially contained in the chamber from condensing. The chamber pressure increases and non-condensable gases are purged by opening the fill valve. The procedure continues until visual inspection confirms that only vapor from the test fluid is present. The condenser valve is then gradually opened until the chamber pressure reaches one atmosphere. Upon reaching saturated conditions, the surface heater is set to a heat flux 80-90% of the expected CHF for the test fluid. The high applied heat flux assures that almost all potential sites on the surface are active so that any adsorbed foreign particles or gases are carried away by the vigorous boiling at the surface. The surface is degassed at this heat flux for approximately one hour, after which the surface is cooled to below the saturation temperature to assure that any remnant vapor condenses.

For a given test fluid, the initial applied voltage to the heater is set by requiring the observed temperature differences between the thermocouples to be greater than the known error in the thermocouples. This is only a concern at low heat fluxes, where

temperature gradients in the brass heater are observed to be small. The applied voltage is then increased in one-volt increments until incipience. This gradual increase in applied voltage assures quasi-steady conditions during step increases in heat flux. This assures minimal error when using a steady state assumption in extrapolating surface temperatures preceding highly transient events like incipience and CHF. After incipience, the magnitude of voltage increments is increased depending on the test fluid. Approaching CHF, voltage increments are then decreased to one-volt increments, again assuring quasi-steady conditions during step changes. Repeatability studies have confirmed that heat transfer performance from test to test does not change even for studies conducted more than twenty-four hours apart. Experiments were conducted to assess the repeatability of the soldering process; it was observed that the wall superheat for a given applied heat flux varied less than 10% for different soldering applications.

Results and Discussion

For comparison to results from previous researchers, a Figure 4-3 from Wei and Honda's work on micro pin-fins has been included. This includes data from Anderson and Mudawar and from O'Connor et al. [54, 89, 90]. This data was for FC-72 and saturated boiling (same as this study). Data on the reproducibility of boiling curves can be found in Appendix E. During boiling of the discrete reentrant structures there were no distinct temperature drops associated with the onset of nucleate boiling. It appeared instead as if individual regions would begin to nucleate. This sometimes resulted in a number of small drops in temperature on the boiling curve as new areas of the pattern began boiling. This may be due to the expected enhanced entrainment causing colder

fluid to be pulled toward the surface around a vapor-producing site causing the temperature in the neighboring areas to drop.

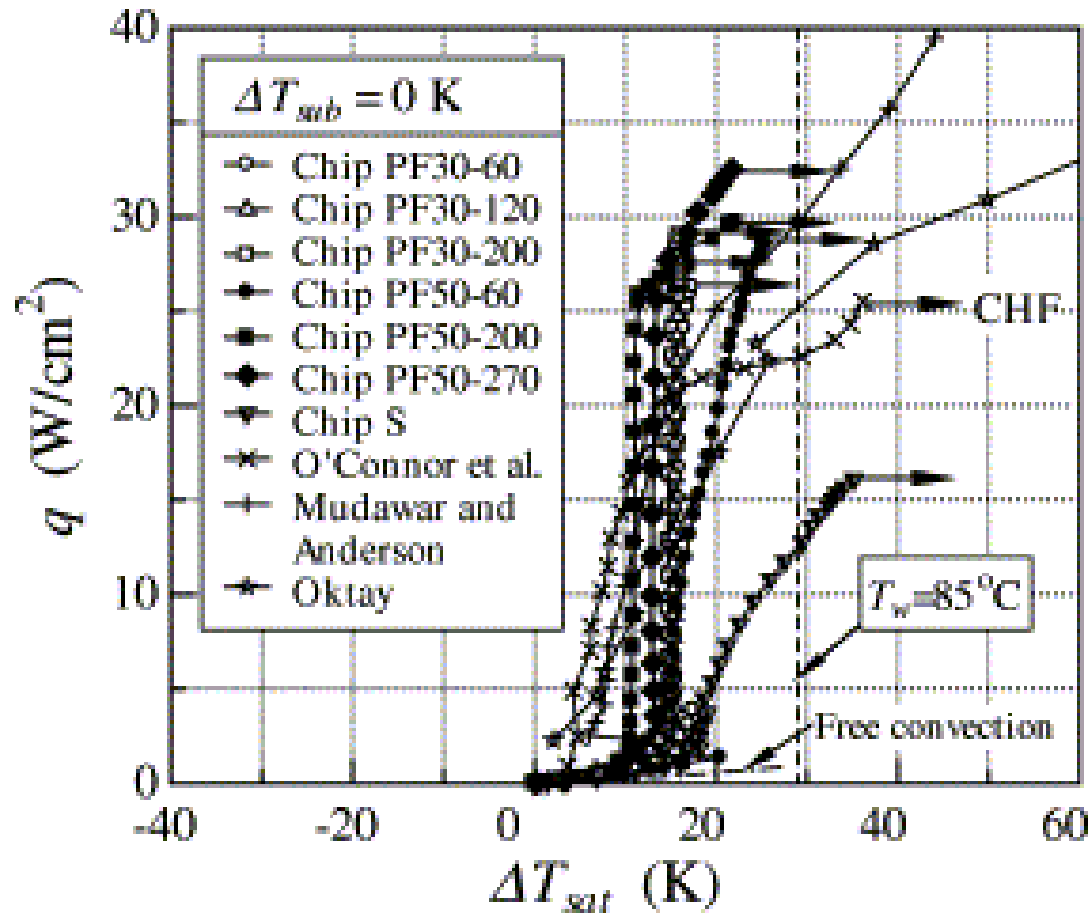


Figure 4-3. Boiling curves for the enhanced surfaces produced by Honda and Wei, Anderson and Mudawar, and O'Connor. These results indicate some of the best performing enhanced boiling surfaces with FC-72.

Size and Spacing Variation

Cap size variation. Figure 4-4 shows the boiling curves for the variation in cap size with a constant spacing of 3 μ m. The 20 μ m cap size shows the best performance with a decrease in performance for sizes above and below. The 20 μ m cap size also shows the highest performance in CHF for the variation in cap size.

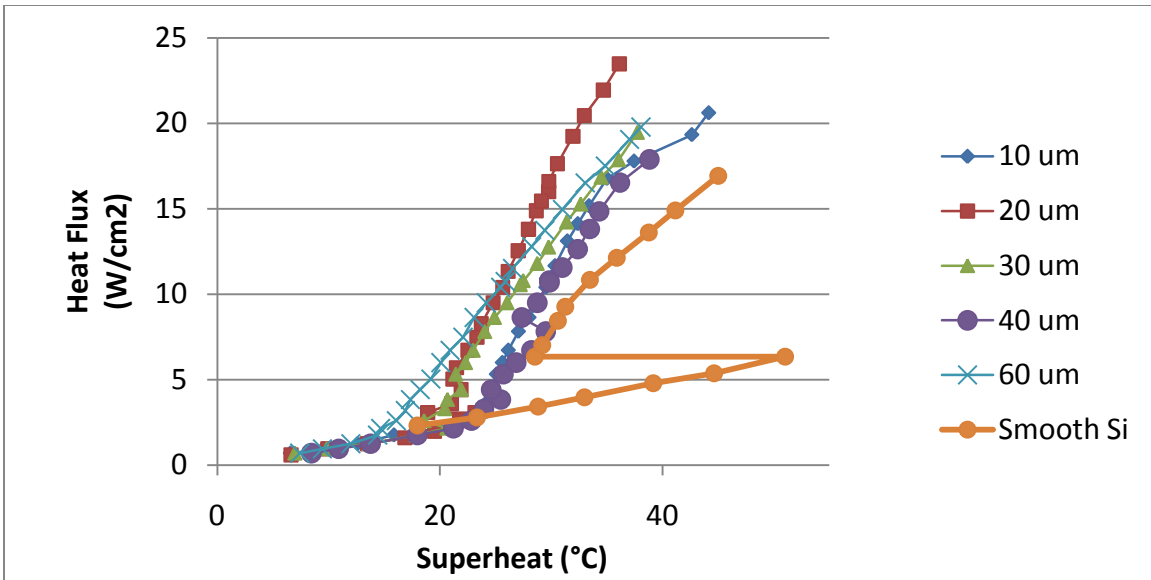


Figure 4-4. Boiling curves for the various cap sizes at a constant spacing of $3\mu\text{m}$. the $20\mu\text{m}$ surface shows a peak in both CHF and heat transfer coefficient. This is likely due to enhanced liquid entrainment and an increase in the length of the three-phase line.

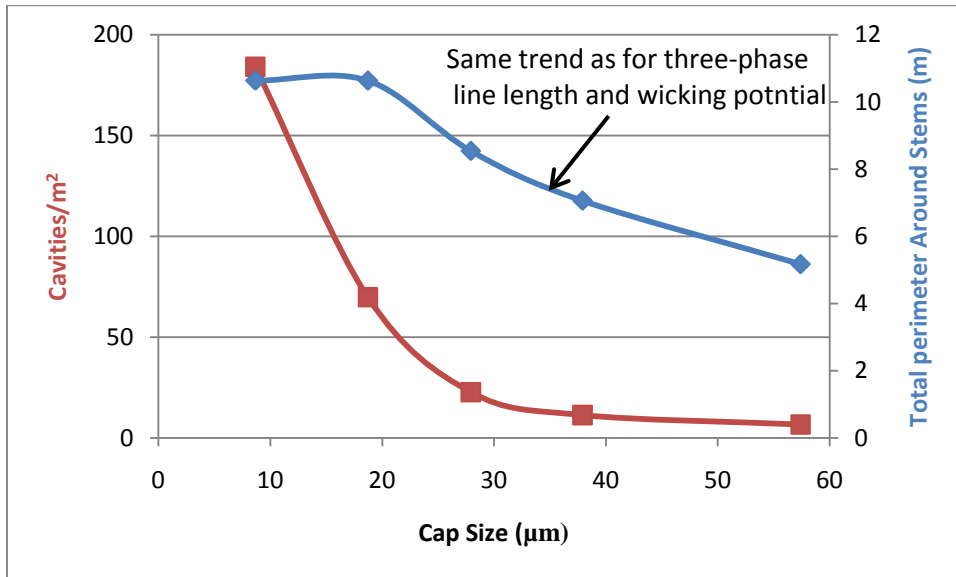


Figure 4-5. Expected trends as a function of the measured cap sizes with constant spacing of $3\mu\text{m}$. Based on an expected decrease in wetted perimeter, number of cavities, and wicking potential it is expected that increasing the cap size will decrease boiling performance.

To understand the results, those parameters that change as a function of cap size and affect boiling should be discussed. When increasing the cap size the number of cavities

on the surface, the perimeter of the stems (related to the increase in three-phase line length as shown in Figure 1-10), and the wicking potential of the surface will decrease as shown in Figure 4-5. These expectations however, did not match up with the actual trends. Further analysis can be provided by plotting the heat transfer coefficient at three different heat fluxes as a function of the number of cavities on the surface, as shown in Figure 4-6. These heat transfer coefficients were all take from a least squares fit of the relatively straight portion of the nucleate boiling curve.

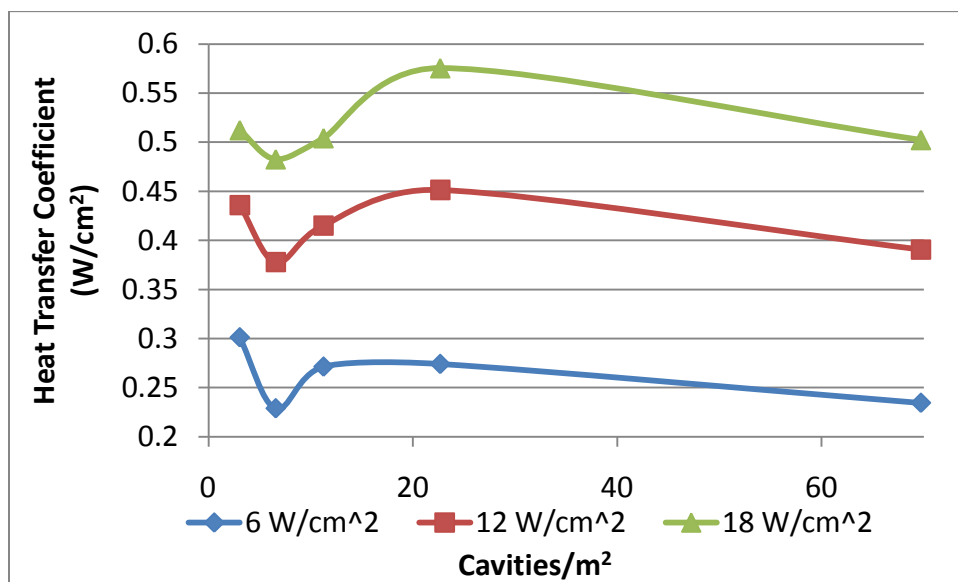


Figure 4-6. Heat transfer coefficient for constant cap size at three different heat fluxes as a function of the number of cavities on the surface.

Figure 4-6 shows that the unexpected behavior of the larger cap sizes begins to go away at higher heat fluxes. The reduction in heat transfer coefficient for the surface with the largest number of cavities is however, unexplained. One possible answer may be that the mechanical strength of the smaller structures on that sample was low enough to allow more damage to the surface. This was difficult to quantify with SEM imaging due to a large amount of surface damage experienced during the removal of the sample

from the heating block. A similar plot to 4-6 as a function of the total perimeter of stems on the surface (not shown), shows very little variation.

Spacing variation. Analysis of the variation in spacing is more complicated. As spacing is increased both the number of cavities on the surface and size of cavities on the surface change as shown in Figure 4-7. This is because spacing was defined as edge-to-edge distance not center-to-center distance for the structures. In the future, this may be a more beneficial way of preparing the surfaces. In addition to the size and number of cavities, increasing the spacing will also decrease the perimeter around the structure stems. This in turn alters the wicking potential.

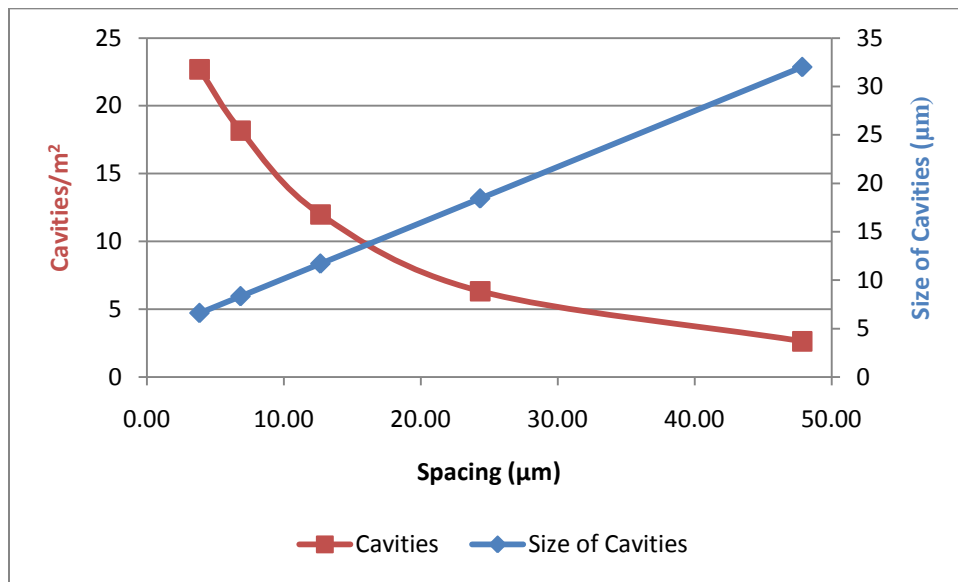


Figure 4-7. Expected trends in boiling as a function of spacing.

Figures 4-8 shows the boiling curves for the 20μm cap sizes with spacing from 1.5-48μm. There is a decrease in heat transfer performance from 1.5-12μm followed by an increase for the 24 and 48μm surfaces. Plotting the heat transfer coefficients as a function of cavity density on the surface as shown in Figure 4-9 or by similarly plotting as a function of increased perimeter or size of cavities, shows a slight u shape trend.

This is consistent with the expectation that multiple boiling parameters will trend in opposite directions.

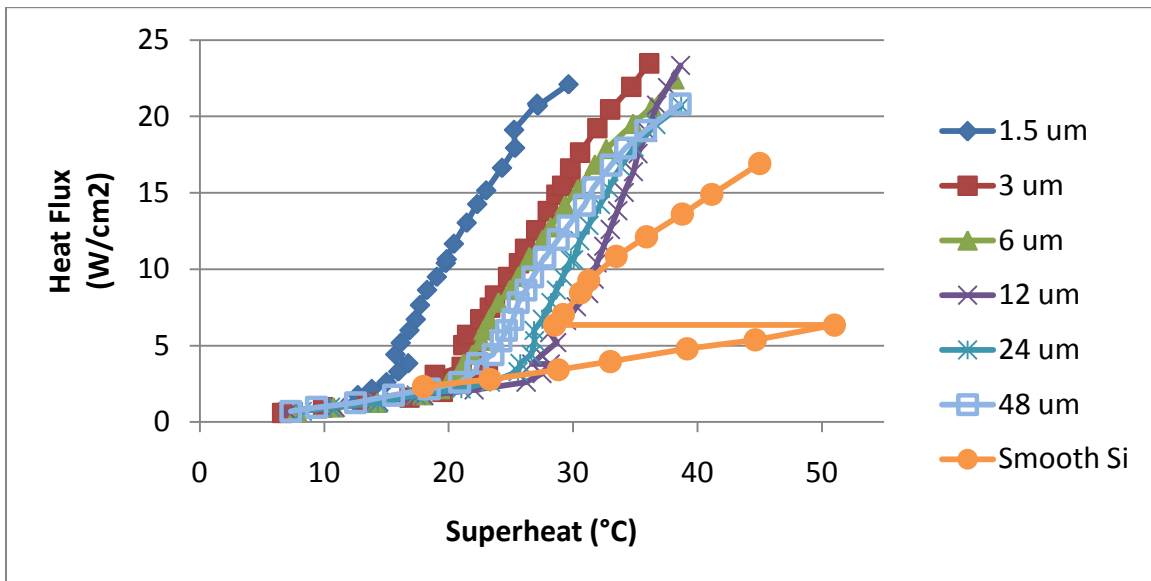


Figure 4-8. Boiling curves for the variation in spacing with 20μm cap size. Significant improvement in boiling performance can be found for the smaller spacing.

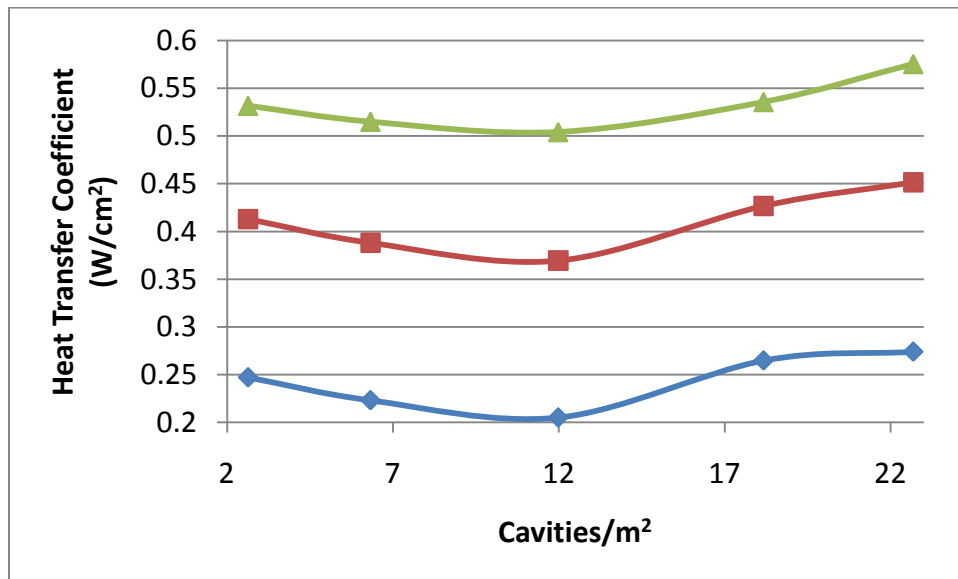


Figure 4-9. Heat transfer coefficient for constant spacing at three different heat fluxes as a function of the number of cavities on the surface.

Critical heat flux. Critical heat flux has been significantly improved. The best surface has a CHF that is 39% higher than on smooth Silicon. Additionally the higher

CHF occurs at 36.12°C instead of 45°C in the case of smooth Silicon. For the variation in cap size, the critical heat flux is highest at $20\mu\text{m}$. Plotting the critical heat flux as a function of the cavity density or length of structure perimeter produces no apparent trend as shown in Figure 4-10. For the variation in spacing, the CHF values for the $1.5\text{-}12\mu\text{m}$ spacing are the highest as shown in figure 4-11. As previously mentioned, increasing the spacing results in a decrease in the structure perimeter, wicking, and number of cavities and an increase in the size of the cavities. Although as previously mentioned the larger spaced surface are not likely to be acting as cavities.

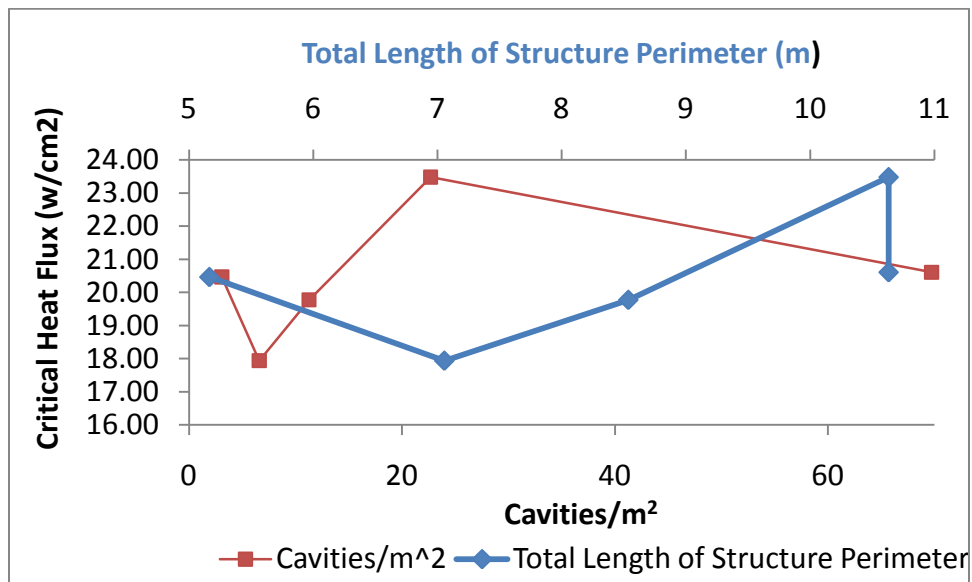


Figure 4-10. Critical heat flux variation as a function of cap size. No trend is apparent.

It is believed that enhanced wicking and three-phase contact line explain the increase in critical heat flux for the smaller spacing. This is supported by the observation of what looked like small vortices formed across the surface near the critical heat flux as shown in Figure 4-12. Due to the difficulty in imaging this phenomenon, the camera shutter was left open for ~ 5 seconds. The resulting images are based on an average over this time and only show the elements on the surface that are static. This is

consistent with the reports by Ramaswamy [68] and Das [14] in regard to enhanced liquid entrainment in pore and tunnel networks, although no mention of these types of vortices has ever been made.

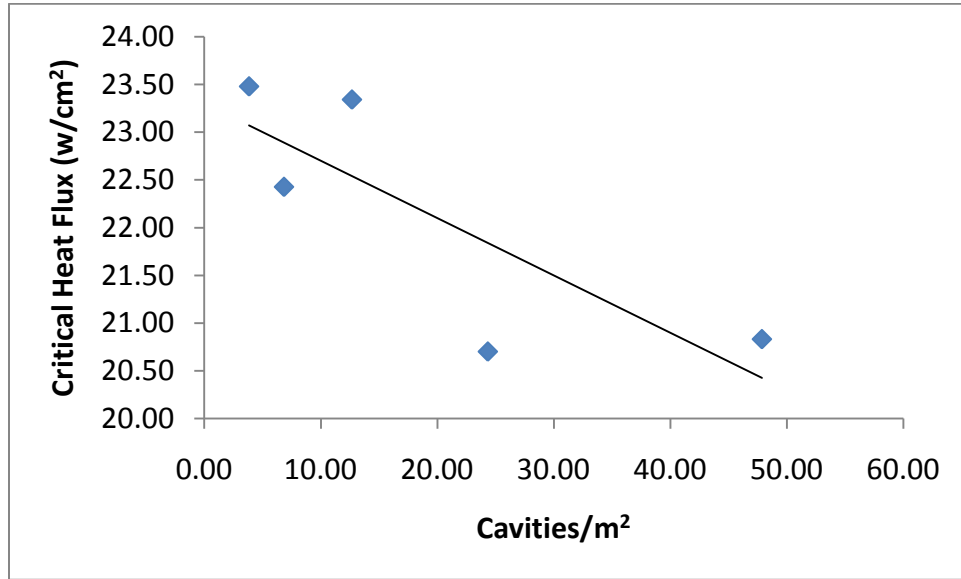


Figure 4-11. Improvement in CHF as a function of spacing for the 20 μ m cap size. CHF is slightly increased for the smaller spacing on the 20 μ m caps.

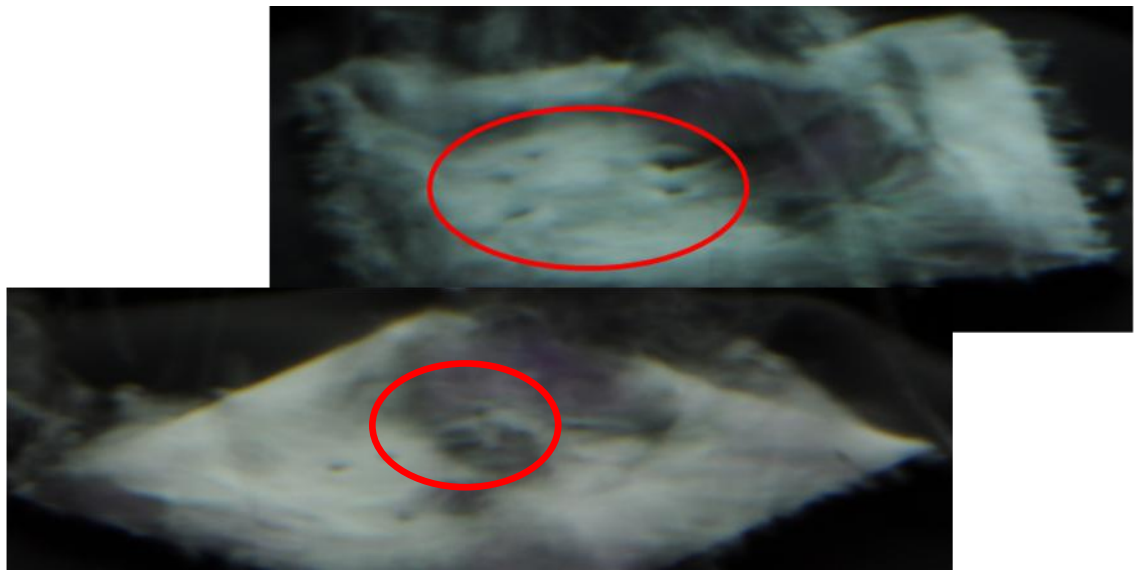


Figure 4-12. Images taken with long shutter lengths, of boiling near the critical heat flux. The black spots were liquid vortices pulling fluid toward the surface.

Copper Coating

Figure 4-13 shows the variation in pool boiling performance for the 20 μm cap size spaced by 3 μm with and without a copper coating. Copper is known to be a good boiling surface. One of the reasons is that it has a good thermal conductivity allowing for rapid reheating of cold spots left behind when bubbles depart. This allows for more rapid vaporization of the next bubble at an active site. The copper coating has a positive effect on performance in terms of both the onset of nucleate boiling and the heat transfer coefficient as expected, although there is a slight decrease in CHF.

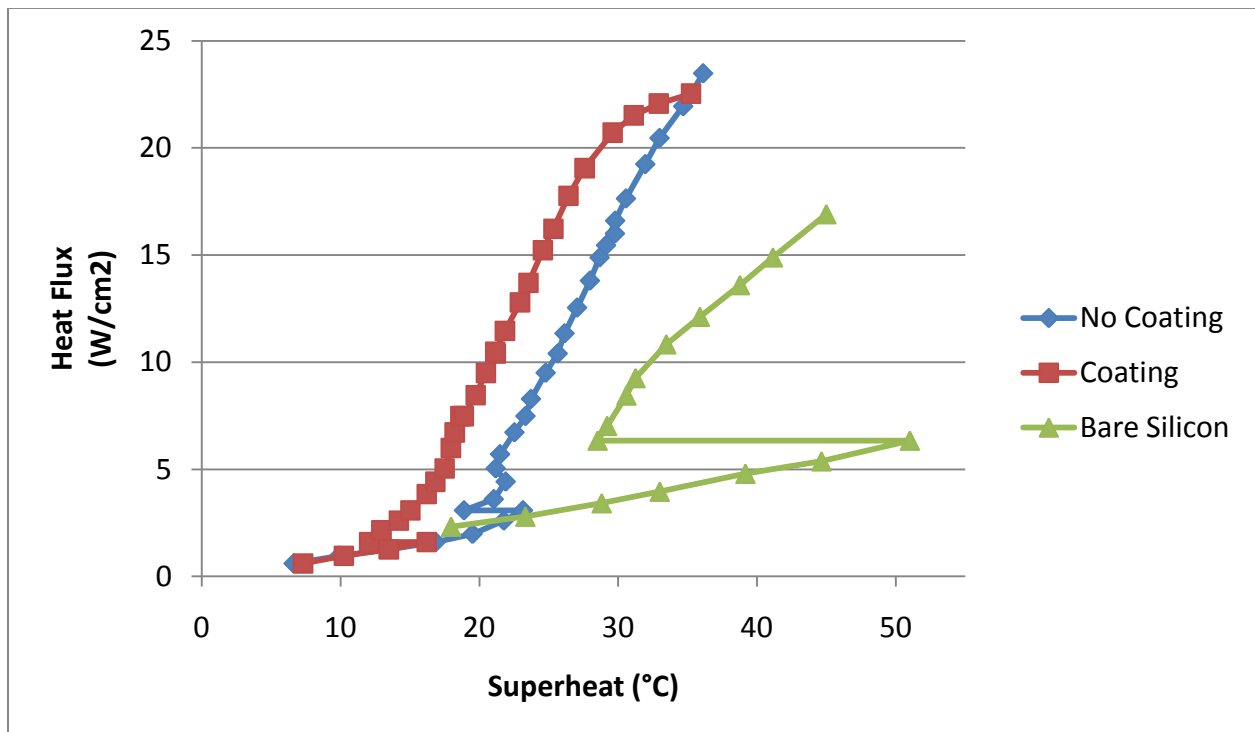


Figure 4-13. Boiling curves for the 20 μm cap size spaced by 3 μm with and without a copper coating. Sputter coating a 200nm thick layer of copper increases the thermal conductivity of the surface, resulting in increased HTC and a slight decrease of ~4% in CHF.

Etching Variations

Figure 4-14 shows the results of varying the etching conditions. Details for the dimensions of the various etch conditions can be found in Chapter 2. Altering the height

and undercut of structures appears to have almost no effect on the boiling curves. The only exception to this is the slight increases in HTC and CHF for the thicker capped structures. This is likely due to a reduction in the slight chipping of the caps during boiling. All surfaces used in the boiling experiments used the thicker caps for this reason except the copper-coated sample. This may also explain why the copper-coated sample showed a drop off in performance near CHF. It is also notable that the surface with no undercut shows a small but standard temperature overshoot before the onset of nucleate boiling. This is expected and one of the reasons reentrant structures were used in this work.

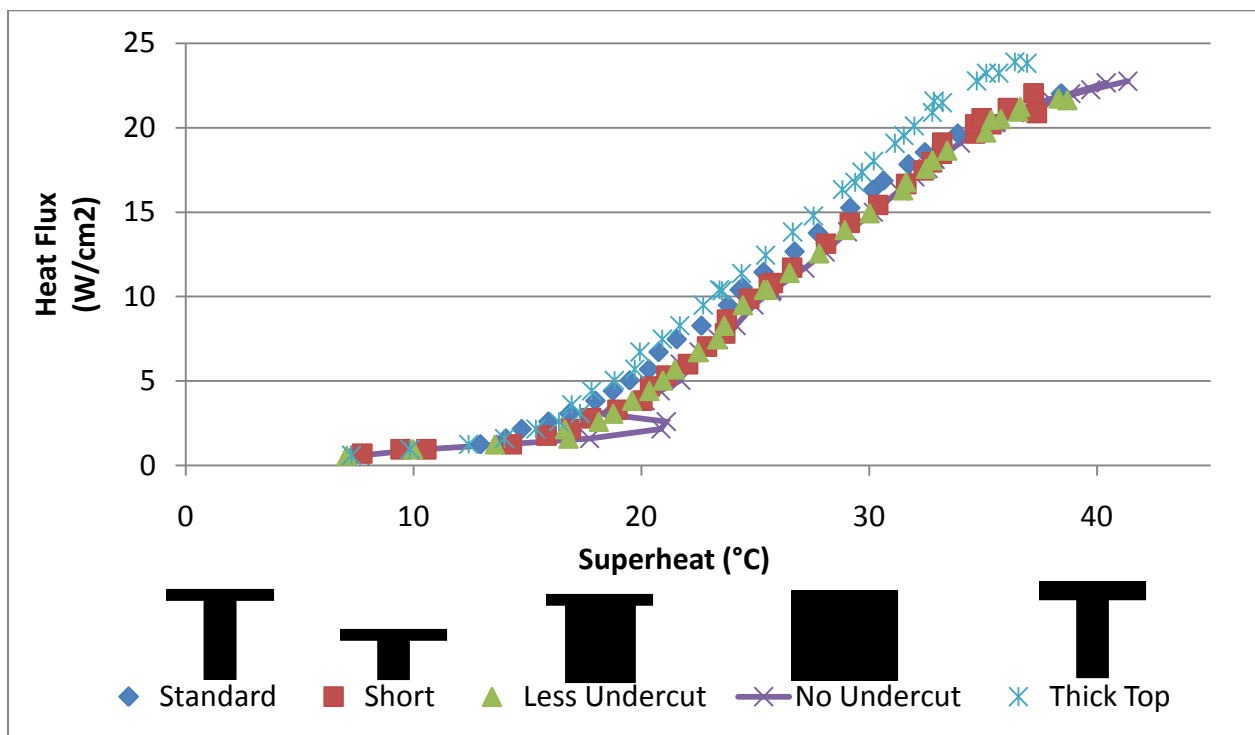


Figure 4-14. Boiling curves for the etching variations. Removing the undercut does increase the incipience temperature as expected. The variations in profile where expected to affect flow dynamics and alter the length of the three-phase line, however, there are no significant changes in the boiling curves.

Boiling Conclusion

The pool boiling performance of discrete reentrant surface structures on the micron scale has been investigated. It was found that these surfaces had a significant effect on both heat transfer coefficient in the nucleate boiling regime and on critical heat flux, although not as much as has been shown on previous optimized micro pin-fin surfaces. An optimum in cap size, which corresponds to the pore density on the surface, has been found. Additionally it has been shown that smaller spacing and rough thermally conductive coatings can also have a significant impact on pool boiling performance. These surfaces could be processed directly on the backside of semiconductor chips leading to solutions for the increasing heat loads produced by denser chips. This boiling data is also being used to model aspects of pool boiling (that have been difficult to model with less well-defined surfaces) by mechanical engineering PhD. students in Dr. James Klausner's lab.

CHAPTER 5 CONCLUSION AND FUTURE WORK

Successful methods have been devised and employed to create undercut micro scale surface patterns. The wetting work described in Chapter 3 has demonstrated that a simple model based on numerical simulation of the wetted fraction of the triple point line has a significantly better relationship to the measured data than any model to date. This is significant due to the increasing demand for superhydrophobic surfaces. This model can be turned in to a small freely distributed software package that accepts rendered images of surfaces and calculates expected contact angles as a function of droplet radius.

Furthermore, qualitative data is presented to help elucidate the properties that most significantly affect the pressure threshold for submerged superhydrophobic surface. This data indicated that taller structures and the presence of an undercut have significant impacts on the ability of a surface to maintain a non-wetted state while being submerged under water.

Chapter 4 investigated the performance of these surfaces for pool boiling. It was found that these surfaces had a significant effect on both heat transfer coefficient in the nucleate boiling regime and on critical heat flux. An interesting type of vortex providing liquid to the surface at high heat fluxes that has never been seen was also discussed. Future work should test boiling on surfaces with different surface tensions. This may further elucidate the mechanisms responsible for enhanced boiling on discrete reentrant surfaces. This may lead to the development of boiling surfaces processed on the backside of semiconductor chips. This could lead to solutions for the increasing heat loads produced by denser chips.

APPENDIX A FABRICATION STEPS

- Deposit a thin layer (300-500nm) of SiO₂ using an STS 310PC PECVD
- Spin coat with 2µm of S1813 positive photo resist
- Soft bake the resist at 105°C for 2 minutes
- Expose mask to G-line(436nm) UV for 21 seconds on a Karl Suss MA6 mask aligner
- Reverse pattern using a Yes image reversal oven
- Expose mask to G-line(436nm) UV for 52.5 seconds
- Develop the resist in 300MIF for 1 minute
- Hard bake the resist at 125°C for 3 minutes
- Etch through SiO₂ using a Unaxis Shuttlelock reactive ion etcher.
 - Gas flow is 25sccm CHF₃ and 3sccm O₂
 - Plasma power is 100W capacitively coupled and 600W inductively coupled
 - Pressure is 5 millitorr
 - Etch time is 2 minutes.
- Etch anisotropically down using the STS deep reactive ion etcher
 - Etch cycle is 7 seconds of SF₆/O₂ followed by 5 seconds of C₄F₈
- Remove any remaining passivation with 30 second O₂ plasma ash
- Etch isotropically (under SiO₂ caps) using the STS deep reactive ion etcher
 - Each cycle is 7 seconds of SF₆ followed by 14 seconds of no power to allow the product species to dissipate and reduce the variation in etch rate for each pattern.
- Immerse the wafer in PRS 3000 stripper with a bath temperature of 80°C for 30 minutes to remove the photo-resist
- Remove any remaining resist in a barrel asher
 - 600 watts power

- 600sccm O₂ flow rate
- 10 minutes
- Deposit a layer of C₄F₈ passivation for 20 seconds in the deep reactive ion etcher
 - Gas flow is 85sccm
 - Plasma power is 600

Table 2-1. Variations in dry etching conditions. Each variation of the structure profile can be achieved by applying the number of cycles in this table to the fabrication steps above.

	Anisotropic Etch (cycles)	Oxygen Clean (seconds)	Isotropic Etch (cycles)
Normal	20	30	12
Tall	40	30	12
Short	10	30	12
More Undercut	20	30	24
Less Undercut	20	30	6
No Undercut	20	30	0

APPENDIX B
SCANNING ELECTRON MICROSCOPY

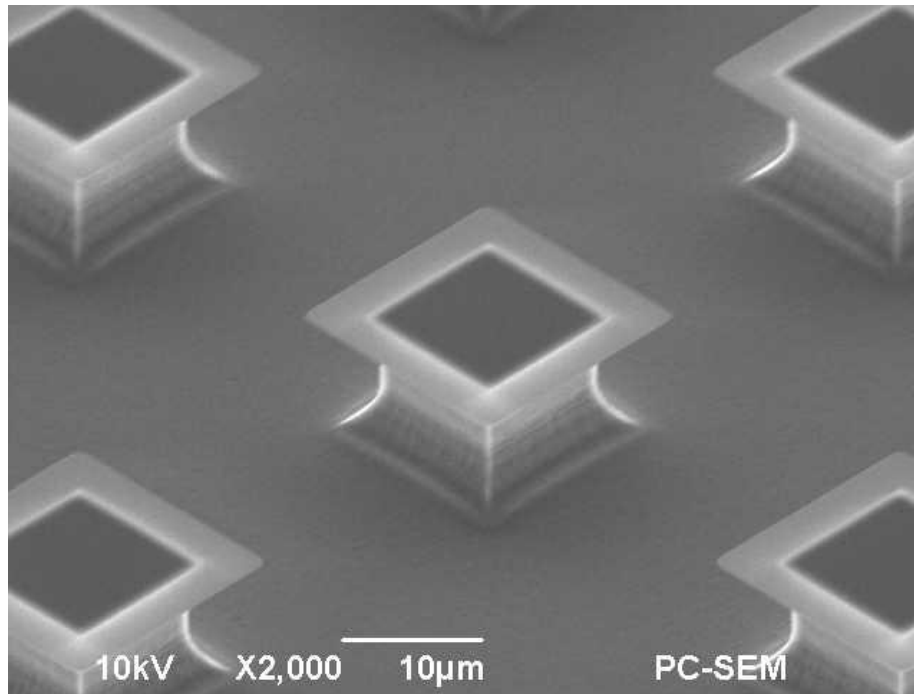


Figure A-1. Standard 20x20μm square pattern. The optimized etching produces smooth, near vertical side walls.

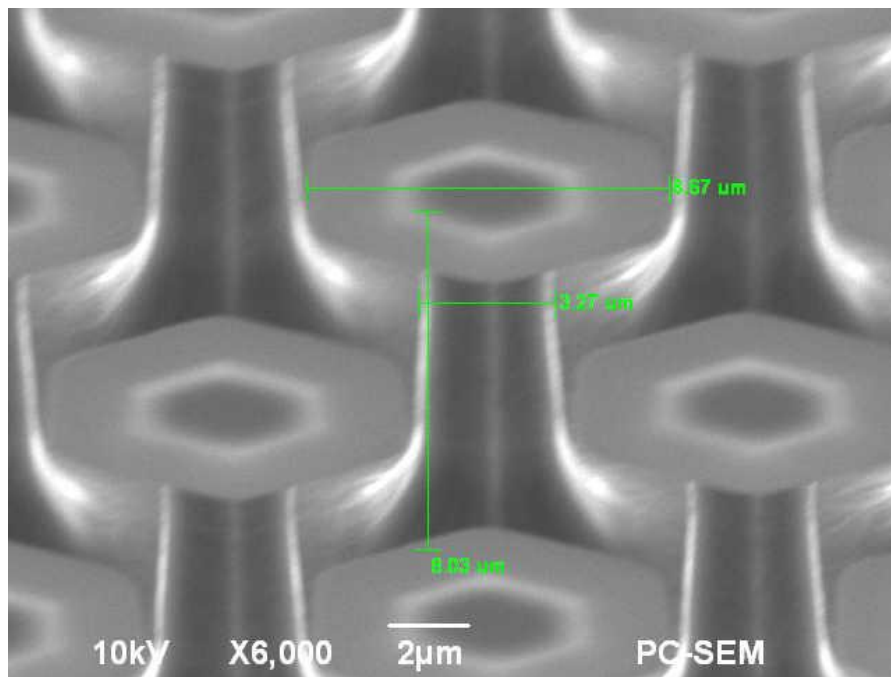


Figure A-2. Standard 10μm cap size with 3μm spacing in tilted view. Stems of structures display smooth, nearly vertical side walls.

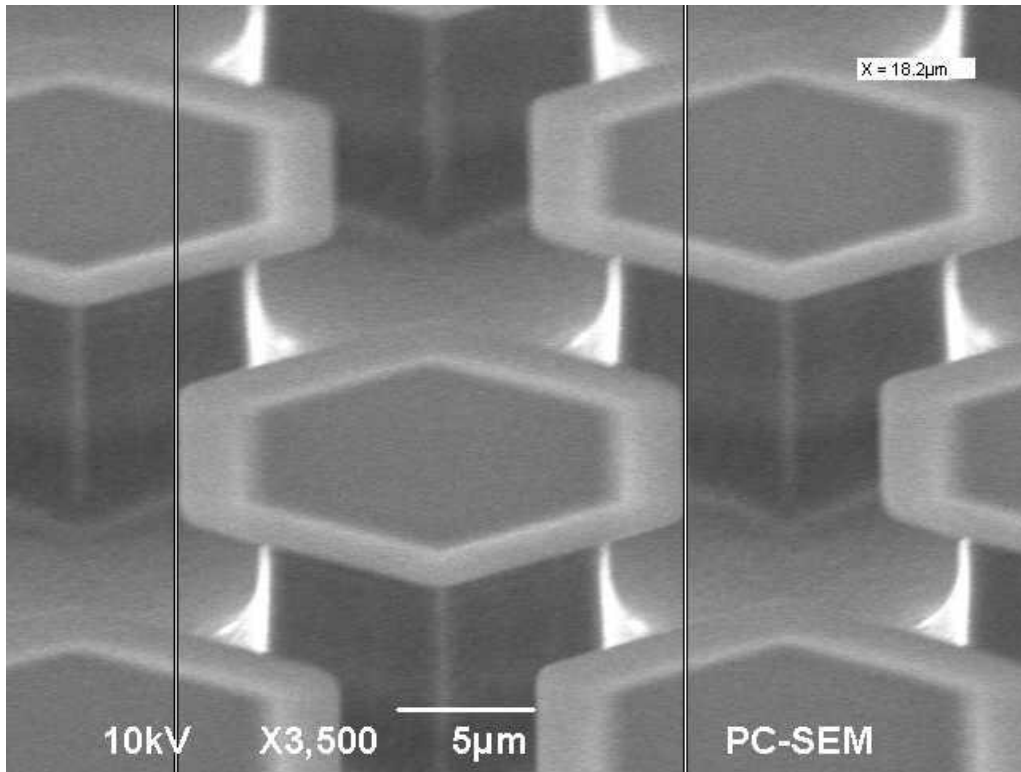


Figure A-3. Standard 20µm cap size with 3µm spacing

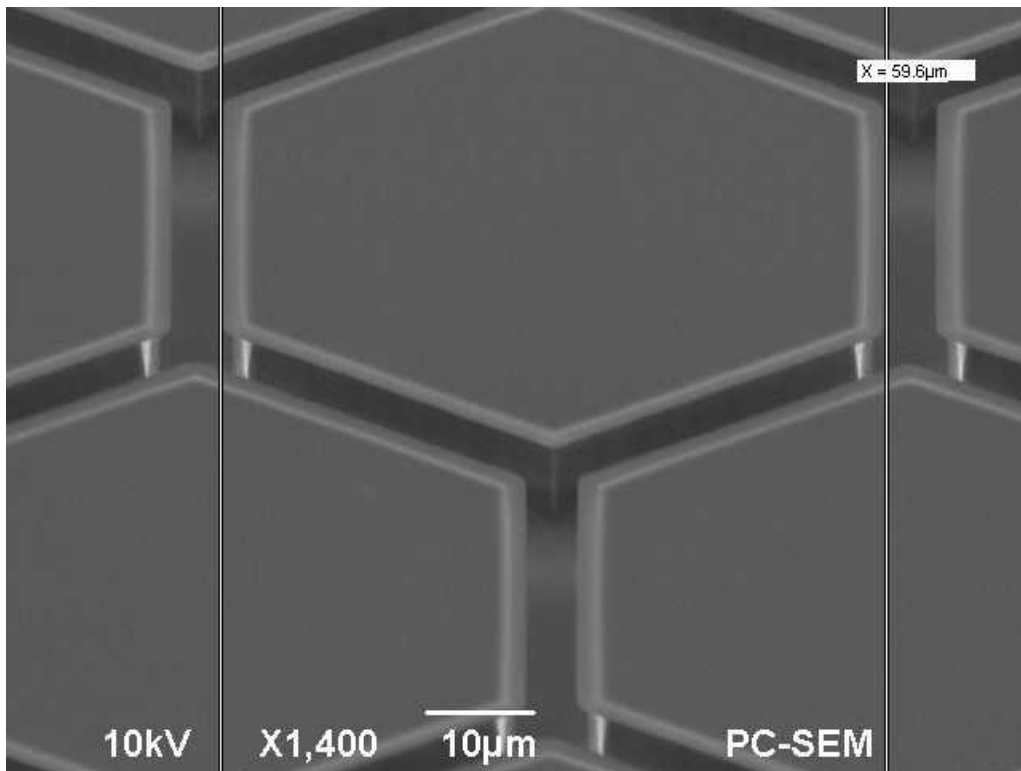


Figure A-4. Standard 60µm cap size with 3µm spacing

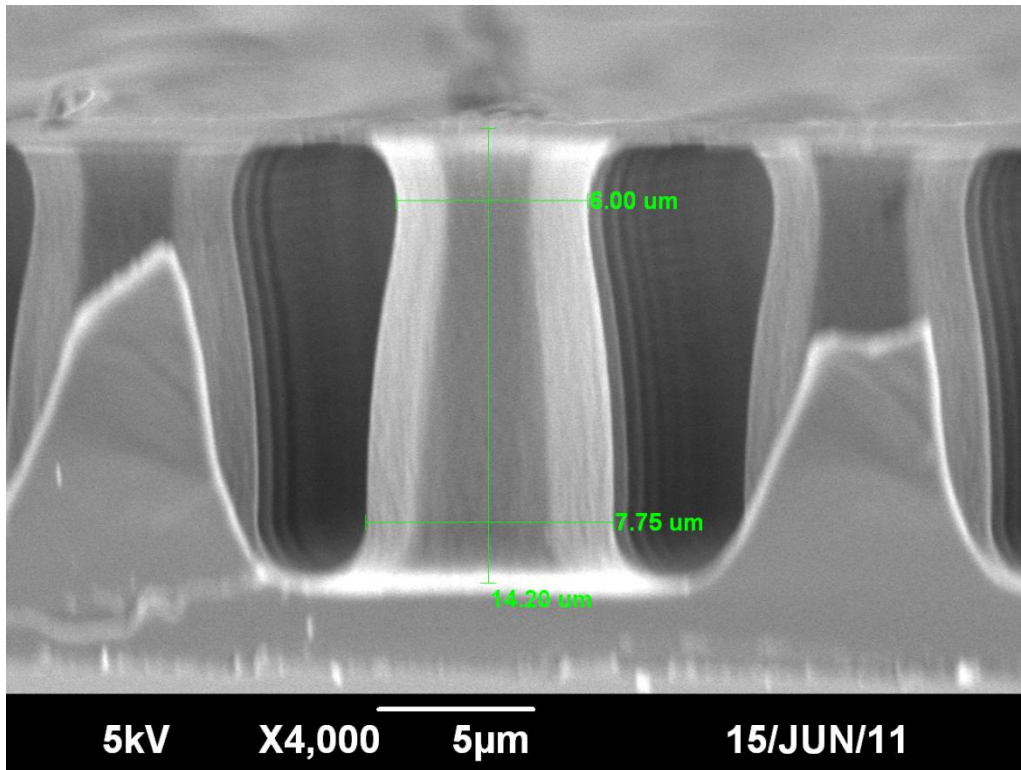


Figure A-5. Tall 10µm cap size with 3µm spacing, cross section

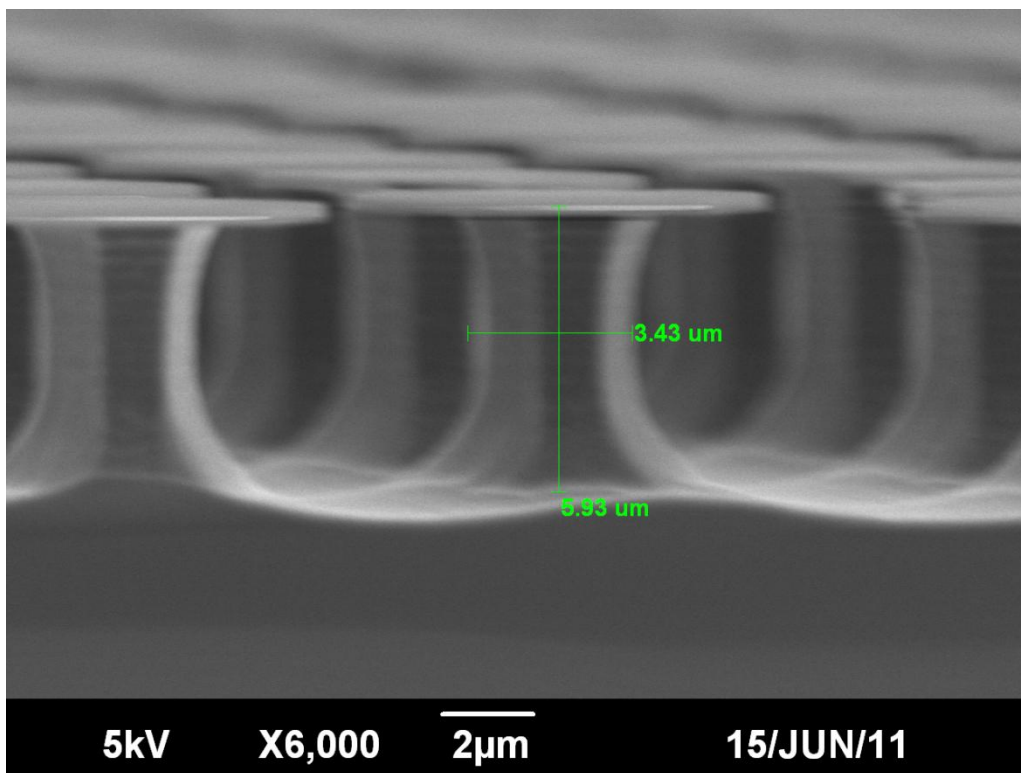


Figure A-6. Short 10µm cap size with 3µm spacing, cross section

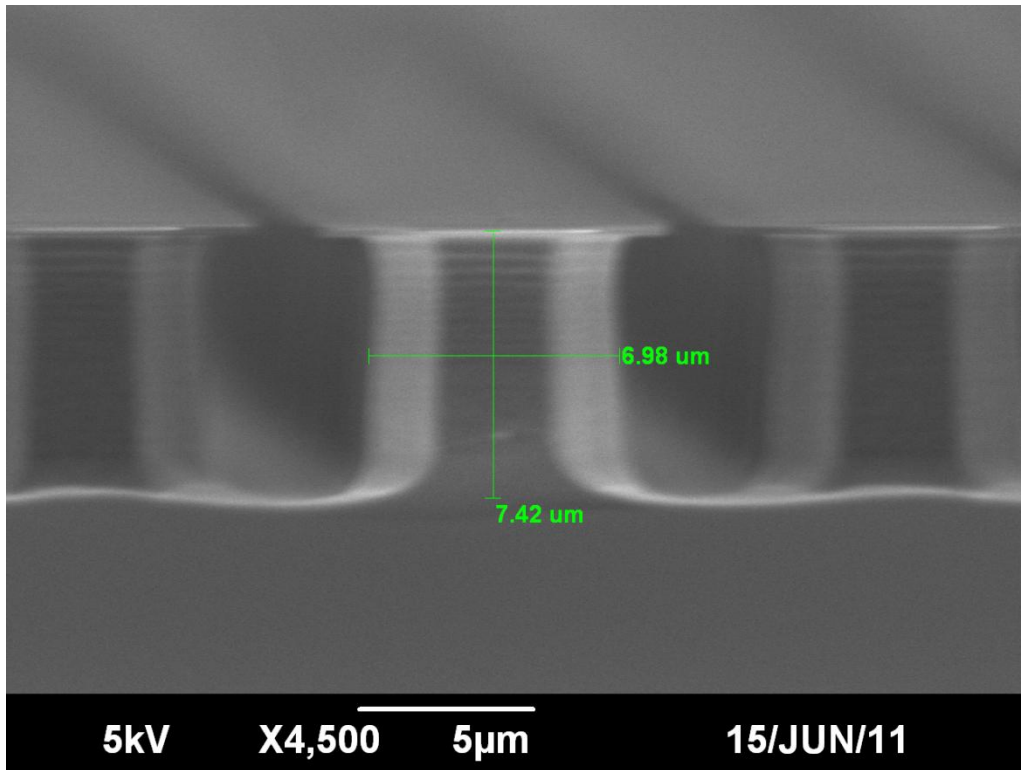


Figure A-7. Less undercut 10µm cap size with 3µm spacing, cross section

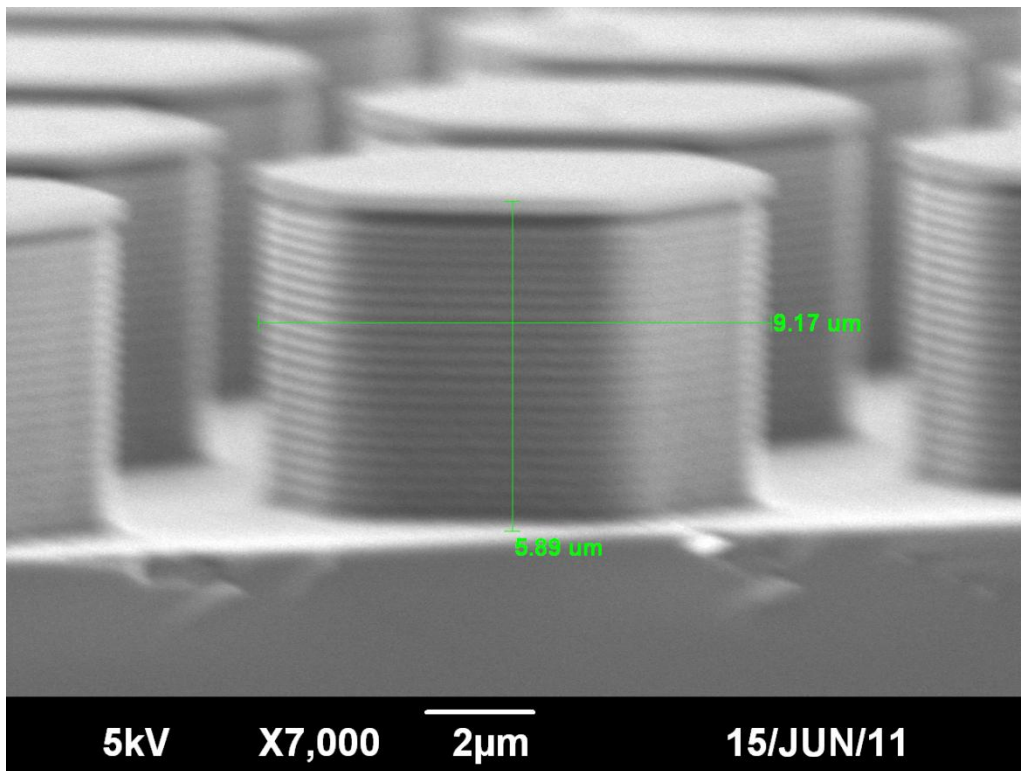


Figure A-8. No undercut 10µm cap size with 3µm spacing, cross section

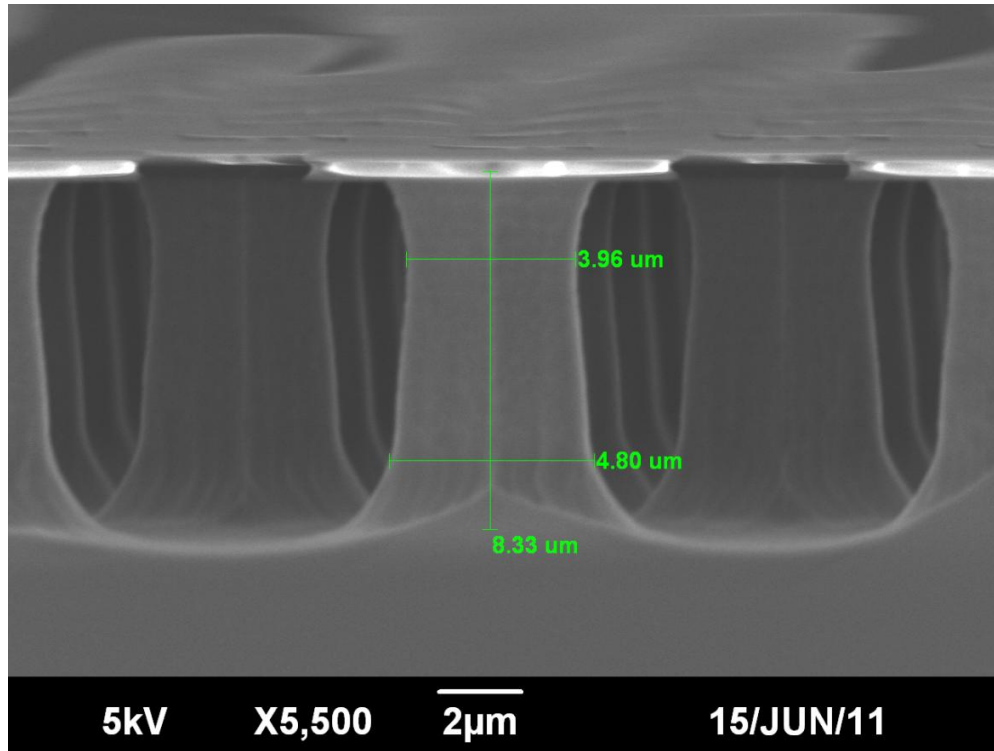


Figure A-9. Standard 10µm cap size with 3µm spacing, cross section with 500nm thick caps

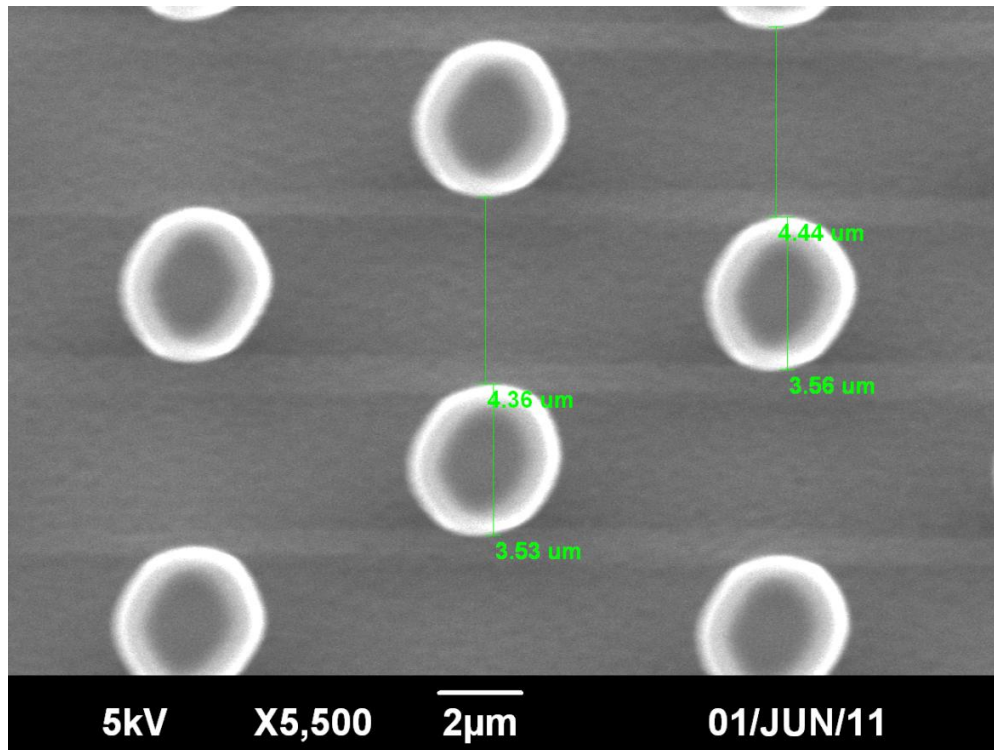


Figure A-10. 5µm cap size with 3µm spacing, plan view

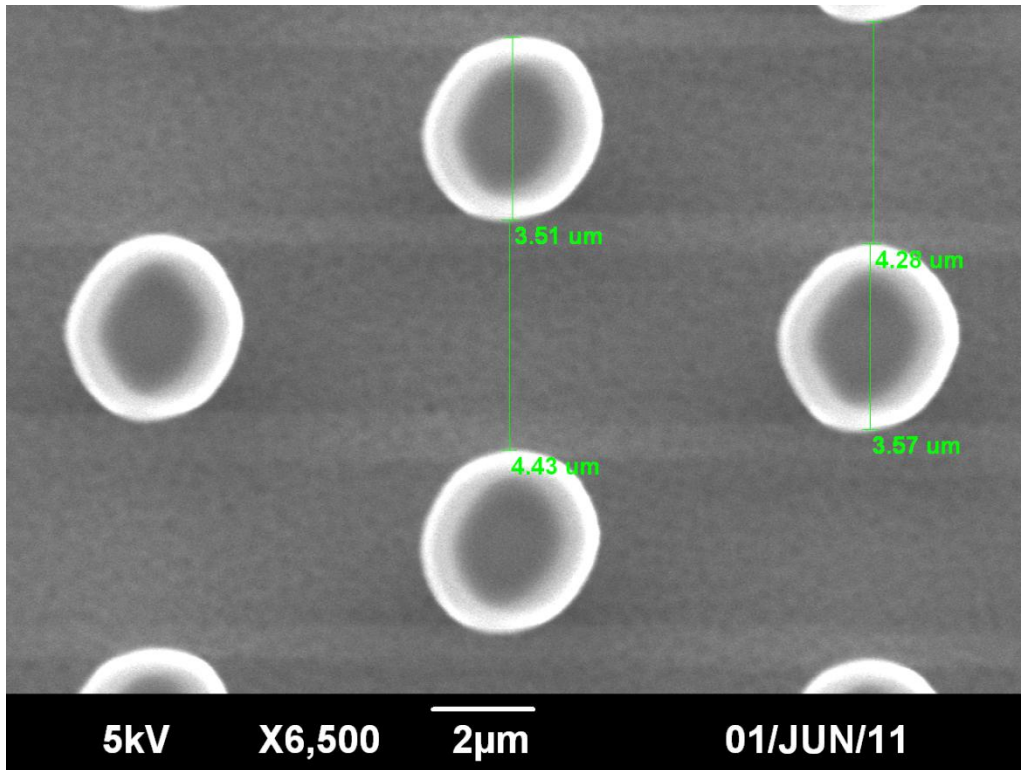


Figure A-11. 5μm cap size with 3μm spacing, plan view (2)

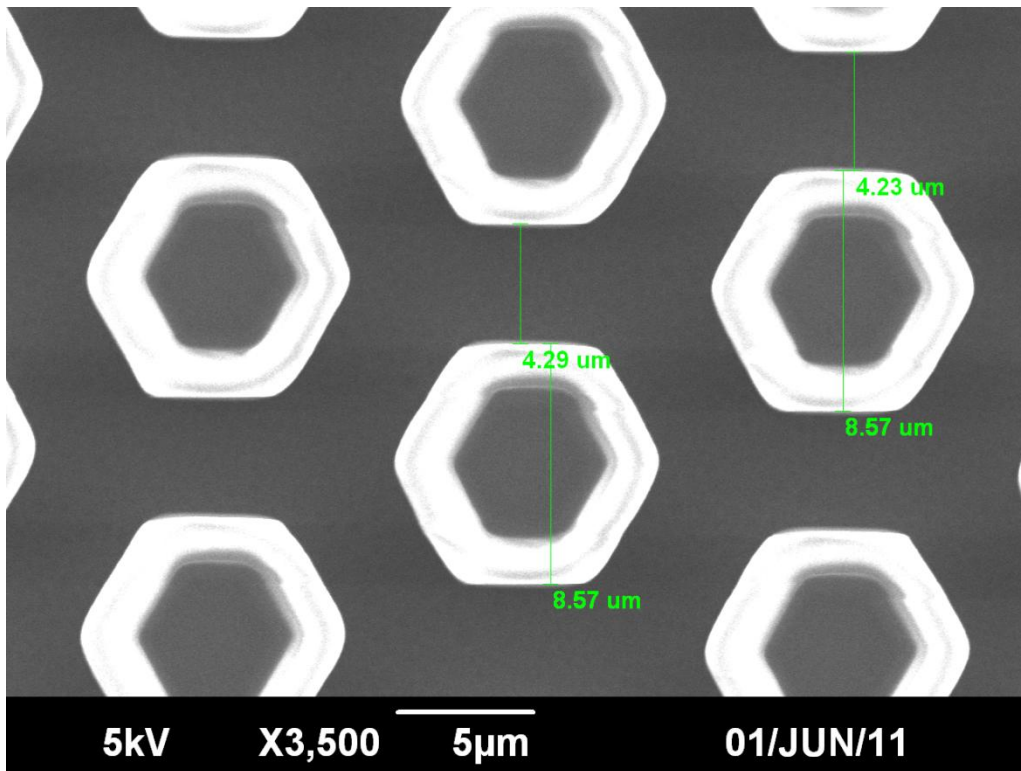


Figure A-12. 10μm cap size with 3μm spacing, plan view (short)

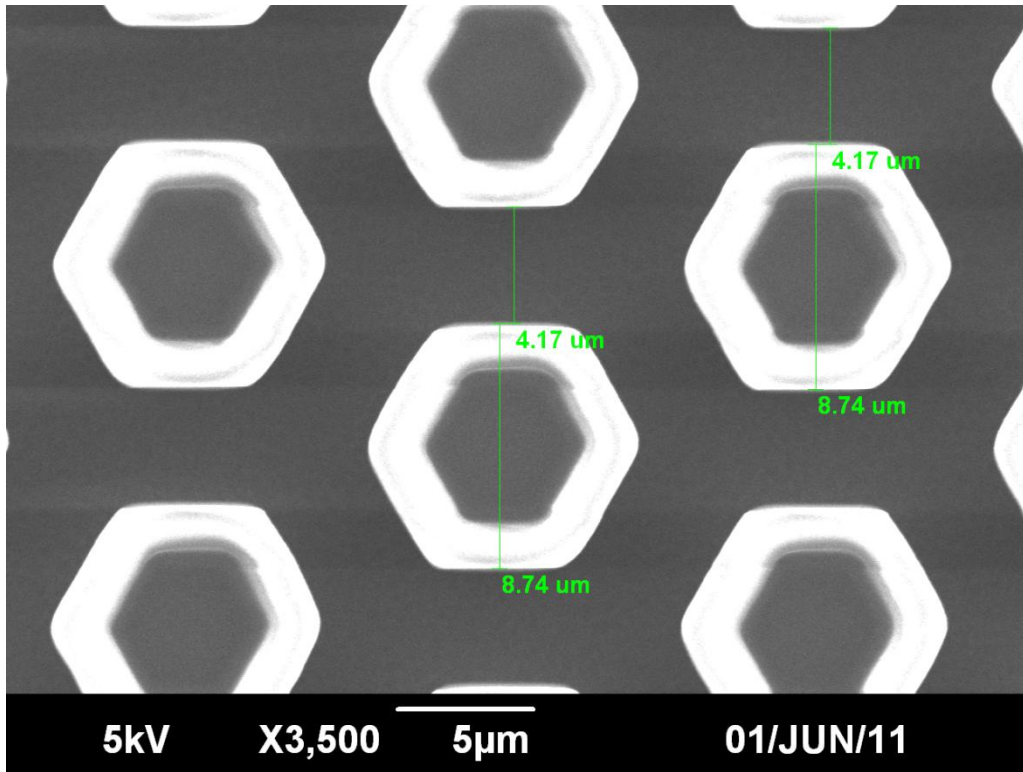


Figure A-13. 10 μm cap size with 3 μm spacing, plan view (2) (short)

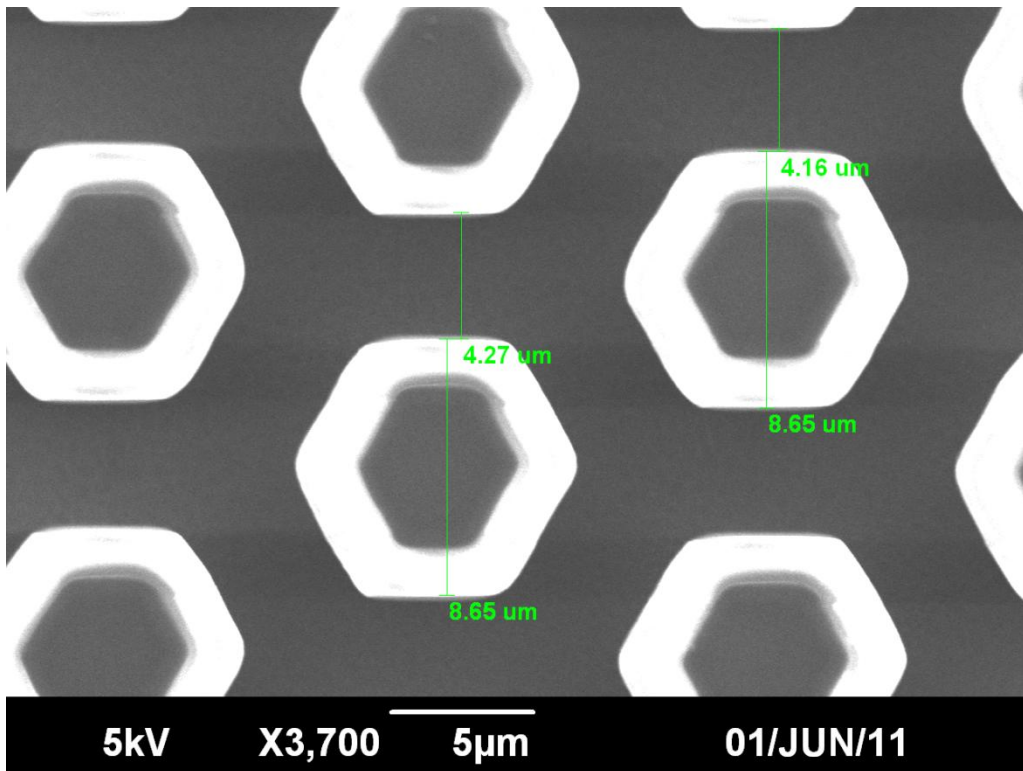


Figure A-14. 10 μm cap size with 3 μm spacing, plan view (3) (short)

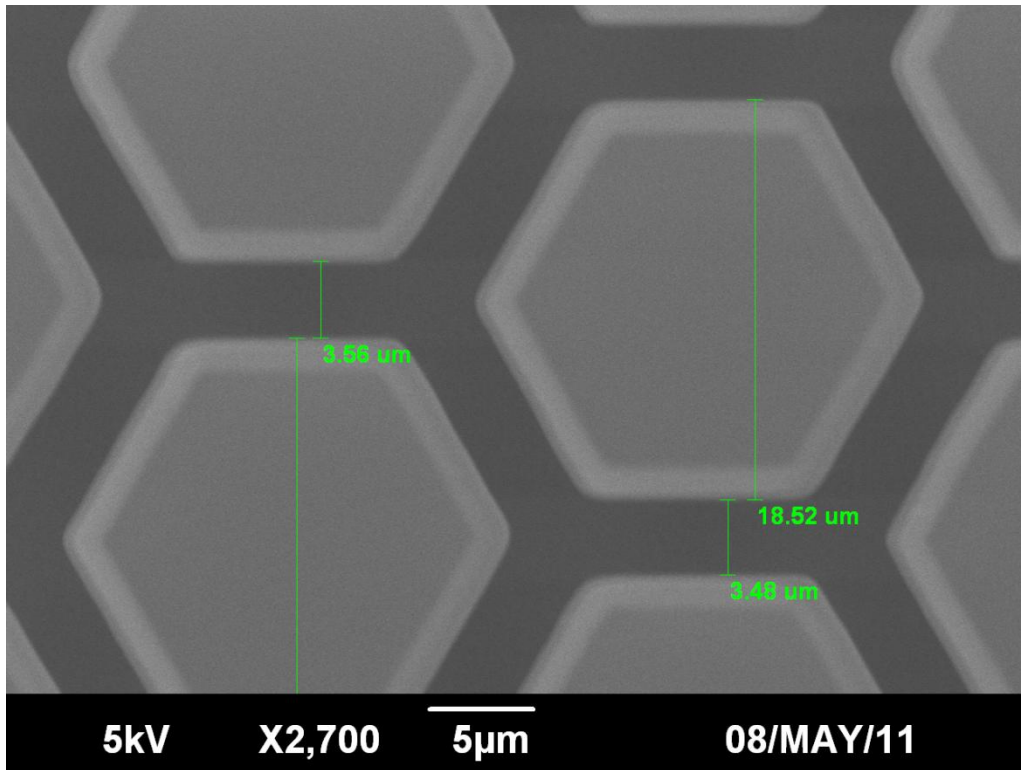


Figure A-15. 20μm cap size with 3μm spacing, plan view (standard)

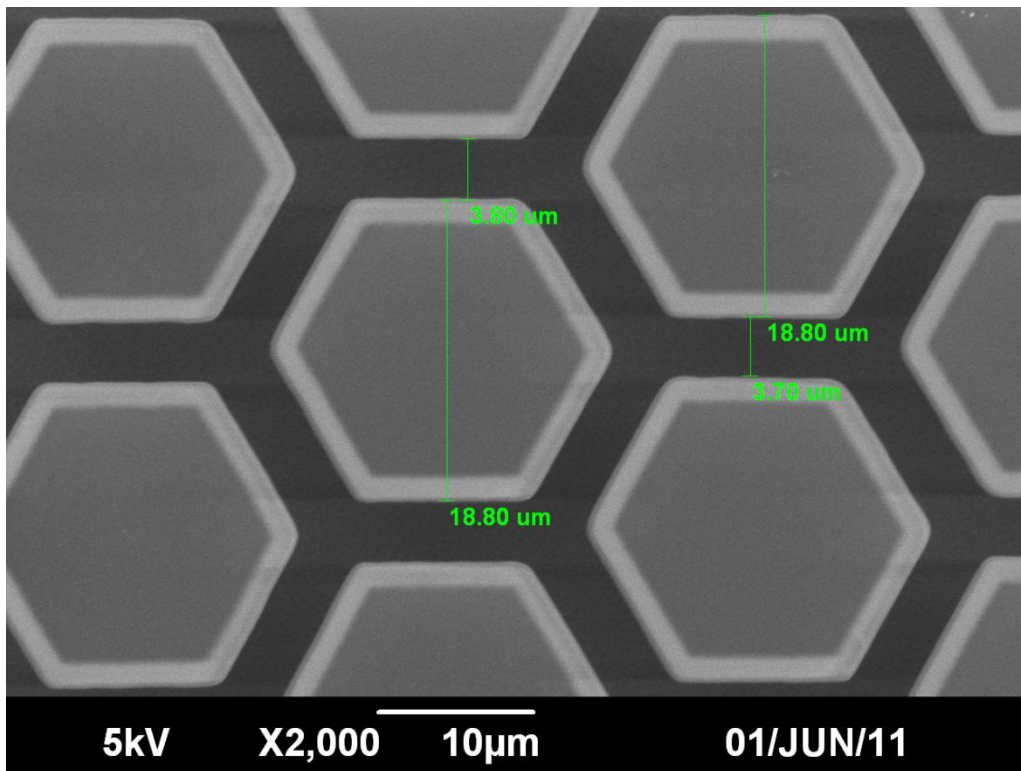


Figure A-16. 20μm cap size with 3μm spacing, plan view (2) (standard)

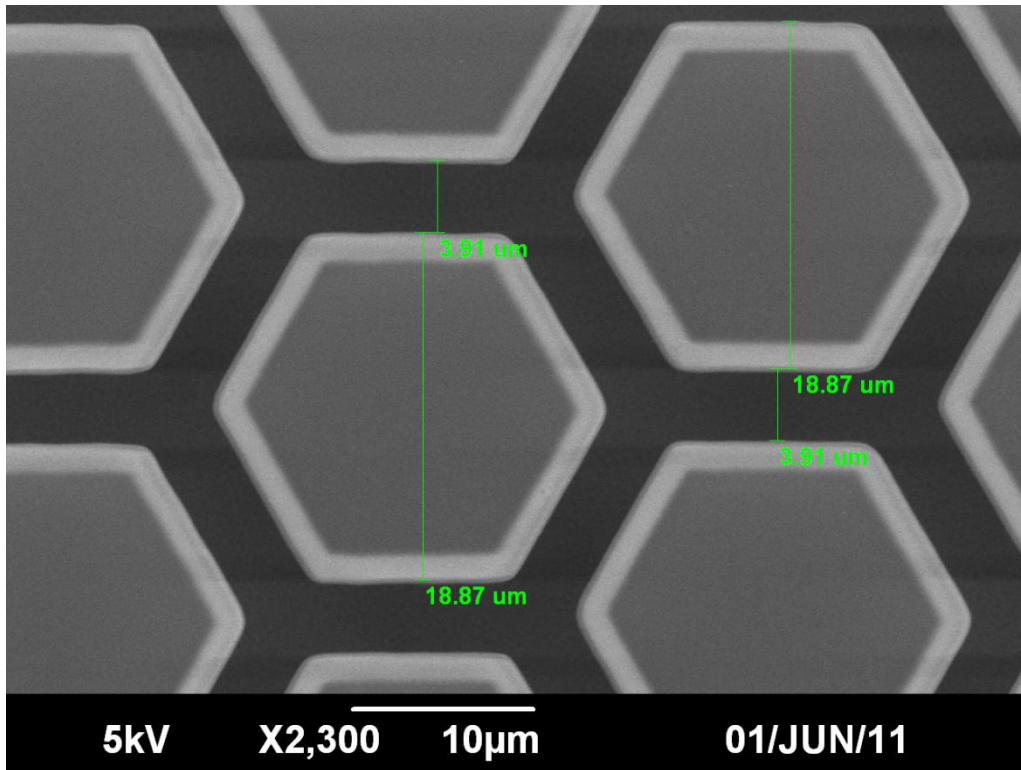


Figure A-17. 20µm cap size with 3µm spacing, plan view (3) (standard)

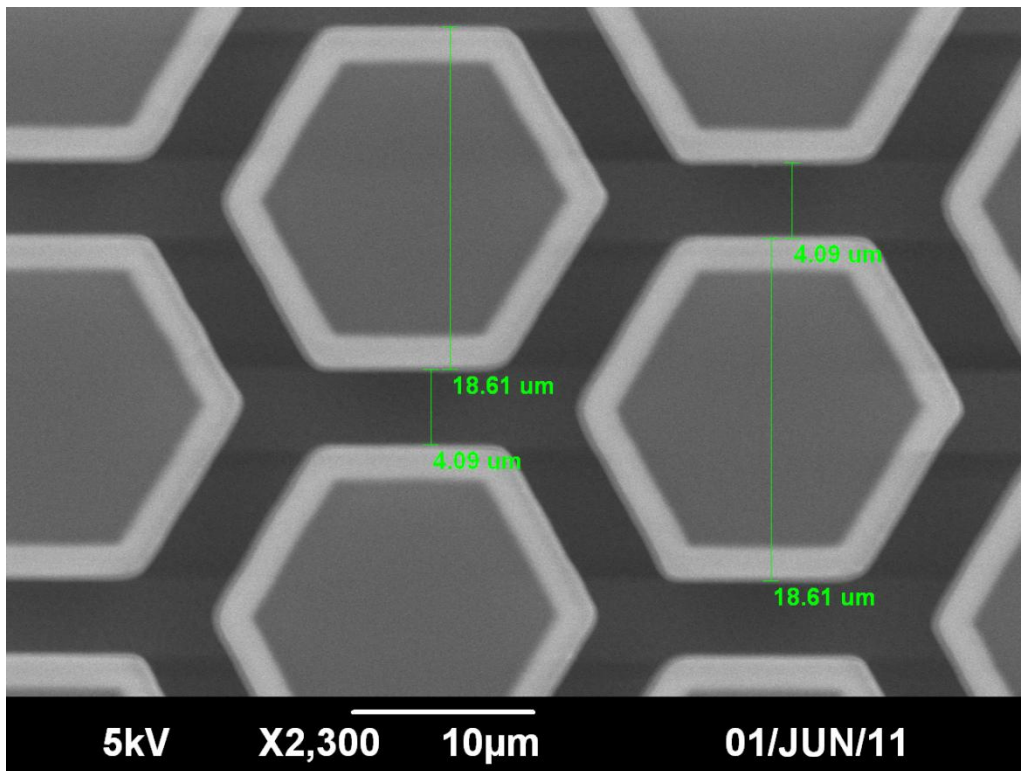


Figure A-18. 20µm cap size with 3µm spacing, plan view (4) (short)

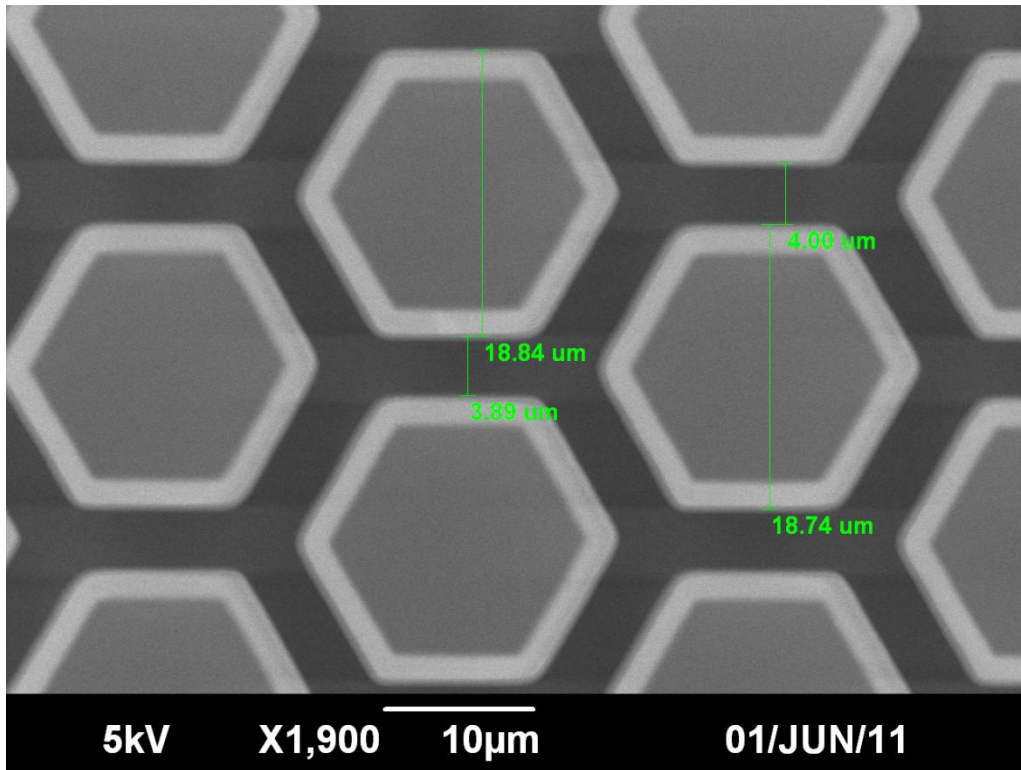


Figure A-19. 20µm cap size with 3µm spacing, plan view (5) (short)

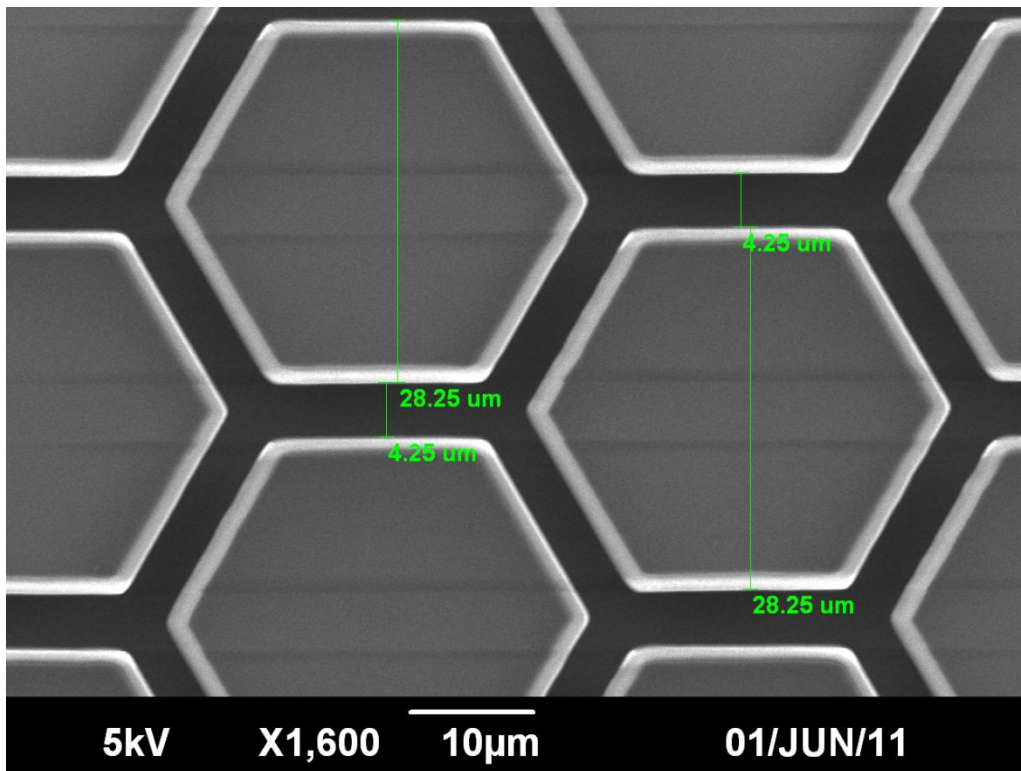


Figure A-20. 30µm cap size with 3µm spacing, plan view (standard)

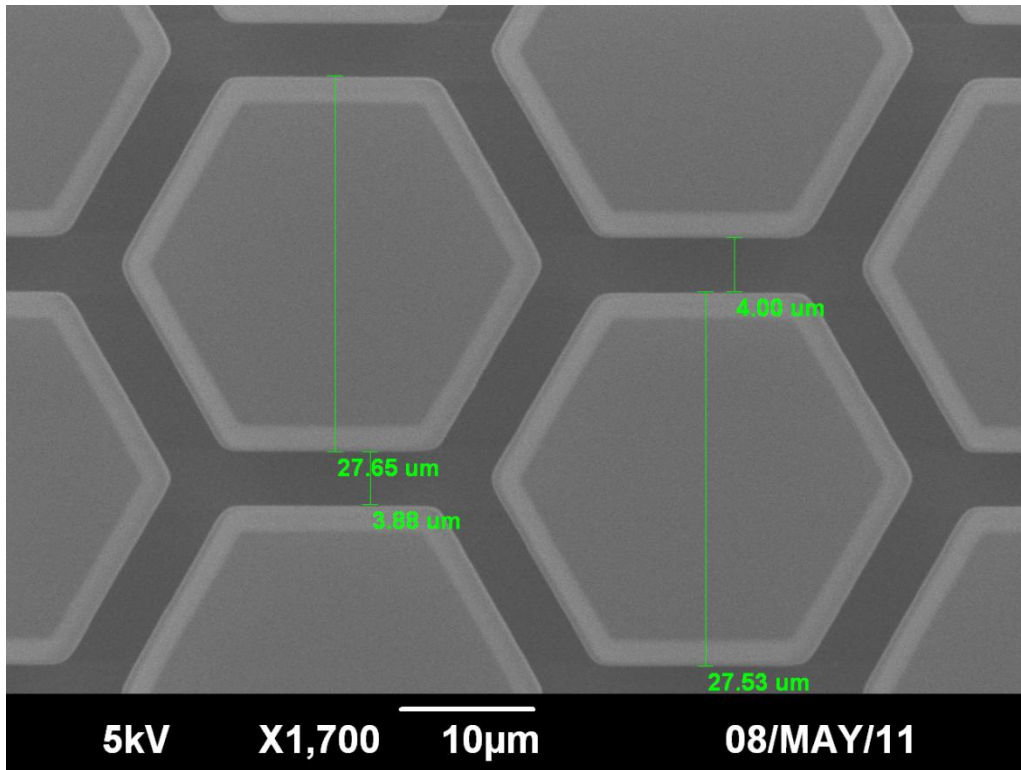


Figure A-21. 30µm cap size with 3µm spacing, plan view (2) (short)

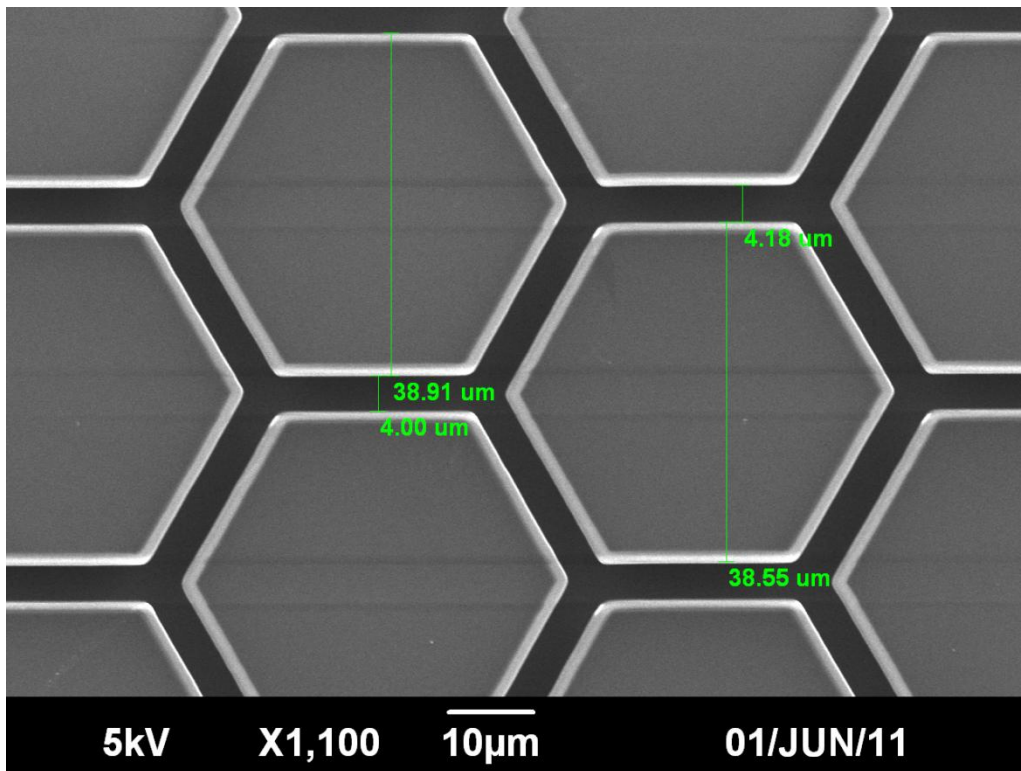


Figure A-22. 40µm cap size with 3µm spacing, plan view (standard)

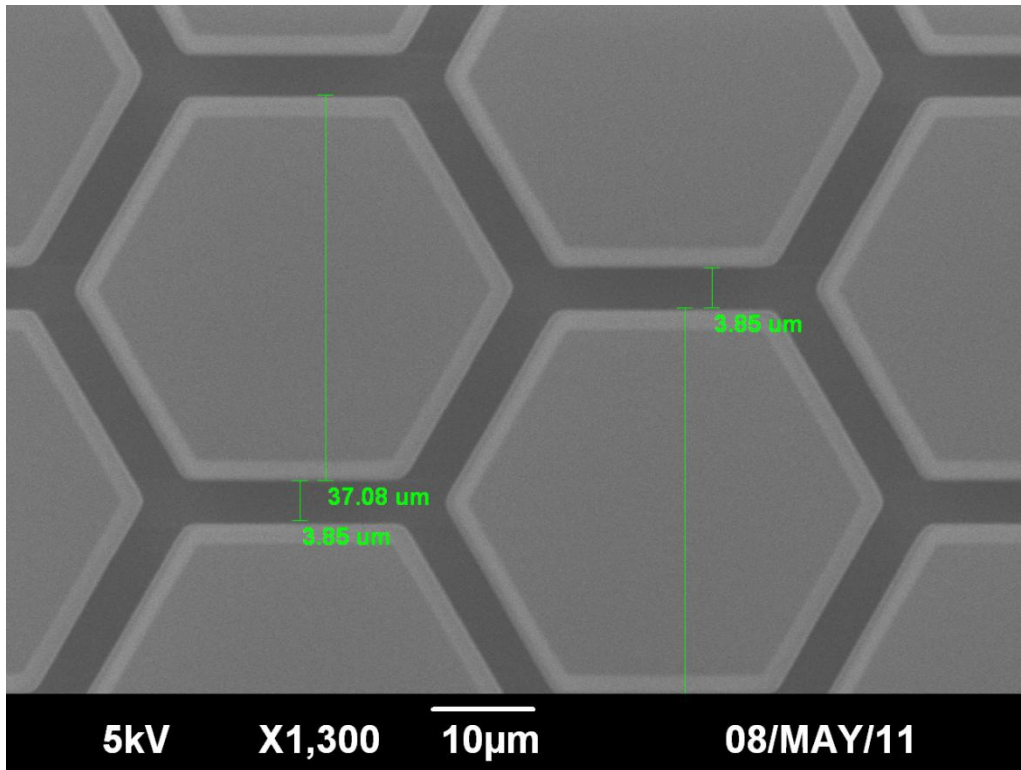


Figure A-23. 40µm cap size with 3µm spacing, plan view (2) (short)

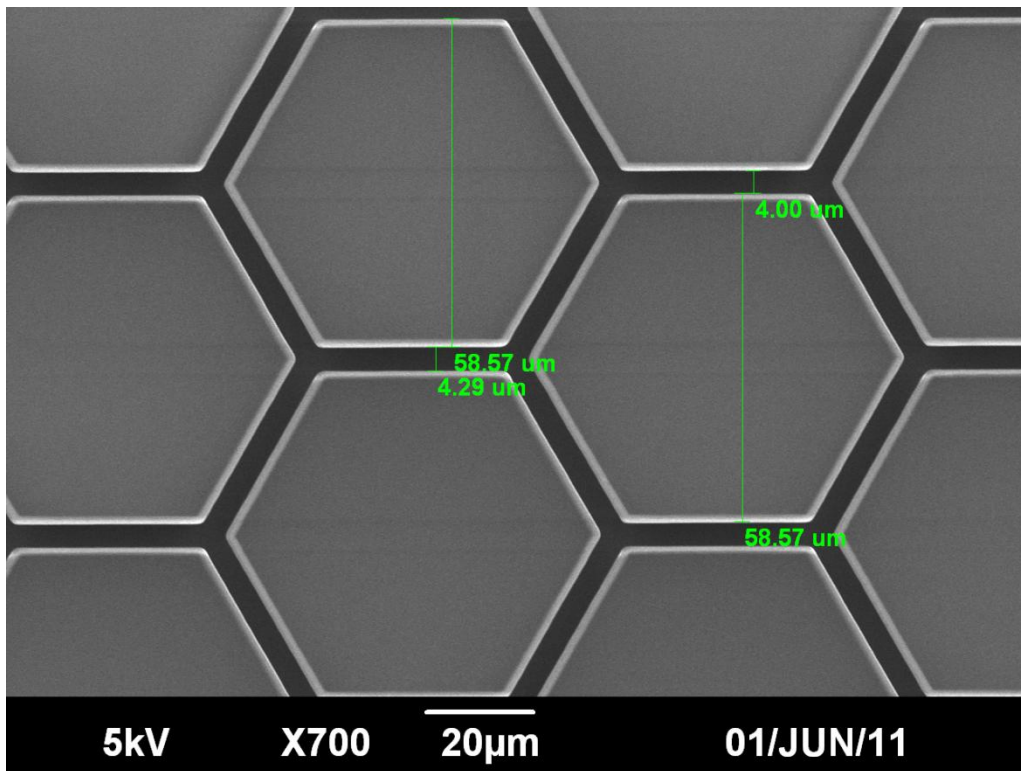


Figure A-24. 60µm cap size with 3µm spacing, plan view (standard)

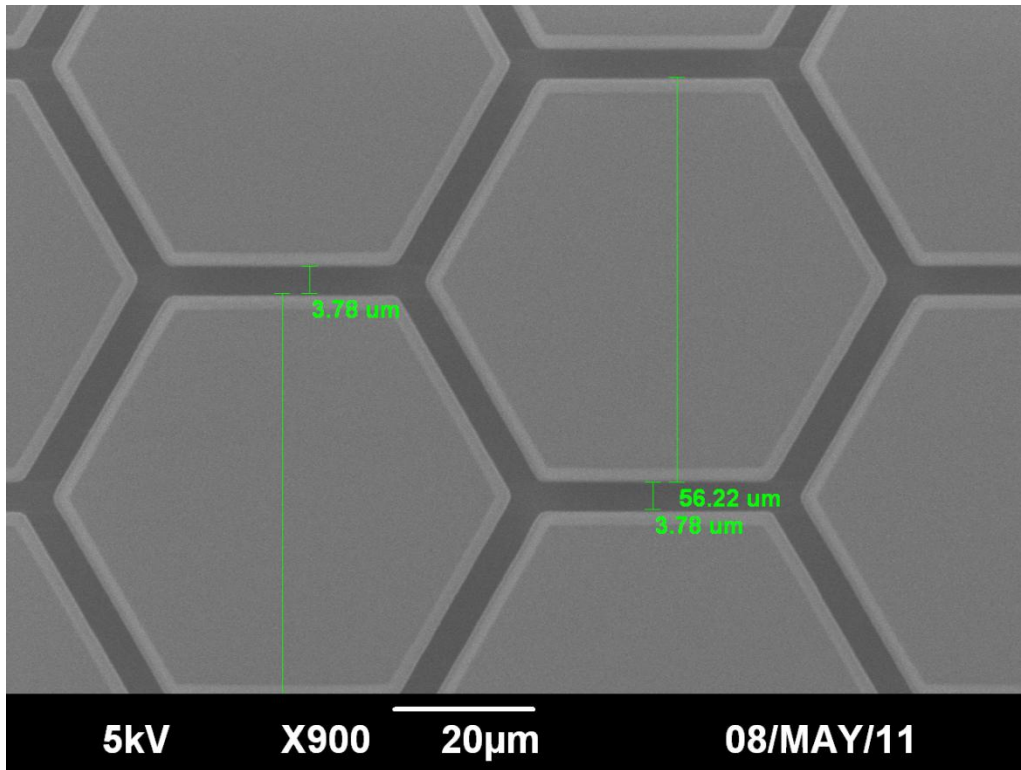


Figure A-25. 60µm cap size with 3µm spacing, plan view (2) (short)

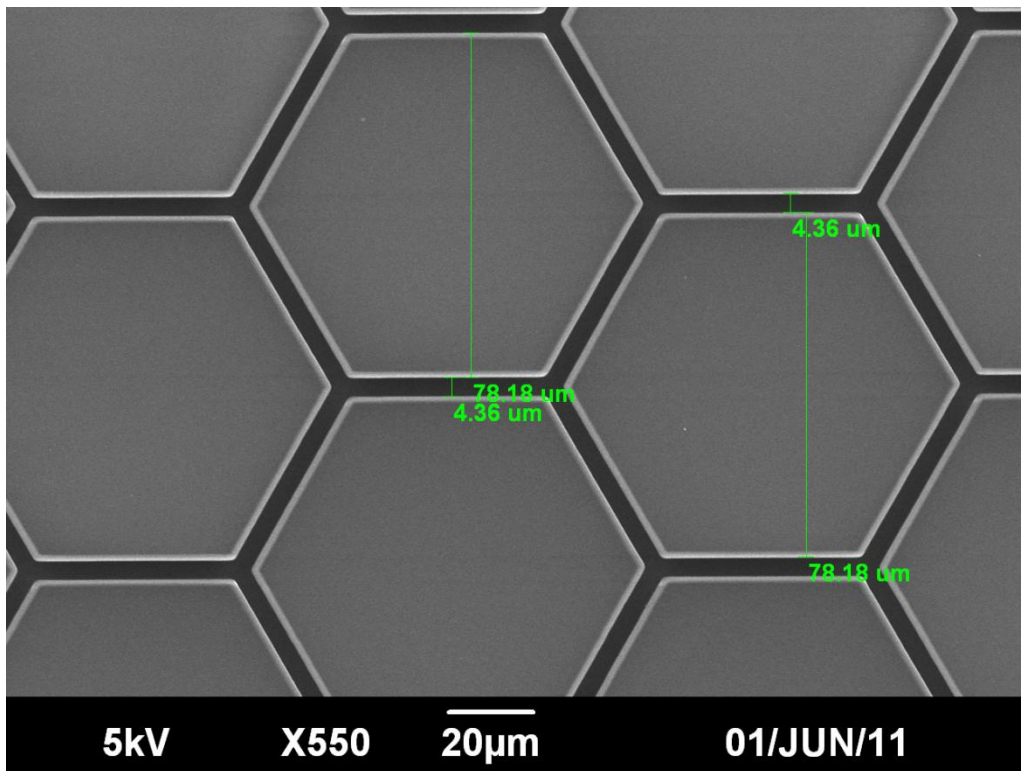


Figure A-26. 80µm cap size with 3µm spacing, plan view (standard)

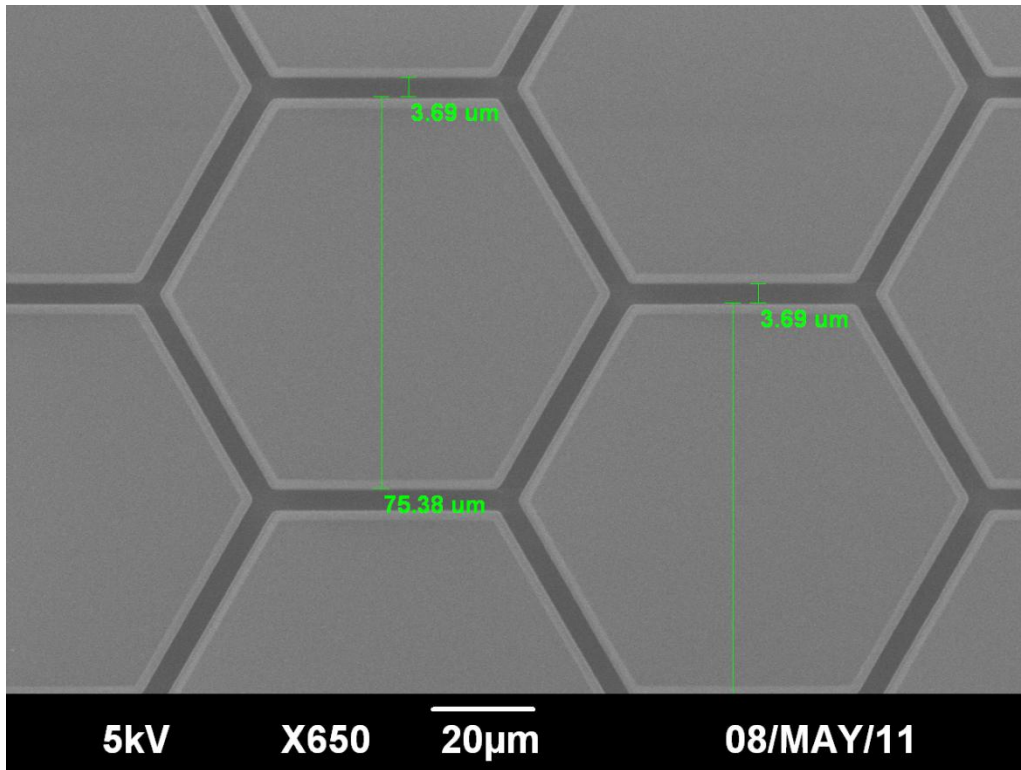


Figure A-27. 80µm cap size with 3µm spacing, plan view (2) (short)

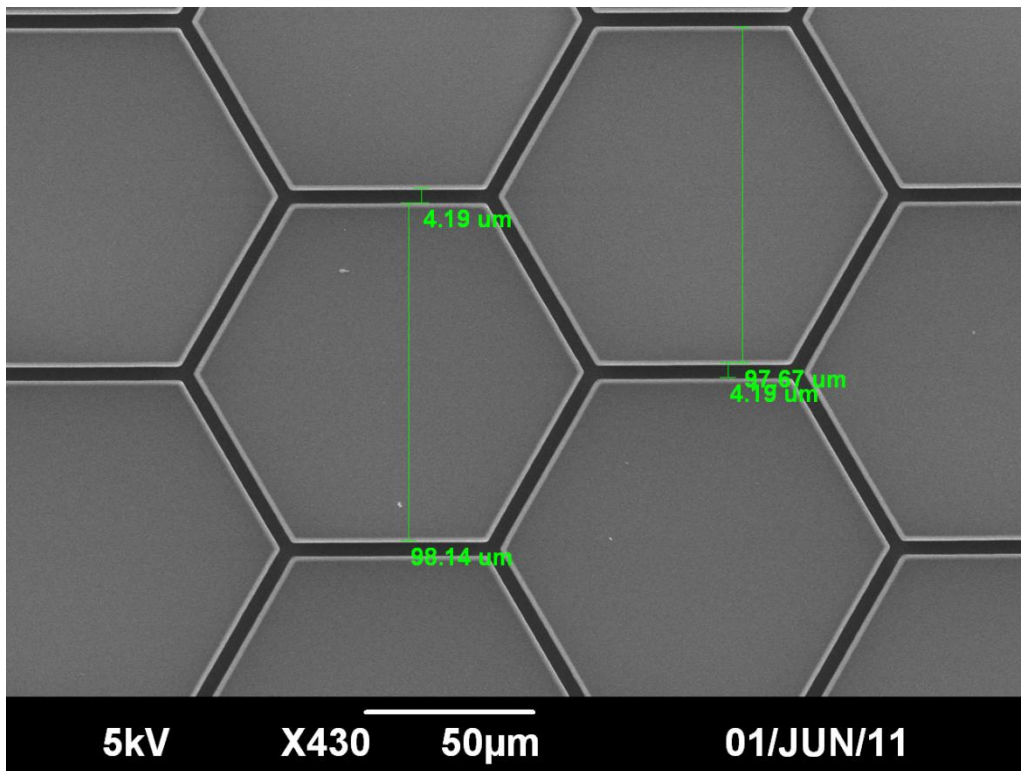


Figure A-28. 100µm cap size with 3µm spacing, plan view (standard)

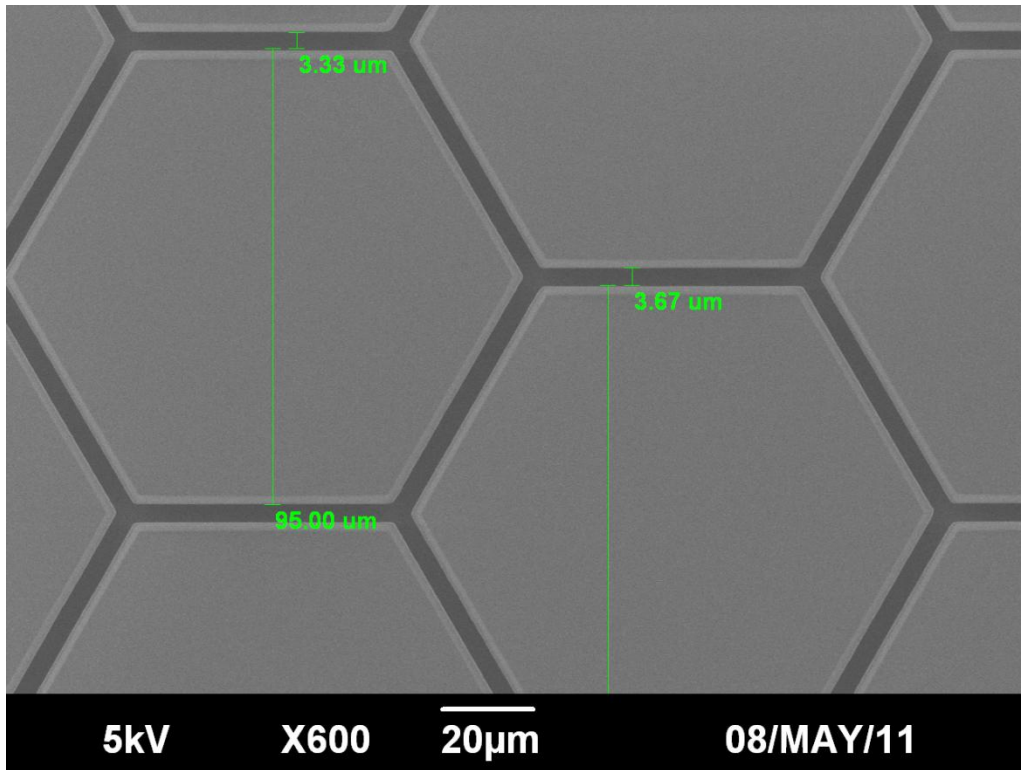


Figure A-29. 100µm cap size with 3µm spacing, plan view (2) (short)

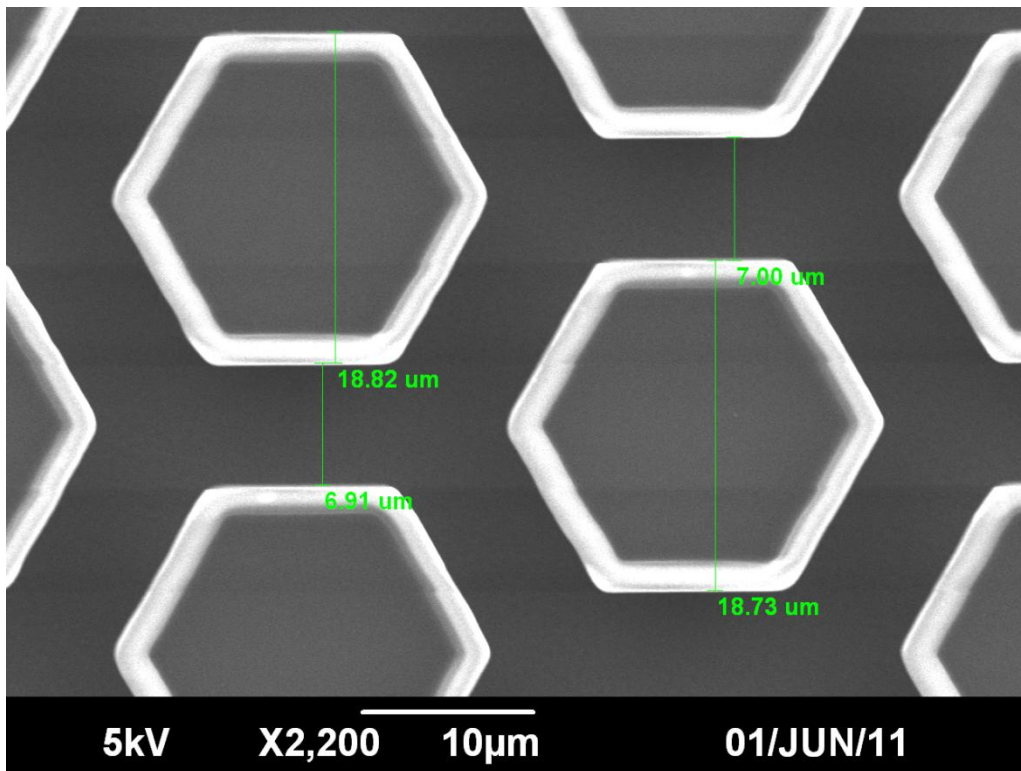


Figure A-30. 20µm cap size spaced by 6µm plan view (standard)

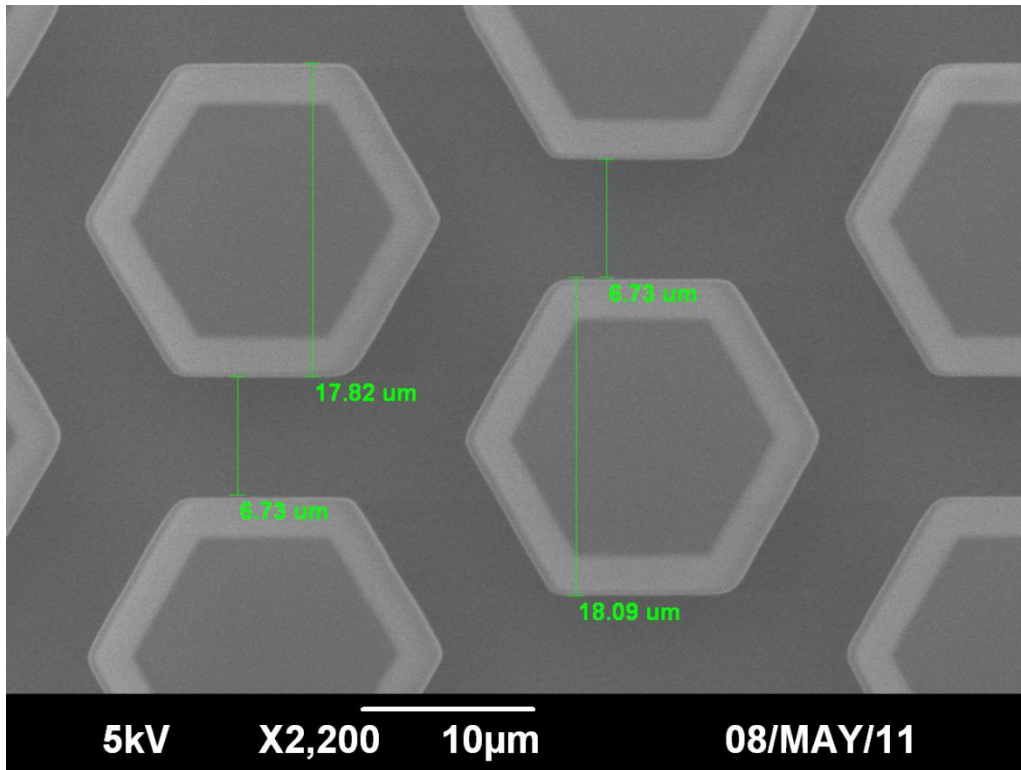


Figure A-31. 20µm cap size spaced by 6µm plan view (2) (short)

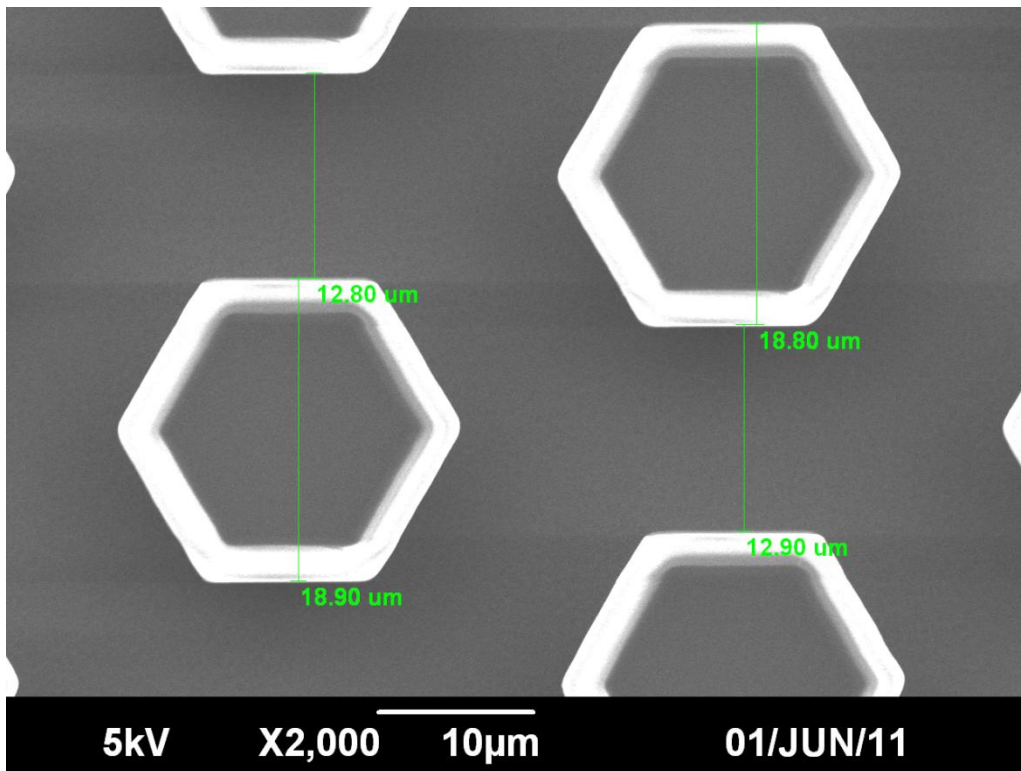


Figure A-32. 20µm cap size spaced by 12µm plan view (standard)

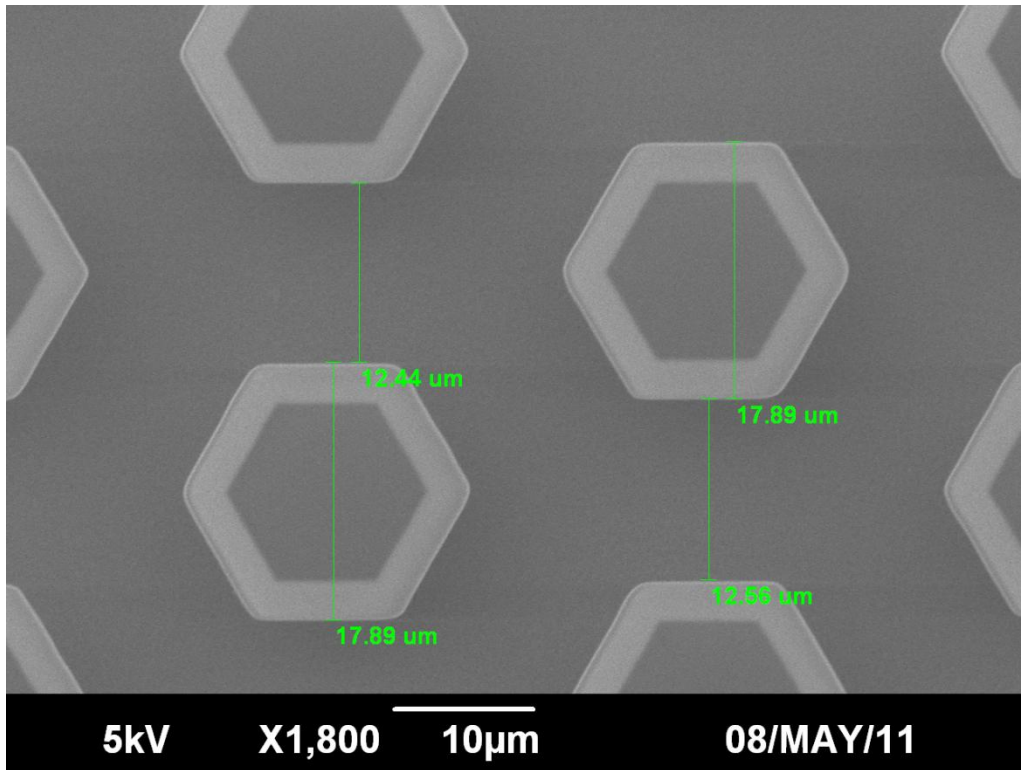


Figure A-33. 20µm cap size spaced by 12µm plan view (2) (short)

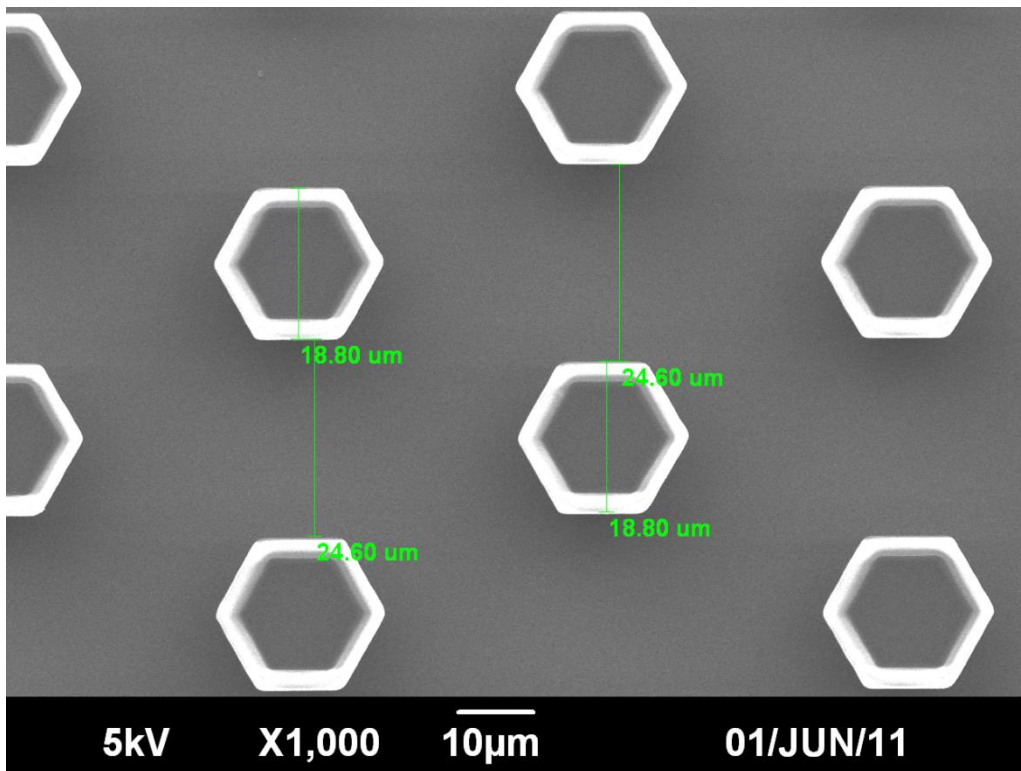


Figure A-34. 20µm cap size spaced by 24µm plan view (standard)

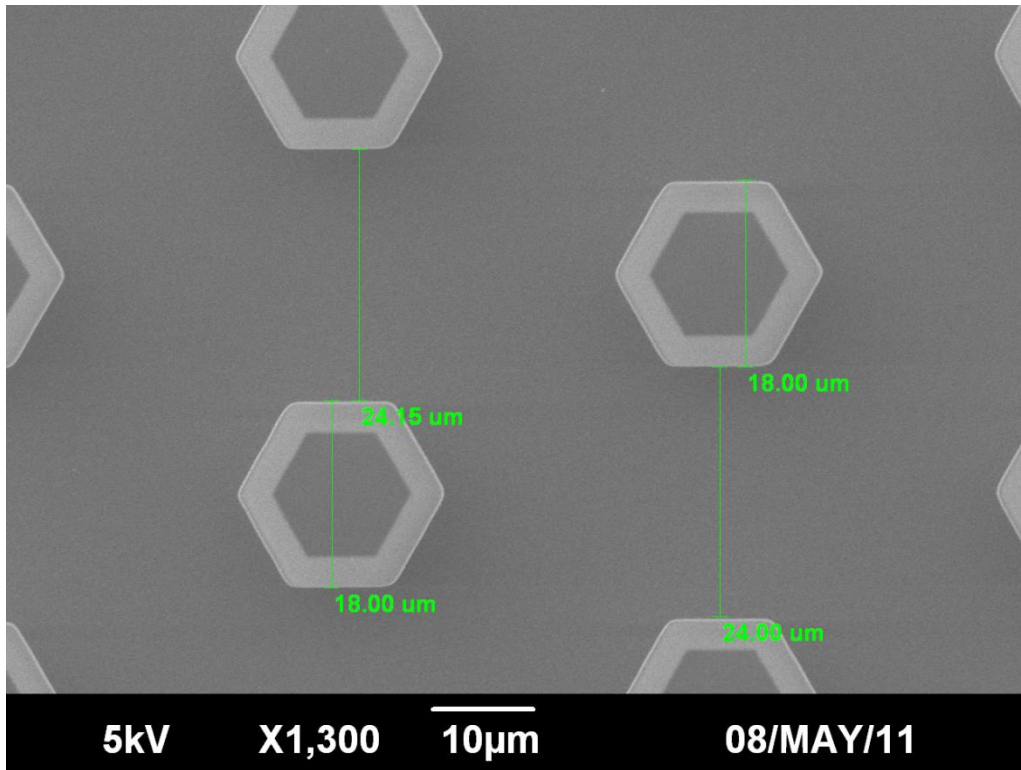


Figure A-35. 20 μ m cap size spaced by 24 μ m plan view (2) (short)

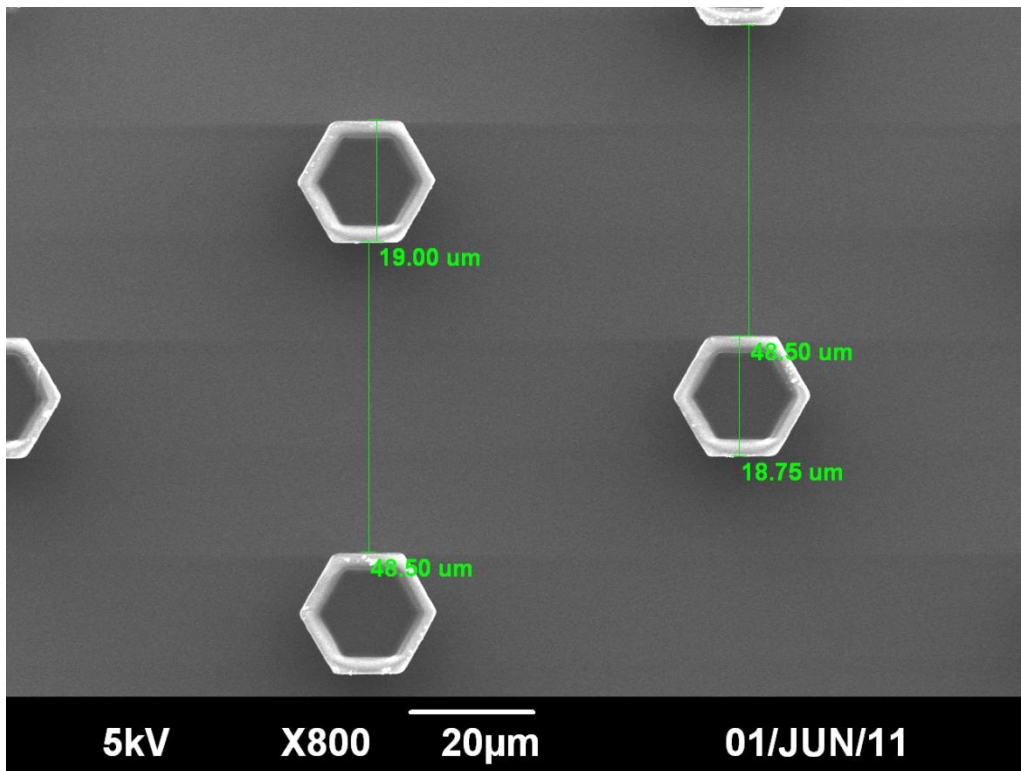


Figure A-36. 20 μ m cap size spaced by 48 μ m plan view (standard)

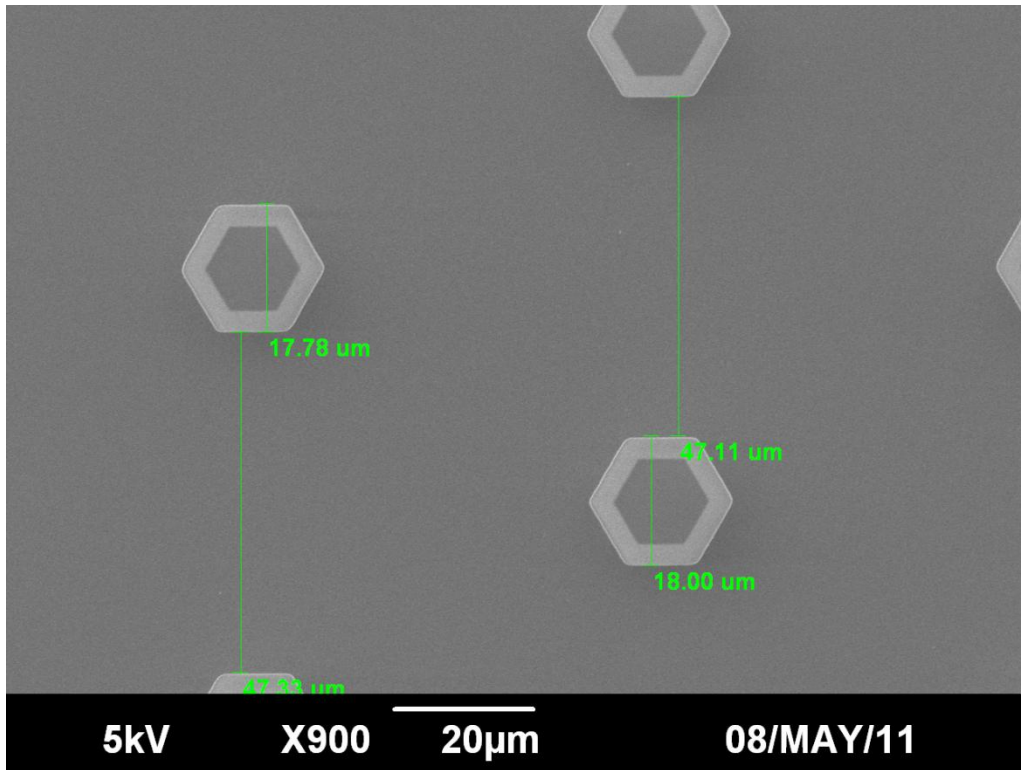


Figure A-37. 20µm cap size spaced by 48µm plan view (2) (short)

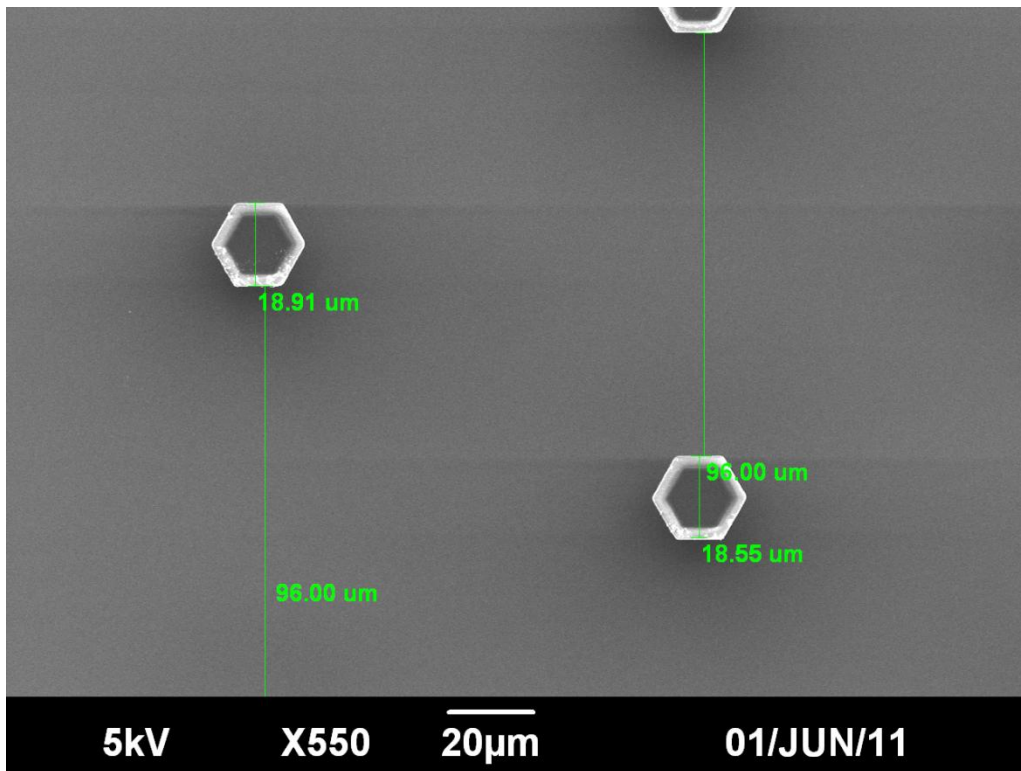


Figure A-38. 20µm cap size spaced by 96µm plan view (standard)

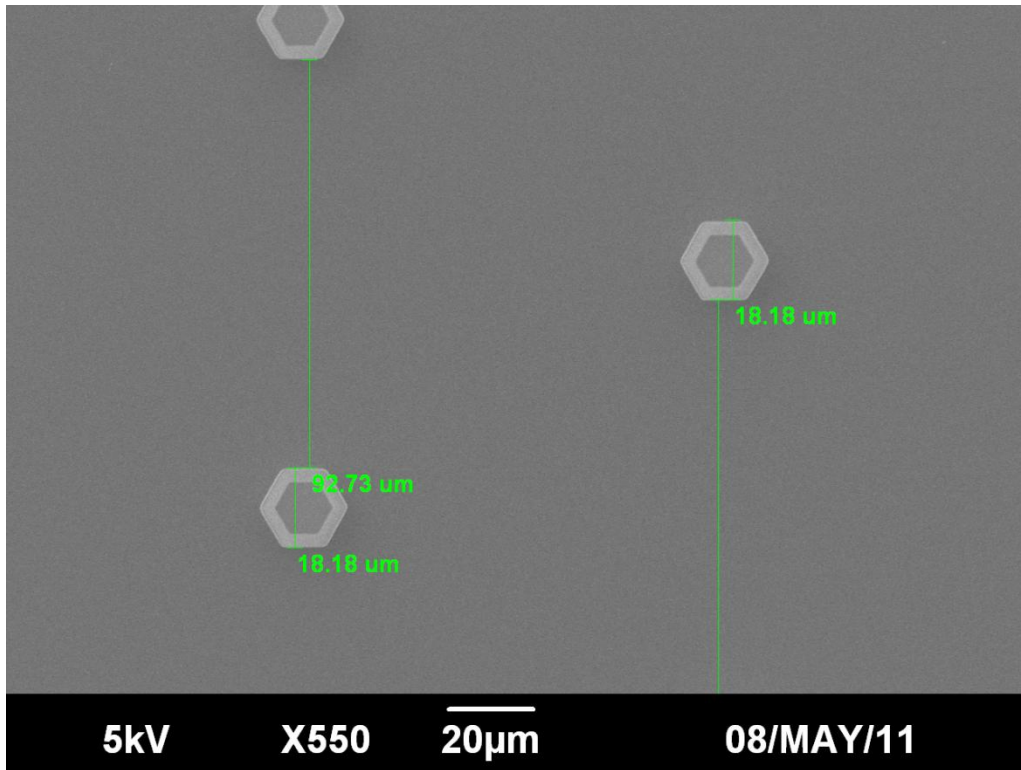


Figure A-39. 20 μ m cap size spaced by 96 μ m plan view (2) (short)

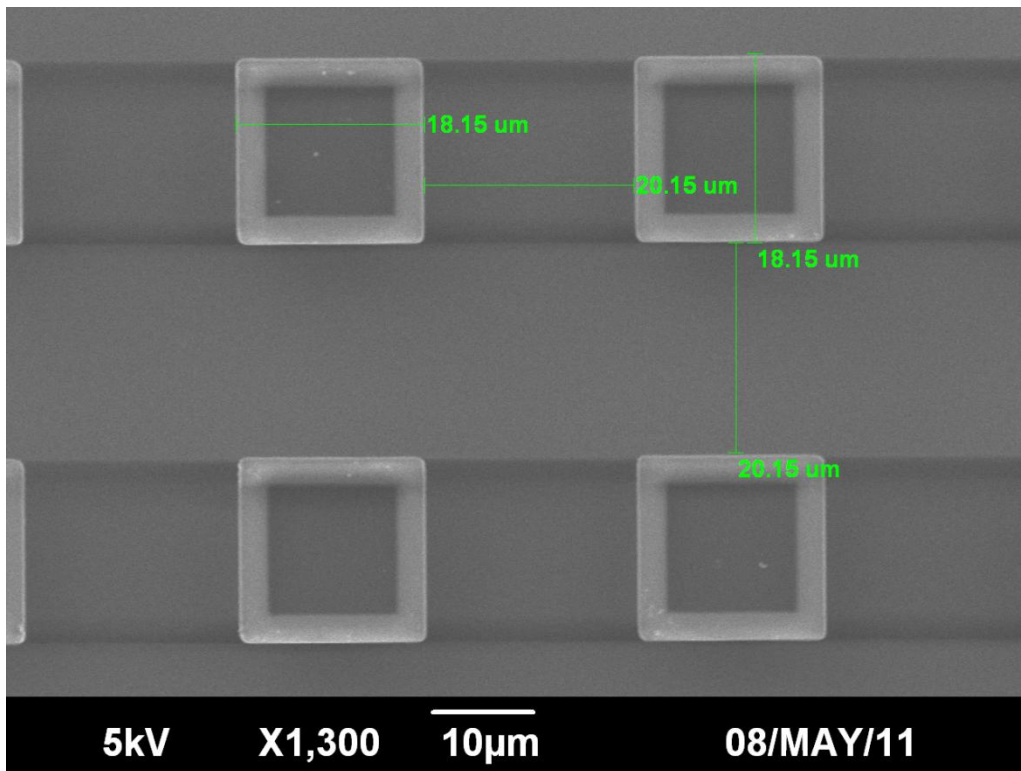


Figure A-40. Standard 20x20 μ m square cap plan view

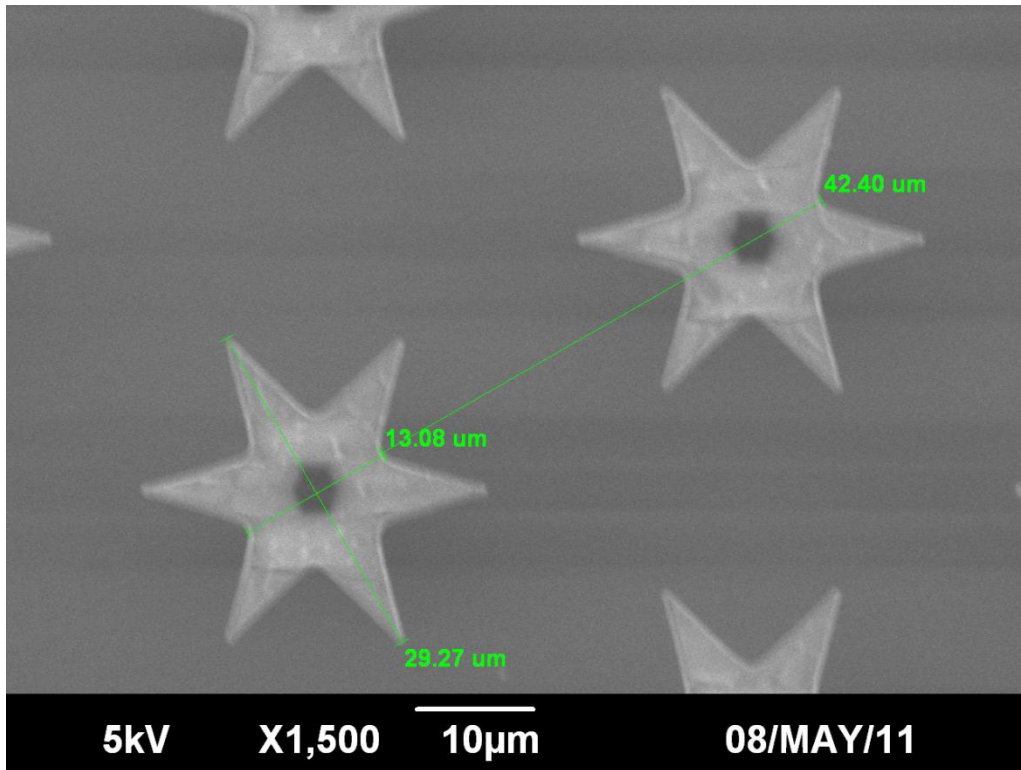


Figure A-41. Star cap plan view

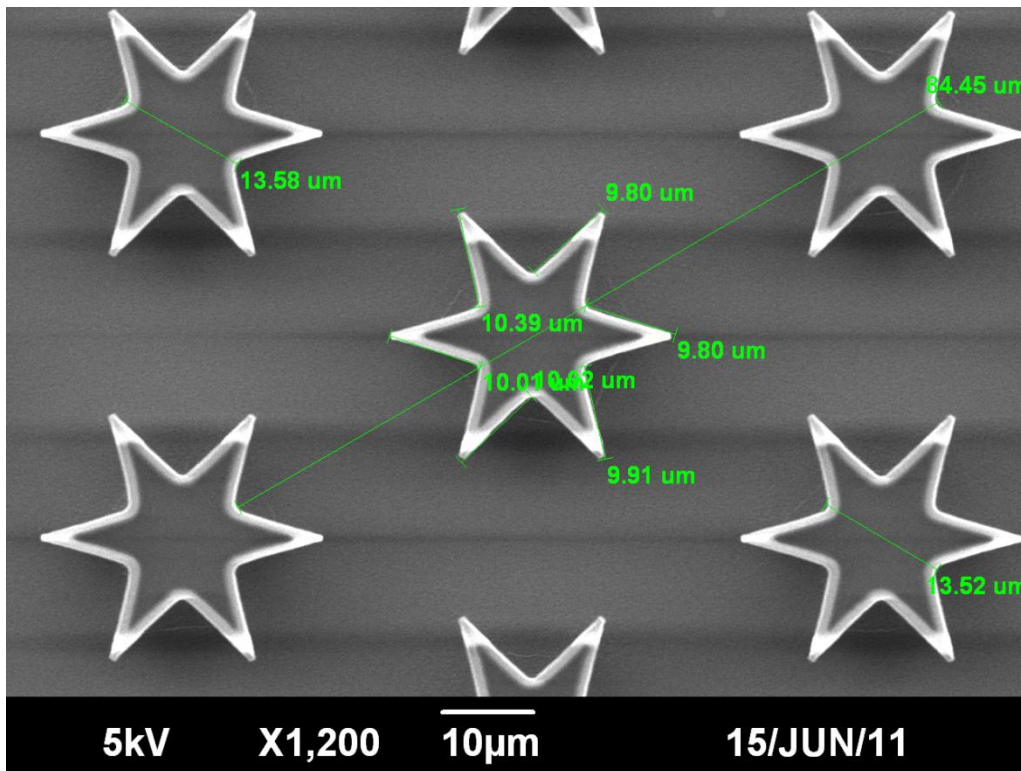


Figure A-42. Star cap plan view (2)

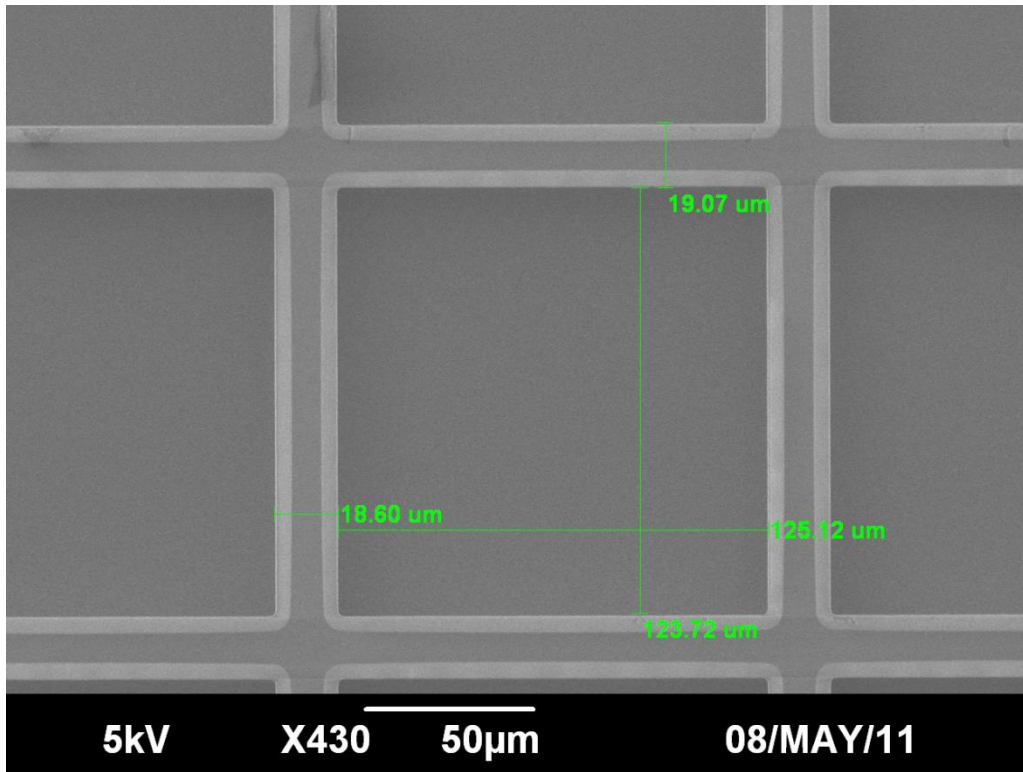


Figure A-43. Inverse pattern plan view

APPENDIX C MATLAB CODE

```
% CL_Code (v3.0)
tic;

% Input image file
[F,P]=uigetfile('*.','Select image file ...');
A=imread([P F]);
A=logical(A);
B=(A==0);
XA=size(A,1);
x=floor(XA/2); y=1;
i=x; j=y;

% Scan for nearest object
ss=50;
if A(x,y)==1
    for j=1:ss
        for i=x-ss:x+ss
            gb=B(i,j);
            if gb>0
                break
            end
        end
        if gb>0
            break
        end
    end
end
if A(i,j)==1
    error('Did not find an object')
end
x=i; y=j;

% If first object is cut off by edge
% find next in Y direction
m=y;
if y==1
    while A(x,m)==0
        m=m+1;
    end
    while A(x,m)==1
        m=m+1;
    end
    y=m;
end
```

```

k=x; l=x; m=y; n=y;

% Find the center in Y
while A(x,m)==0
    m=m-1;
end
while A(x,n)==0
    n=n+1;
end
y=floor((n-m)/2)+m;

% Find the center in X
while A(k,y)==0
    k=k-1;
end
while A(l,y)==0
    l=l+1;
end
x=floor((l-k)/2)+k;

% Kick out of Program if object
% is cut off by edge
mm=y; yy=y;
while A(x,mm)==0
    mm=mm-1;
end

% Truncate the image matrices for Y values
% less than the center of the object
A=A(:,y:end);
B=B(:,y:end);
y=1;
[XA,YA]=size(A);
dist=zeros(XA,YA);

MAX=min([x-1,XA-x,YA-y]);

% Create distance matrix and .multiply
% with the black and white image matrices
for i=1:XA
    for j=1:YA
        dist(i,j)=round(sqrt((x-i)^2+(y-j)^2));
    end
end
A=A.*dist;
B=B.*dist;

```

```

ON=zeros(1,MAX+1);
OFF=zeros(1,MAX+1);
OFF(1)=1;

% Remove zero values from image matrices
AA=(A(A>0));
AA=int16(AA(AA<=MAX));
BB=(B(B>0));
BB=int16(BB(BB<=MAX));
i=size(AA,1);
j=size(BB,1);

% Build histograms
for p=1:i
    ON(AA(p)+1)=ON(AA(p)+1)+1;
end

for q=1:j
    OFF(BB(q)+1)=OFF(BB(q)+1)+1;
end

RAT=OFF./(ON+OFF);

% Plot full graph
yl='Wetted Fraction';
xl='Radius (um)';
h=figure;
plot(RAT(1:MAX));
axis([0 MAX 0 1]);
set(gca, 'XTick', 0:1000:5000);
set(gca, 'XTickLabel', [ 0:250:1250] );
plotpub(h,xl,yl,'Current',6.5,600);

% Plot inset graph
h=figure;
plot(RAT(5000:MAX));
ylim([min(RAT(5000:MAX)) max(RAT(5000:MAX))]);
xlim([0 MAX-5000]);
set(gca, 'XTick', 0:100:500);
set(gca, 'XTickLabel', [ 1250:25:1375] );
plotpubinset(h,xl,yl,'Current_end',2.8,600);

phimin=min(RAT(5000:end))
phimax=max(RAT(5000:end))

toc

```

APPENDIX D
 Φ PLOTS

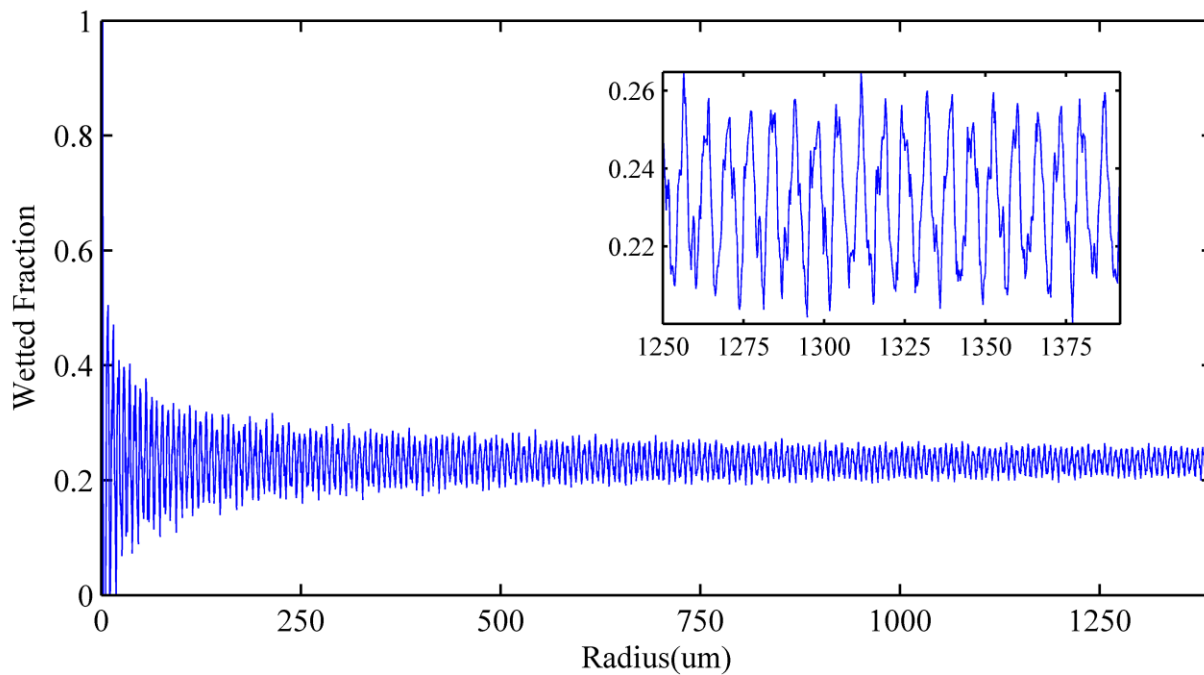


Figure B-1. 5 μ m ϕ -plot

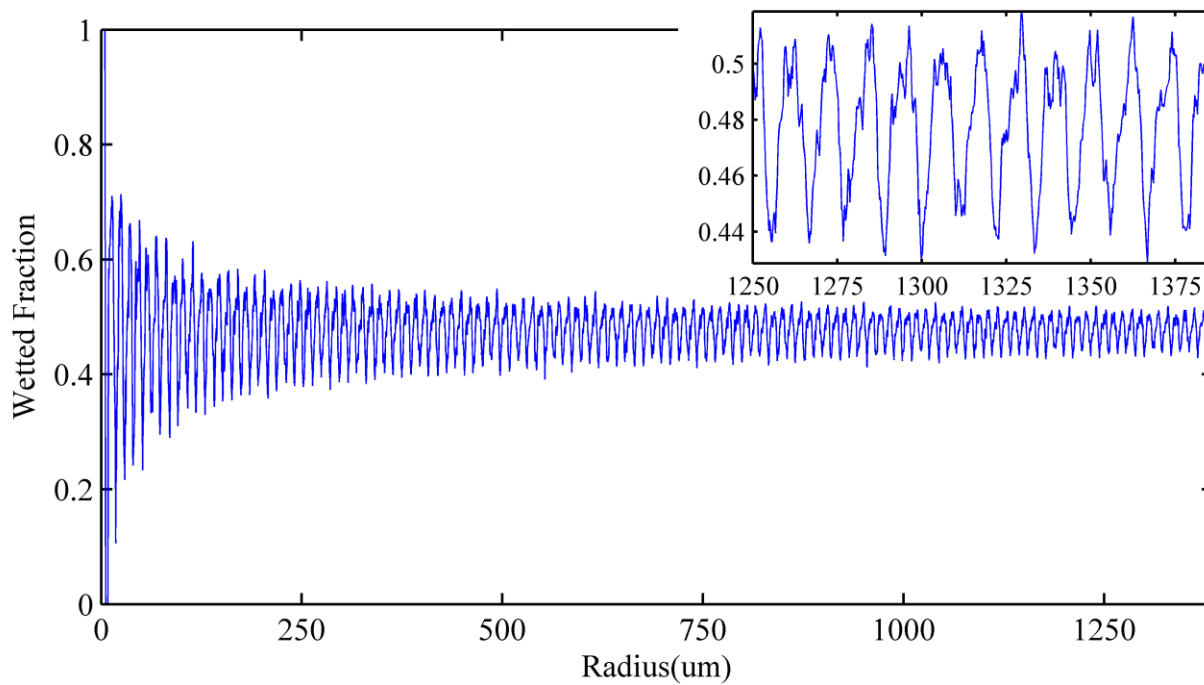


Figure B-2. 10 μ m ϕ -plot

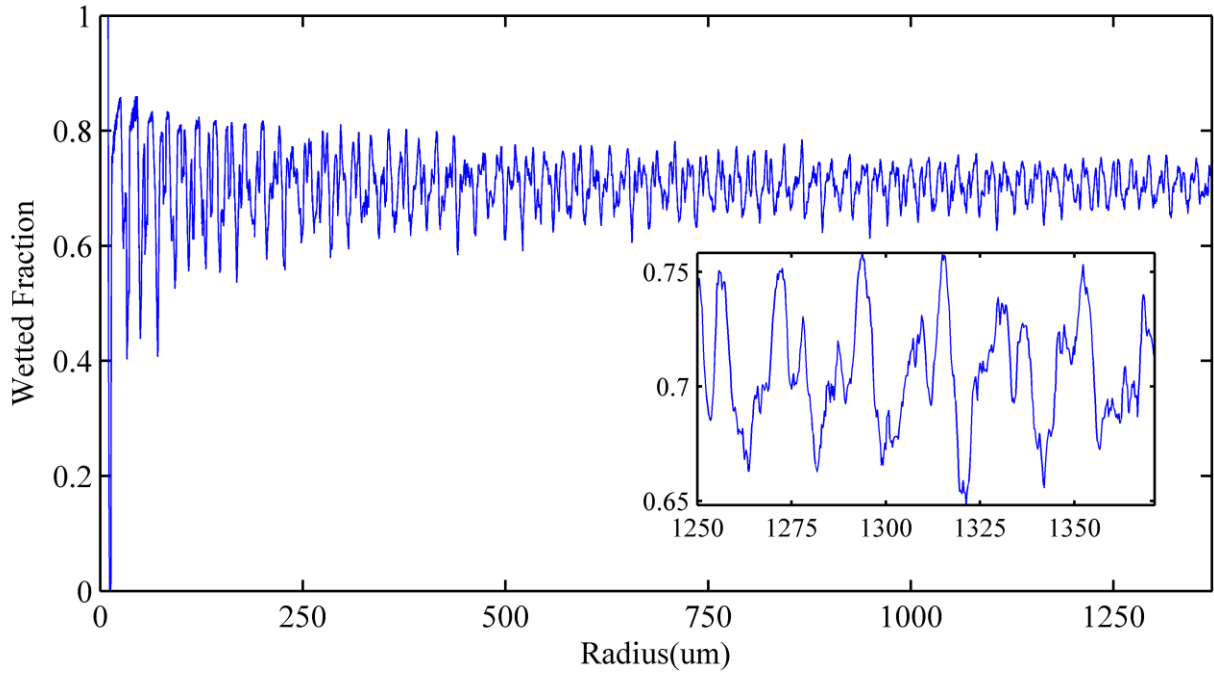


Figure B-3 20 μ m ϕ -plot

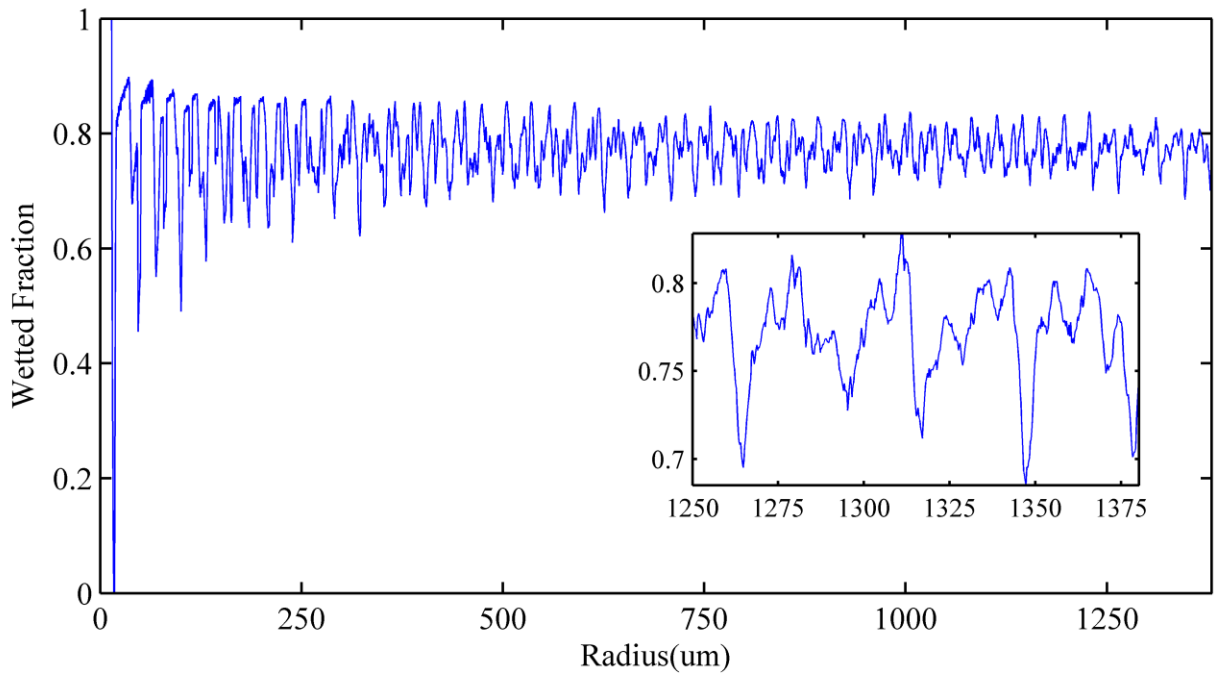


Figure B-4 30 μ m ϕ -plot

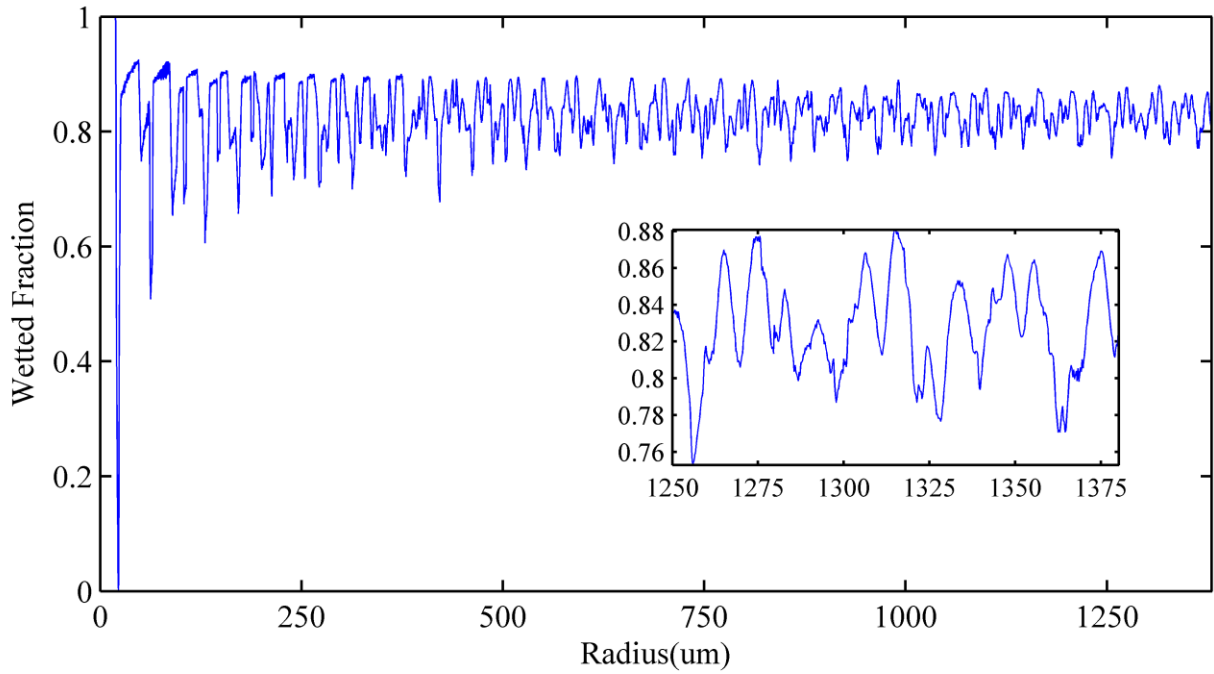


Figure B-5. 40 μ m ϕ -plot

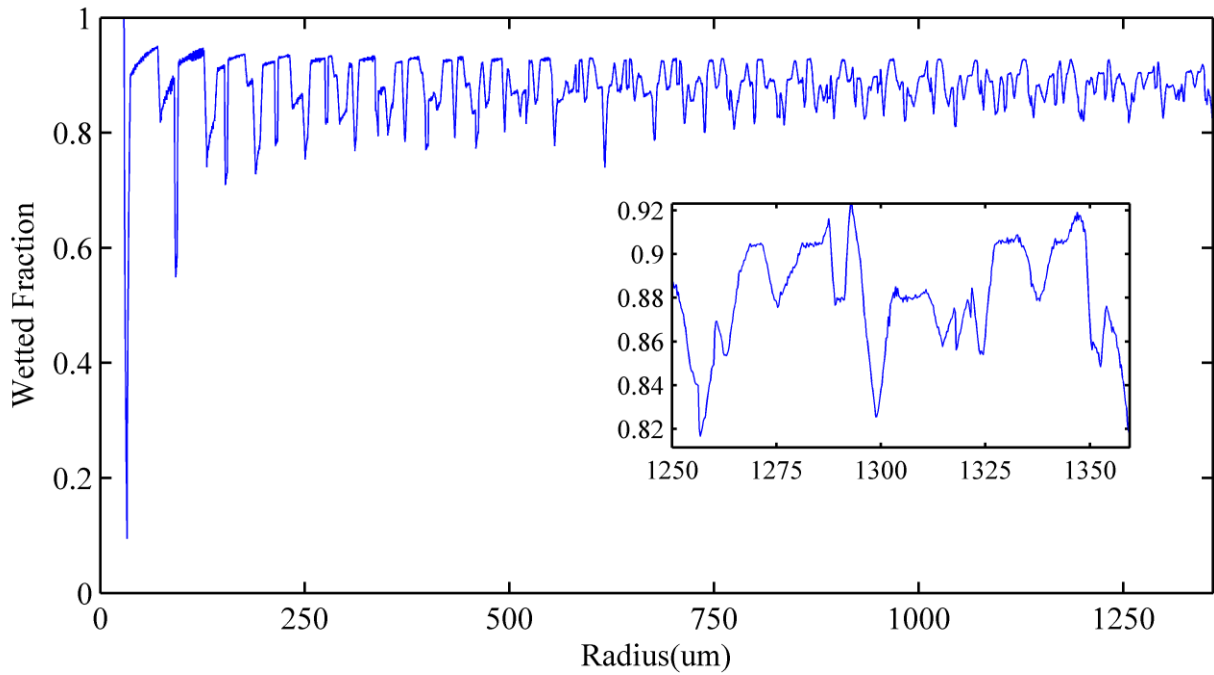


Figure B-6. 60 μ m ϕ -plot

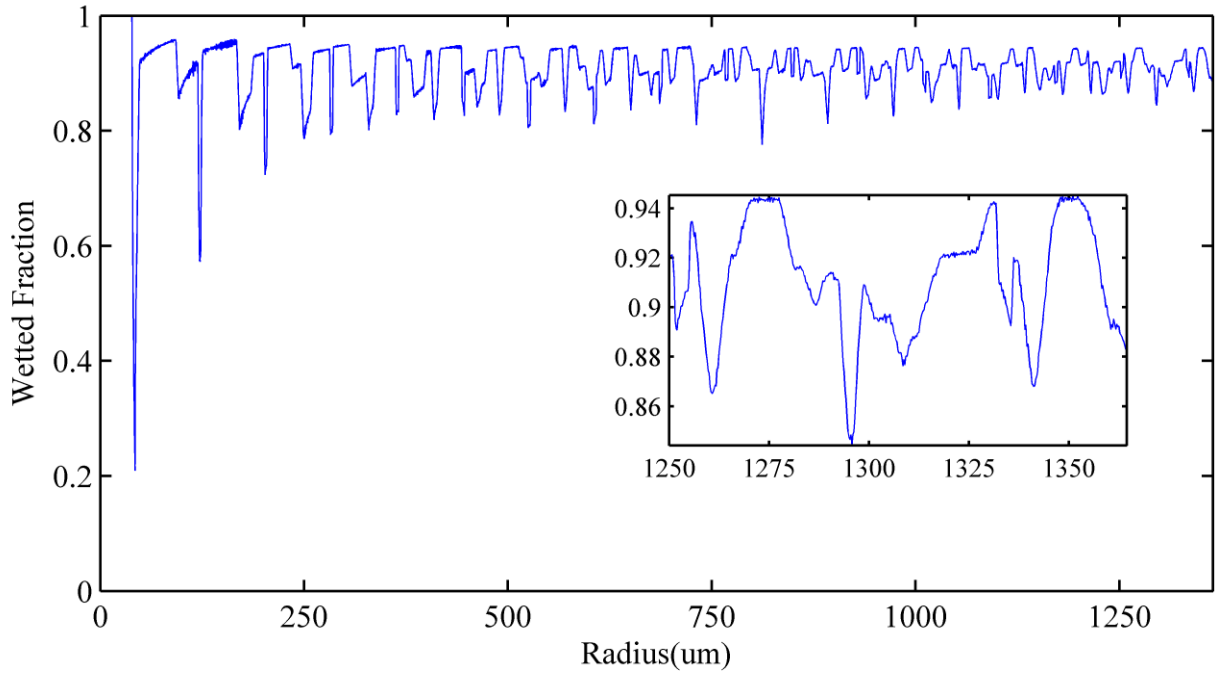


Figure B-7. 80 μ m ϕ -plot

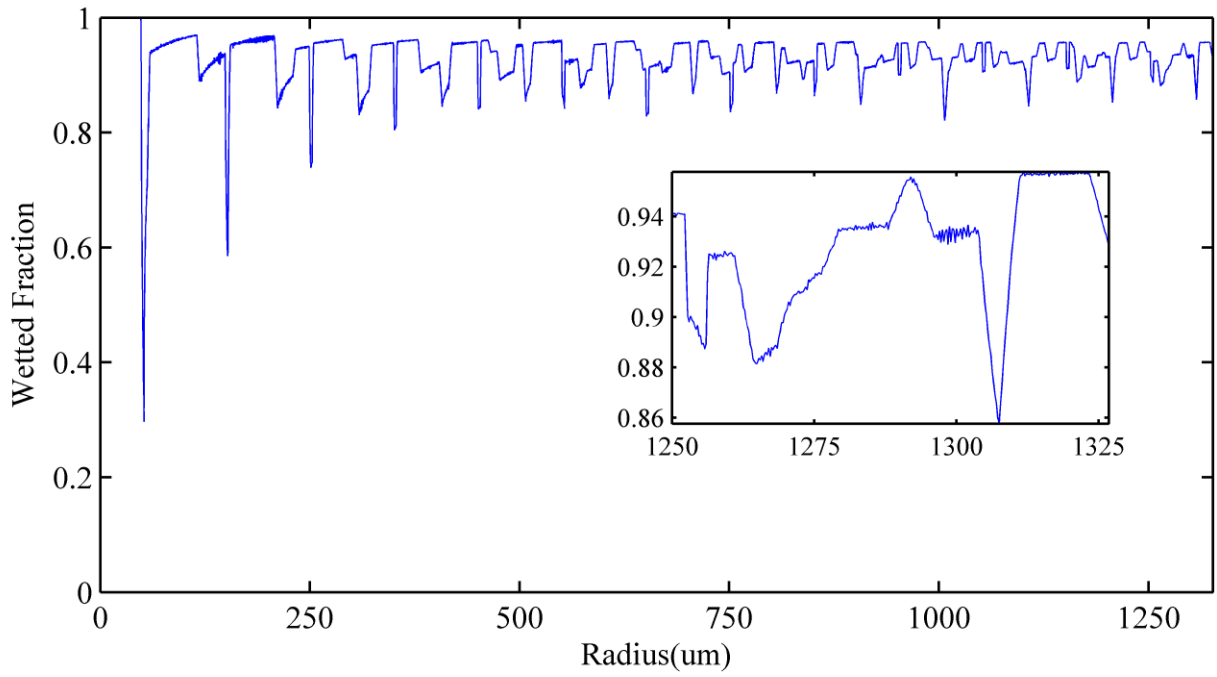


Figure B-8. 100 μ m ϕ -plot

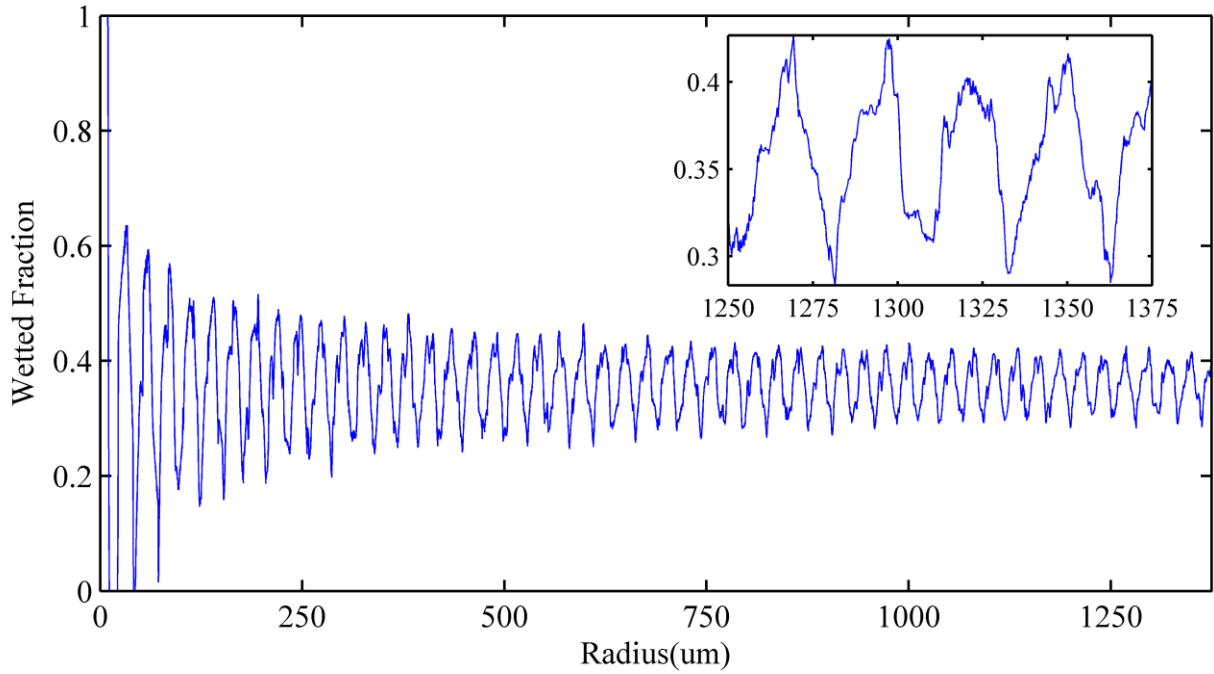


Figure B-9. 20µm cap size spaced by 12µm ϕ -plot

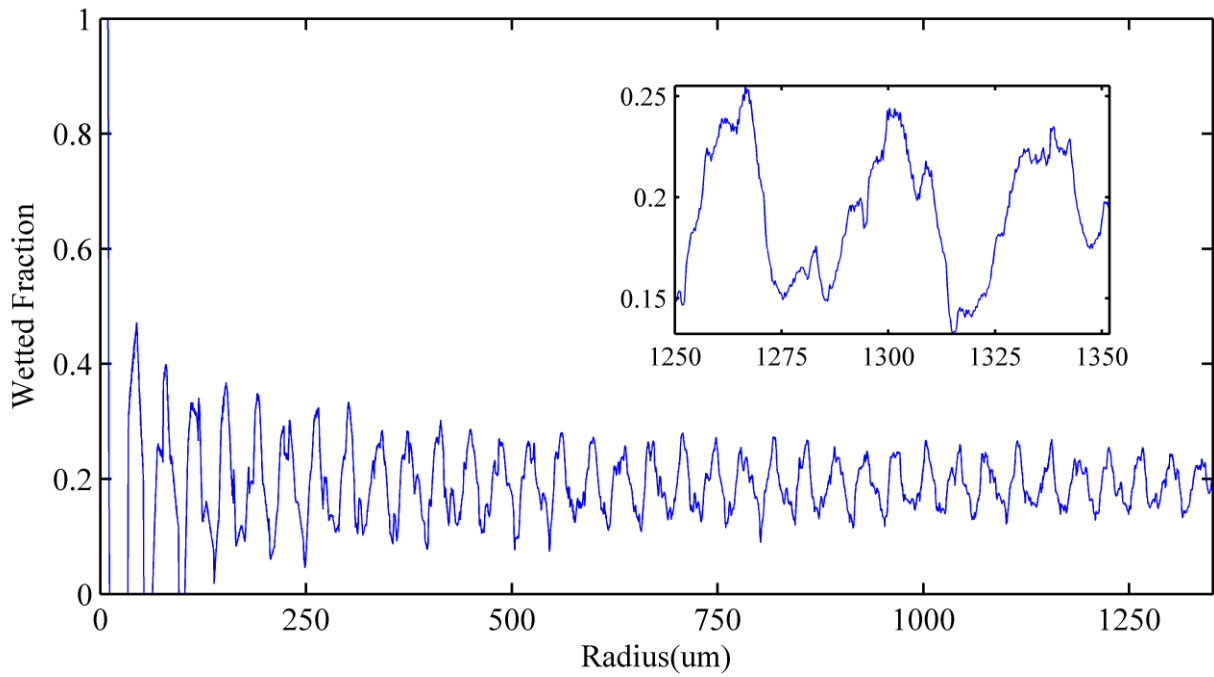


Figure B-10. 20µm cap size spaced by 24µm ϕ -plot

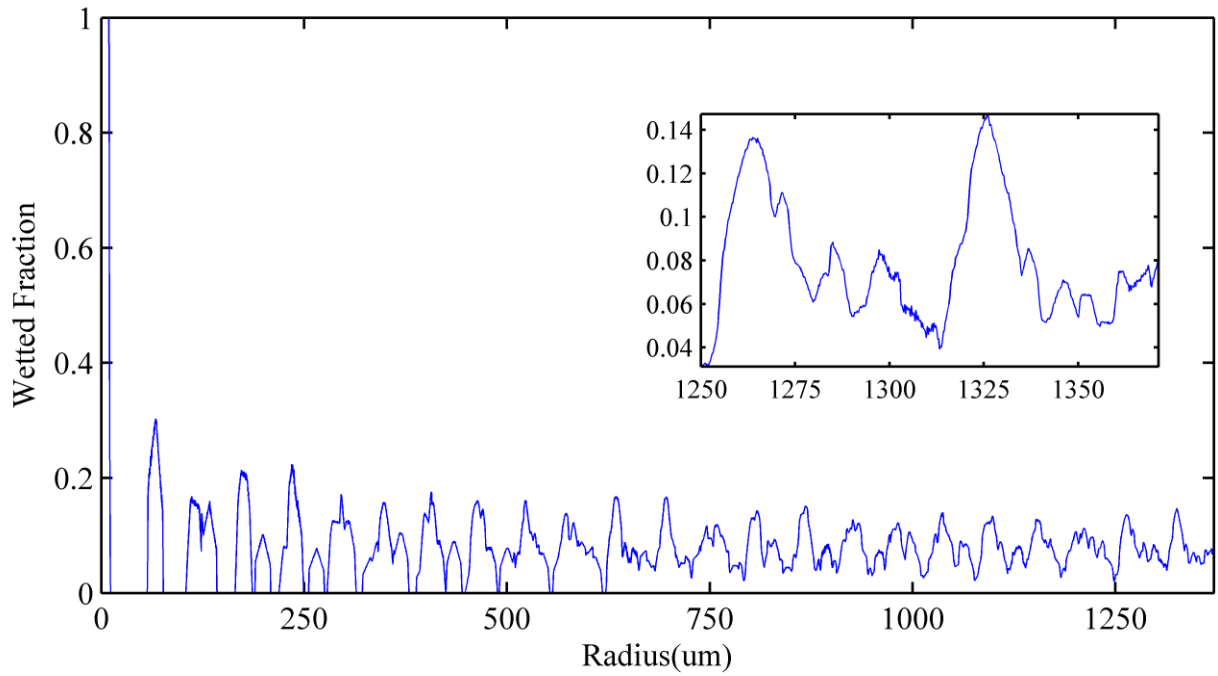


Figure B-11. 20µm cap size spaced by 48µm ϕ -plot

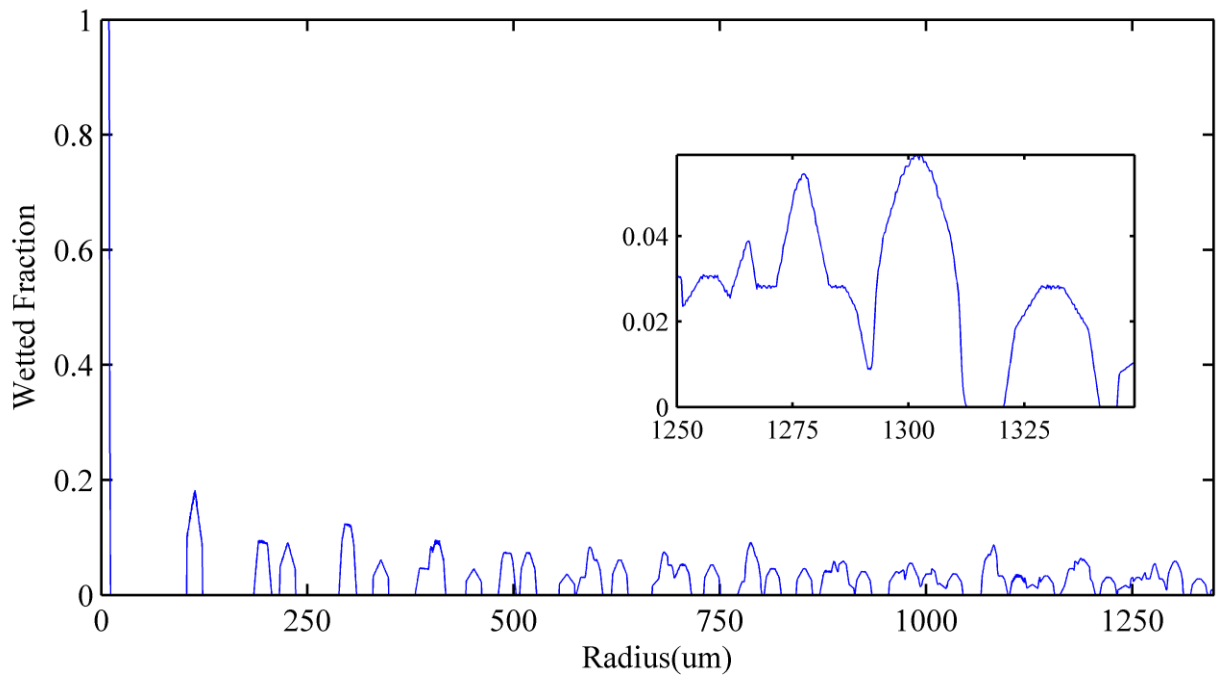


Figure B-12. 20µm cap size spaced by 96µm ϕ -plot

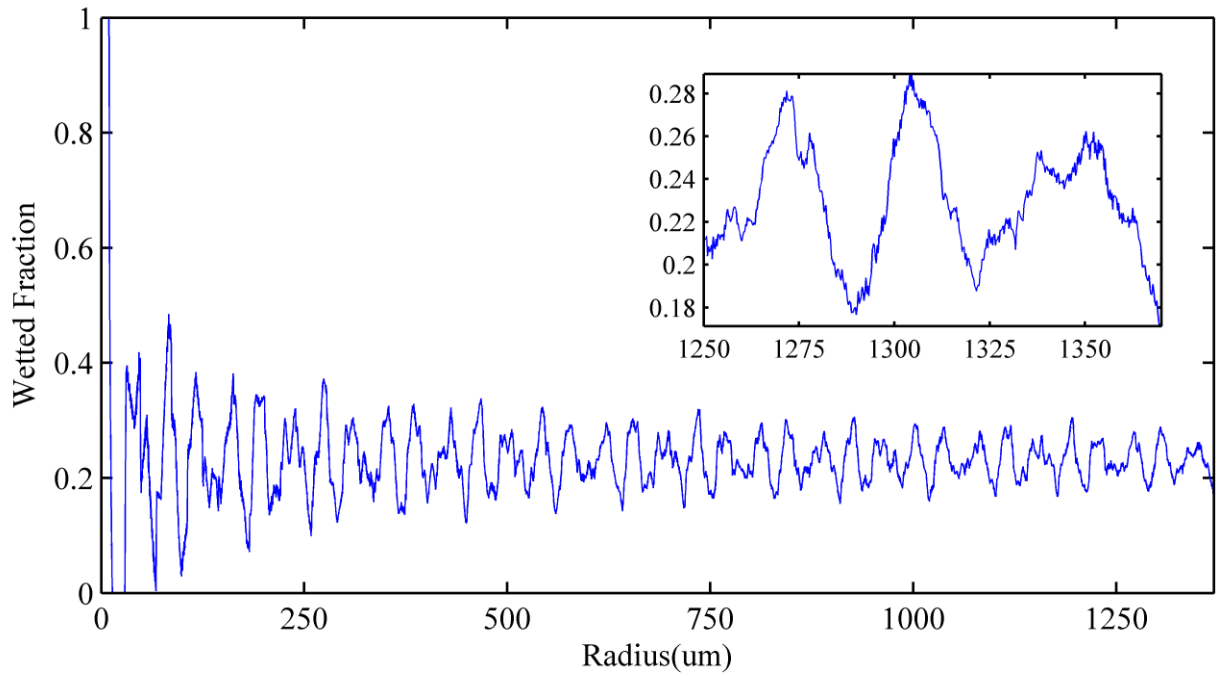


Figure B-13. 20µm cap size spaced by 20µm square ϕ -plot

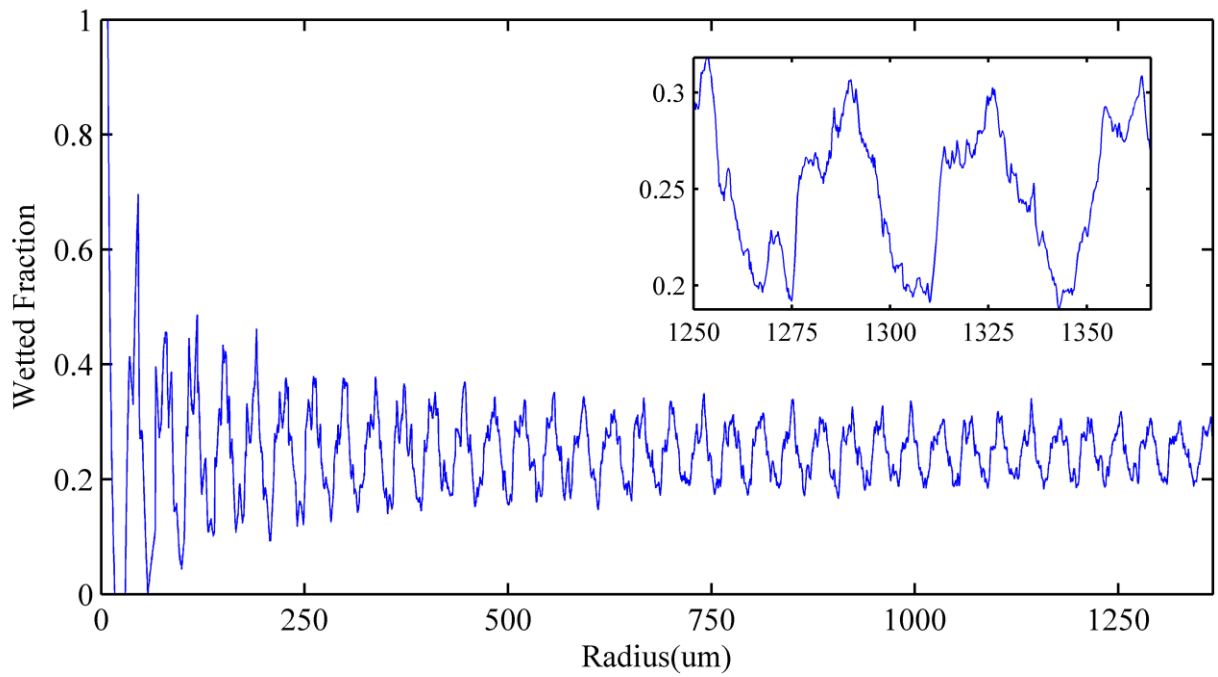


Figure B-14. 20µm cap size spaced by 24µm equivalent star ϕ -plot

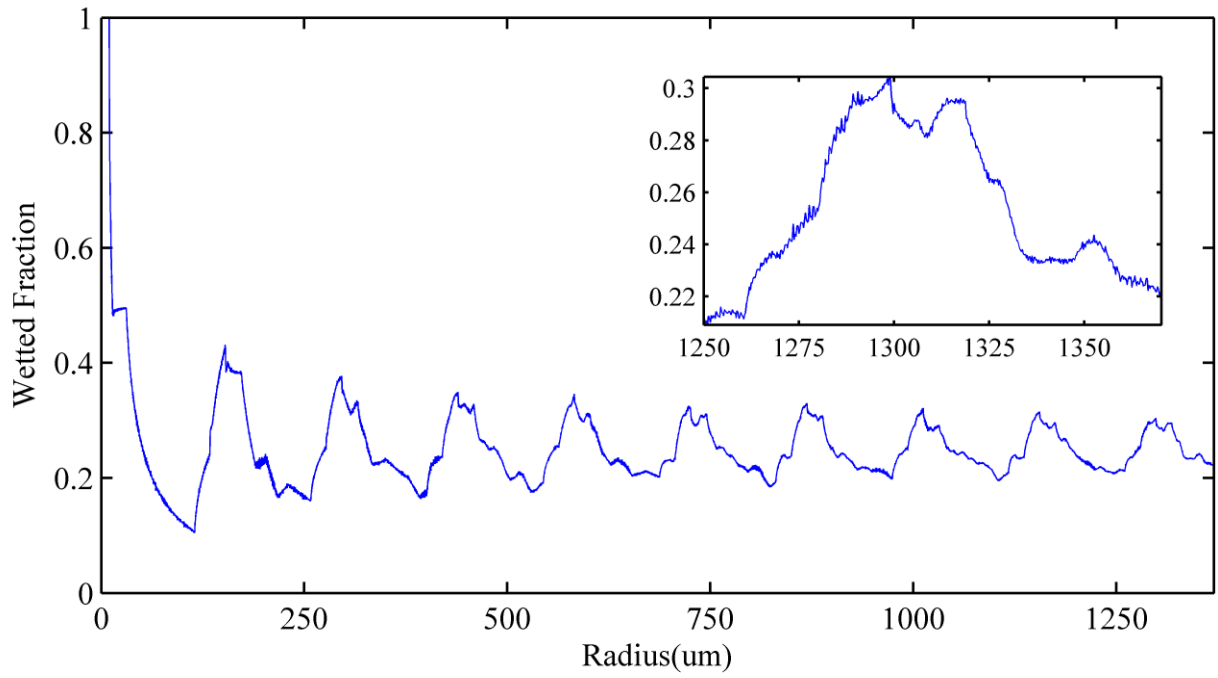


Figure B-15. 20 μ m square equivalent inverse ϕ -plot

APPENDIX E
BOILING REPRODUCIBILITY

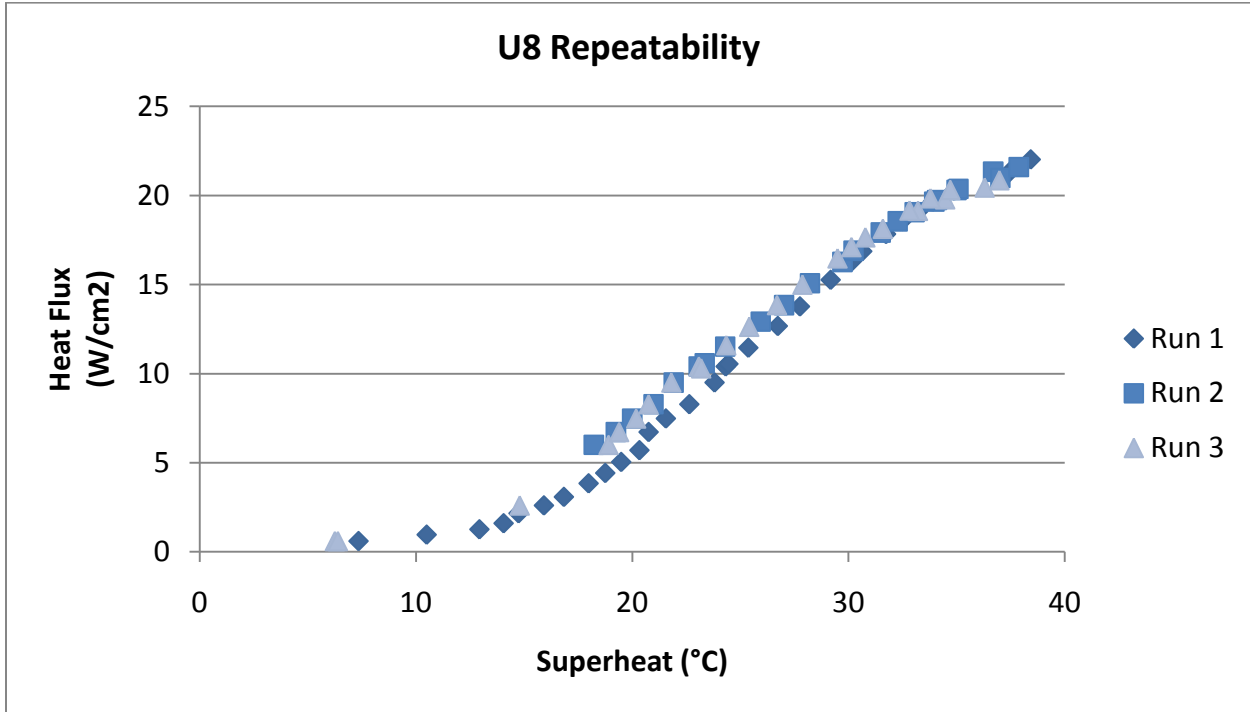


Figure D-1. Three run repeatability for the 20 μ m cap size with 300 and 500 μ m caps

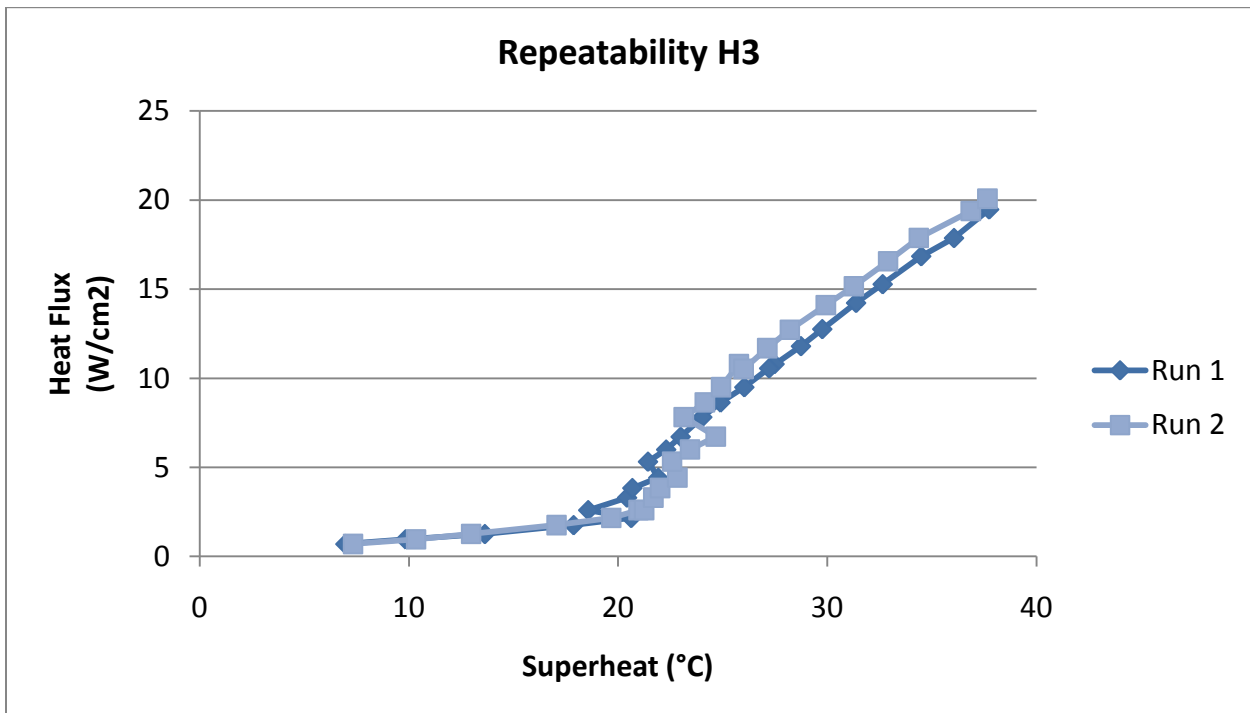


Figure D-2. Two run repeatability for the 30 μ m cap size

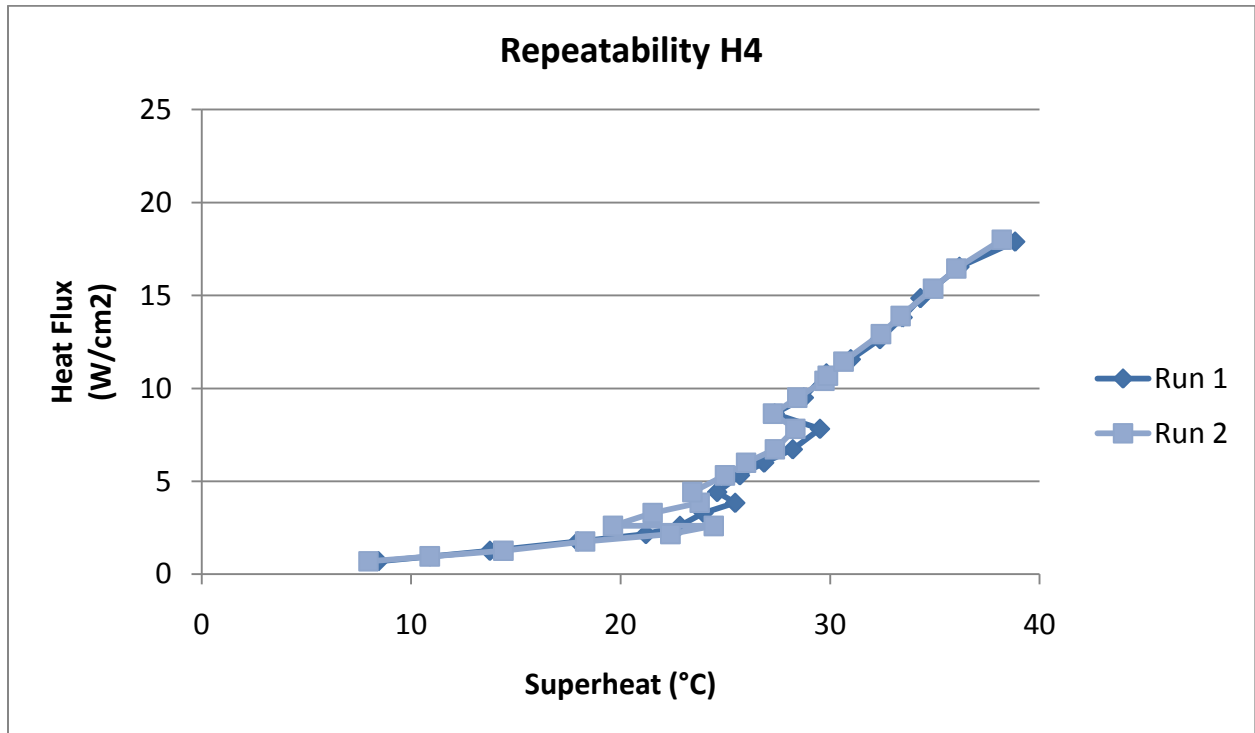


Figure D-3. Two run repeatability for the 40 μ m cap size

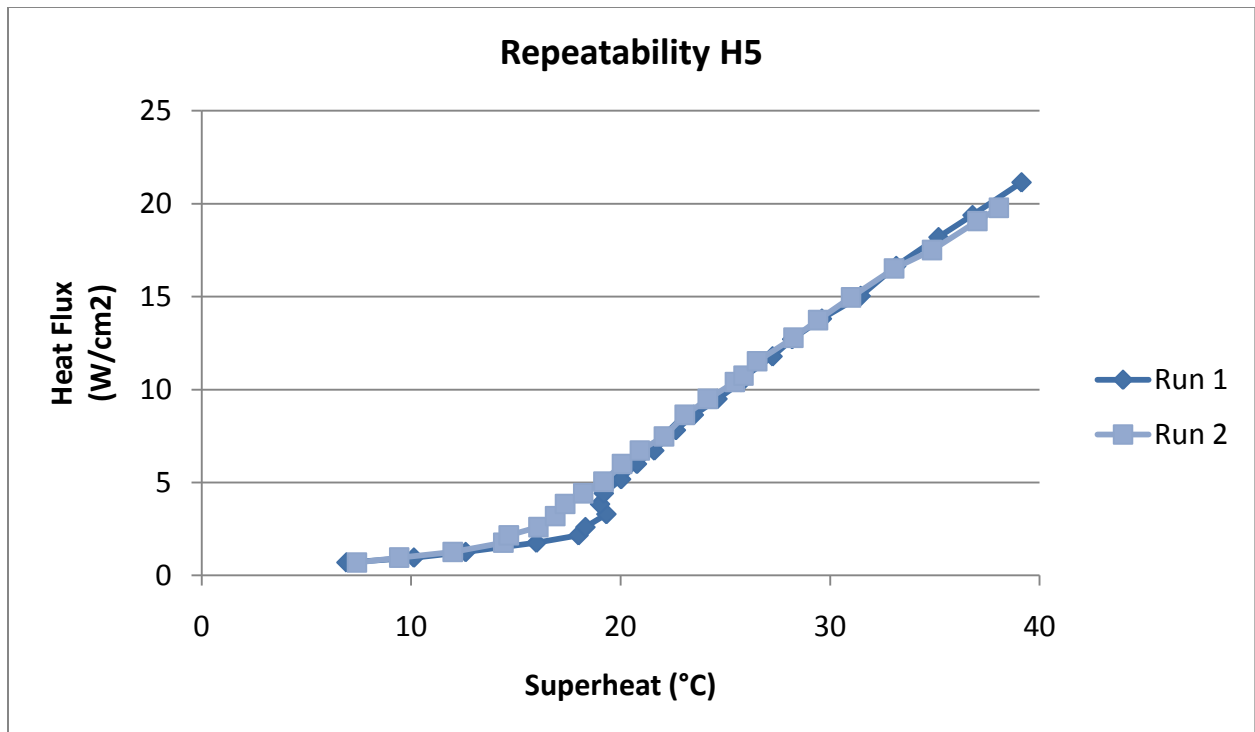


Figure D-4. Two run repeatability for the 60 μ m cap size

BIBLIOGRAPHY

- [1] Quéré D, Azzopardi MJ, Delattre L. Drops at rest on a tilted plane. *Langmuir*. 1998;14:2213-6.
- [2] Pan Q, Wang M, Wang H. Separating small amount of water and hydrophobic solvents by novel superhydrophobic copper meshes. *Applied Surface Science*. 2008;254:6002-6.
- [3] Wang C, Yao T, Wu J, Ma C, Fan Z, Wang Z, et al. Facile Approach in Fabricating Superhydrophobic and Superoleophilic Surface for Water and Oil Mixture Separation. *ACS Applied Materials & Interfaces*. 2009;1:2613-7.
- [4] Bormashenko E. Wetting transitions on biomimetic surfaces. *Philosophical Transactions of the Royal Society A: Mathematical, Physical and Engineering Sciences*. 2010;368:4695-711.
- [5] Marmur A. Super-hydrophobicity fundamentals: implications to biofouling prevention. *Biofouling*. 2006;22:107-15.
- [6] Barthlott W, Neinhuis C. Purity of the sacred lotus, or escape from contamination in biological surfaces. *Planta*. 1997;202:1-8.
- [7] Gao X, Jiang L. Biophysics: Water-repellent legs of water striders. *Nature*. 2004;432:36-.
- [8] Lee W, Jin M-K, Yoo W-C, Lee J-K. Nanostructuring of a Polymeric Substrate with Well-Defined Nanometer-Scale Topography and Tailored Surface Wettability. *Langmuir*. 2004;20:7665-9.
- [9] Cassie ABD, Baxter S. Wettability of porous surfaces. *Transactions of the Faraday Society*. 1944;40:546-51.
- [10] Wenzel RN. RESISTANCE OF SOLID SURFACES TO WETTING BY WATER. *Industrial & Engineering Chemistry*. 1936;28:988-94.
- [11] Young T. An Essay on the Cohesion of Fluids. *Philosophical Transactions of the Royal Society of London*. 1805;95:65-87.
- [12] Carey VP. Liquid-vapor phase-change phenomena 1992.
- [13] Griffith P, Wallis JD. THE ROLE OF SURFACE CONDITIONS IN NUCLEATE BOILING. Technical Report No. 14. Other Information: DSR Project No 7-7673 Orig Receipt Date: 31-DEC-591958. p. Medium: X; Size: Pages: 28.

- [14] Das AK, Das PK, Bhattacharyya S, Saha P. Nucleate boiling heat transfer from a structured surface - Effect of liquid intake. *International Journal of Heat and Mass Transfer*. 2007;50:1577-91.
- [15] Das AK, Das PK, Saha P. Performance of different structured surfaces in nucleate pool boiling. *Applied Thermal Engineering*. 2009;29:3643-53.
- [16] Pastuszko R, Poniewski ME. Semi-analytical approach to boiling heat fluxes calculation in subsurface horizontal and vertical tunnels. *International Journal of Thermal Sciences*. 2008;47:1169-83.
- [17] Chien L-H, Webb RL. A nucleate boiling model for structured enhanced surfaces. *International Journal of Heat and Mass Transfer*. 1998;41:2183-95.
- [18] Ranjan R, Murthy JY, Garimella SV. Analysis of the Wicking and Thin-Film Evaporation Characteristics of Microstructures. *Journal of Heat Transfer*. 2009;131:101001-11.
- [19] Choi W, Tuteja A, Mabry JM, Cohen RE, McKinley GH. A modified Cassie-Baxter relationship to explain contact angle hysteresis and anisotropy on non-wetting textured surfaces. *Journal of Colloid and Interface Science*. 2009;339:208-16.
- [20] Tuteja A, Choi W, Ma M, Mabry JM, Mazzella SA, Rutledge GC, et al. Designing Superoleophobic Surfaces. *Science*. 2007;318:1618-22.
- [21] Tuteja A, Choi W, Mabry JM, McKinley GH, Cohen RE. Robust omniphobic surfaces. *Proceedings of the National Academy of Sciences*. 2008;105:18200-5.
- [22] Hsu YY. ON THE SIZE RANGE OF ACTIVE NUCLEATION CAVITIES ON A HEATING SURFACE. *Journal Name: Journal of Heat Transfer (US); Journal Volume: Vol: 84; Other Information: Orig Receipt Date: 31-DEC-62. 1962:Medium: X; Size: Pages: 207-16.*
- [23] Gibbs JW, Bumstead HA, Name RGV, Longley WR. *The collected works of J. Willard Gibbs: Longmans, Green and Co.; 1902.*
- [24] Roura P, Fort J. Local thermodynamic derivation of Young's equation. *Journal of Colloid and Interface Science*. 2004;272:420-9.
- [25] Pease DC. The Significance of the Contact Angle in Relation to the Solid Surface. *The Journal of Physical Chemistry*. 1945;49:107-10.
- [26] Tadmor R. Line Energy and the Relation between Advancing, Receding, and Young Contact Angles. *Langmuir*. 2004;20:7659-64.
- [27] Cassie A. Contact angles. *Discuss Faraday Soc*. 1948;3:11-6.

- [28] Gao L, McCarthy TJ. How Wenzel and Cassie Were Wrong. *Langmuir*. 2007;23:3762-5.
- [29] Extrand CW. Model for Contact Angles and Hysteresis on Rough and Ultraphobic Surfaces. *Langmuir*. 2002;18:7991-9.
- [30] Rodríguez-Valverde MA, Montes Ruiz-Cabello FJ, Gea-Jódar PM, Kamusewitz H, Cabrerizo-Vílchez MA. A new model to estimate the Young contact angle from contact angle hysteresis measurements. *Colloids and Surfaces A: Physicochemical and Engineering Aspects*. 2010;365:21-7.
- [31] Bartell FE, Shepard JW. The effect of surface roughness on apparent contact angles and on contact angle hysteresis. I. The system Paraffin–Water–Air. *Phys Chem*. 1953;57.
- [32] Extrand CW. Contact Angles and Hysteresis on Surfaces with Chemically Heterogeneous Islands. *Langmuir*. 2003;19:3793-6.
- [33] Chen W, Fadeev AY, Hsieh MC, Öner D, Youngblood J, McCarthy TJ. Ultrahydrophobic and Ultralyophobic Surfaces: Some Comments and Examples. *Langmuir*. 1999;15:3395-9.
- [34] Gao L, McCarthy TJ. The “Lotus Effect” Explained: Two Reasons Why Two Length Scales of Topography Are Important. *Langmuir*. 2006;22:2966-7.
- [35] Gao L, McCarthy TJ. “Artificial Lotus Leaf” Prepared Using a 1945 Patent and a Commercial Textile. *Langmuir*. 2006;22:5998-6000.
- [36] Lipowsky R, Lenz P, Swain PS. Wetting and dewetting of structured and imprinted surfaces. *Colloids and Surfaces A: Physicochemical and Engineering Aspects*. 2000;161:3-22.
- [37] Öner D, McCarthy TJ. Ultrahydrophobic Surfaces. Effects of Topography Length Scales on Wettability. *Langmuir*. 2000;16:7777-82.
- [38] Youngblood JP, McCarthy TJ. Ultrahydrophobic Polymer Surfaces Prepared by Simultaneous Ablation of Polypropylene and Sputtering of Poly(tetrafluoroethylene) Using Radio Frequency Plasma. *Macromolecules*. 1999;32:6800-6.
- [39] Zhang J, Kwok DY. On the validity of the Cassie equation via a mean-field free-energy lattice Boltzmann approach. *Journal of Colloid and Interface Science*. 2005;282:434-8.
- [40] Panchagnula MV, Vedantam S. Comment on How Wenzel and Cassie Were Wrong by Gao and McCarthy. *Langmuir*. 2007;23:13242-.

- [41] Gao, McCarthy TJ. Reply to “Comment on How Wenzel and Cassie Were Wrong by Gao and McCarthy”. *Langmuir*. 2007;23:13243-.
- [42] McHale G. Cassie and Wenzel: Were They Really So Wrong? *Langmuir*. 2007;23:8200-5.
- [43] Bormashenko E. Why does the Cassie-Baxter equation apply? *Colloids and Surfaces A: Physicochemical and Engineering Aspects*. 2008;324:47-50.
- [44] Bormashenko E, Bormashenko Y, Whyman G, Pogreb R, Stanevsky O. Micrometrically scaled textured metallic hydrophobic interfaces validate the Cassie-Baxter wetting hypothesis. *Journal of Colloid and Interface Science*. 2006;302:308-11.
- [45] Nosonovsky M. On the Range of Applicability of the Wenzel and Cassie Equations. *Langmuir*. 2007;23:9919-20.
- [46] Gao L, McCarthy TJ. An Attempt to Correct the Faulty Intuition Perpetuated by the Wenzel and Cassie “Laws”. *Langmuir*. 2009;25:7249-55.
- [47] Kwon Y, Choi S, Anantharaju N, Lee J, Panchagnula MV, Patankar NA. Is the Cassie–Baxter Formula Relevant? *Langmuir*. 2010;26:17528-31.
- [48] Roach P, Shirtcliffe NJ, Newton MI. Progress in superhydrophobic surface development. *Soft Matter*. 2008;4:224-40.
- [49] Ma M, Hill RM. Superhydrophobic surfaces. *Current Opinion in Colloid & Interface Science*. 2006;11:193-202.
- [50] Crick CR, Parkin IP. Preparation and Characterisation of Super-Hydrophobic Surfaces. *Chemistry – A European Journal*. 2010;16:3568-88.
- [51] Mognetti BM, Yeomans JM. Modeling Receding Contact Lines on Superhydrophobic Surfaces. *Langmuir*. 2010;26:18162-8.
- [52] Iwamatsu M. The validity of Cassie's law: A simple exercise using a simplified model. *Journal of Colloid and Interface Science*. 2006;294:176-81.
- [53] Long J, Hyder MN, Huang RYM, Chen P. Thermodynamic modeling of contact angles on rough, heterogeneous surfaces. *Advances in Colloid and Interface Science*. 2005;118:173-90.
- [54] Anderson TM, Mudawar I. Microelectronic Cooling by Enhanced Pool Boiling of a Dielectric Fluorocarbon Liquid. *Journal of Heat Transfer*. 1989;111:752-9.
- [55] Jacob M. *Heat Transfer*. 1949:636-8.

- [56] Berenson PJ. Experiments on pool-boiling heat transfer. *International Journal of Heat and Mass Transfer*. 1962;5:985-99.
- [57] Corty C, and Foust, A. S. Surface Variables in Nucleate Boiling. *Chem Eng Prog, Symp*. 1955;51:1-12.
- [58] Kurihara HM, Myers JE. The effects of superheat and surface roughness on boiling coefficients. *AIChE Journal*. 1960;6:83-91.
- [59] Bankoff SG. Entrapment of gas in the spreading of a liquid over a rough surface. *AIChE Journal*. 1958;4:24-6.
- [60] Gaertner RF, Westwater JW. POPULATION OF ACTIVE SITES IN NUCLEATE BOILING HEAT TRANSFER. *Journal Name: Chem Eng Progr; Journal Volume: Vol: 56: Symposium Ser No 30; Other Information: Orig Receipt Date: 31-DEC-61. 1960:Medium: X; Size: Pages: 39-48.*
- [61] Clark HB, Strenge PS, Westwater JW. ACTIVE SITES FOR NUCLEATE BOILING. *Journal Name: Chem Eng Progr; Journal Volume: Vol: 55, Symposium Ser No 29; Other Information: Orig Receipt Date: 31-DEC-60. 1959:Medium: X; Size: Pages: 103-10.*
- [62] Benjamin JE, Westwater JW. Bubble growth in nucleate boiling of binary mixture. *International Developments in Heat Transfer*. 1961:212-8.
- [63] Nakayama W, Daikoku T, Kuwahara H, Nakajima T. Dynamic Model of Enhanced Boiling Heat Transfer on Porous Surfaces---Part I: Experimental Investigation. *Journal of Heat Transfer*. 1980;102:445-50.
- [64] Nakayama W, Daikoku T, Nakajima T. Effects of Pore Diameters and System Pressure on Saturated Pool Nucleate Boiling Heat Transfer From Porous Surfaces. *Journal of Heat Transfer*. 1982;104:286-91.
- [65] Webb RL. Donald Q. Kern Lecture Award Paper: Odyssey of the Enhanced Boiling Surface. *Journal of Heat Transfer*. 2004;126:1051-9.
- [66] Piroo IL, Rohsenow W, Doerffer SS. Nucleate pool-boiling heat transfer. I: review of parametric effects of boiling surface. *International Journal of Heat and Mass Transfer*. 2004;47:5033-44.
- [67] Piroo IL, Rohsenow W, Doerffer SS. Nucleate pool-boiling heat transfer. II: assessment of prediction methods. *International Journal of Heat and Mass Transfer*. 2004;47:5045-57.

- [68] Ramaswamy C, Joshi Y, Nakayama W, Johnson WB. Effects of Varying Geometrical Parameters on Boiling From Microfabricated Enhanced Structures. *Journal of Heat Transfer*. 2003;125:103-9.
- [69] Reed SJ, Mudawar I. Elimination of boiling incipience temperature drop in highly wetting fluids using spherical contact with a flat surface. *International Journal of Heat and Mass Transfer*. 1999;42:2439-54.
- [70] Messina AD, Park Jr EL. Effects of precise arrays of pits on nucleate boiling. *International Journal of Heat and Mass Transfer*. 1981;24:141-5.
- [71] Miller WJ, Gebhart B, Wright NT. Effects of boiling history on a microconfigured surface in a dielectric liquid. *International Communications in Heat and Mass Transfer*. 1990;17:389-98.
- [72] Goyal A, Jaeger RC, Bhavnani SH, Ellis CD, Phadke NK, Azimi-Rashti M, et al. Re-entrant cavity heat sinks formed by anisotropic etching and silicon direct wafer bonding. *Semiconductor Thermal Measurement and Management Symposium, 1992 SEMI-THERM VIII, Eighth Annual IEEE1992*. p. 25-9.
- [73] Honda H, Takamastu H, Wei J. Enhanced boiling of FC-72 on silicon chips with micro-pin-fins and submicron-scale roughness. *Journal of Heat Transfer*. 2002;124:383.
- [74] Honda H, Wei JJ. Enhanced boiling heat transfer from electronic components by use of surface microstructures. *Experimental Thermal and Fluid Science*. 2004;28:159-69.
- [75] Bhavnani SH, Fournelle G, Jaeger RC. Immersion-cooled heat sinks for electronics: insight from high-speed photography. *Components and Packaging Technologies, IEEE Transactions on*. 2001;24:166-76.
- [76] Garimella SV, Fleischer AS, Murthy JY, Keshavarzi A, Prasher R, Patel C, et al. Thermal Challenges in Next-Generation Electronic Systems. *Components and Packaging Technologies, IEEE Transactions on*. 2008;31:801-15.
- [77] Jones RJ, Pate DT, Bhavnani SH. Control of Instabilities in Two-Phase Microchannel Flow Using Artificial Nucleation Sites. *ASME Conference Proceedings*. 2007;2007:347-58.
- [78] Nimkar ND, Bhavnani SH, Jaeger RC. Effect of nucleation site spacing on the pool boiling characteristics of a structured surface. *International Journal of Heat and Mass Transfer*. 2006;49:2829-39.
- [79] Pate DT, Jones RJ, Bhavnani SH. Cavity-induced two-phase heat transfer in silicon microchannels. *Thermal and Thermomechanical Phenomena in Electronics Systems, 2006 ITherm '06 The Tenth Intersociety Conference on*2006. p. 8 pp.-78.

- [80] Chen Y, Mo D, Zhao H, Ding N, Lu S. Pool boiling on the superhydrophilic surface with TiO₂ nanotube arrays. *Science in China Series E: Technological Sciences*. 2009;52:1596-600.
- [81] Mitrovic J, Hartmann F. A new microstructure for pool boiling. *Superlattices and Microstructures*. 2004;35:617-28.
- [82] Ujereh S, Fisher T, Mudawar I. Effects of carbon nanotube arrays on nucleate pool boiling. *International Journal of Heat and Mass Transfer*. 2007;50:4023-38.
- [83] Launay S, Fedorov AG, Joshi Y, Cao A, Ajayan PM. Hybrid micro-nano structured thermal interfaces for pool boiling heat transfer enhancement. *Microelectronics Journal*. 2006;37:1158-64.
- [84] Arik M, Bar-Cohen A, You SM. Enhancement of pool boiling critical heat flux in dielectric liquids by microporous coatings. *International Journal of Heat and Mass Transfer*. 2007;50:997-1009.
- [85] Chang JY, You SM. Boiling heat transfer phenomena from microporous and porous surfaces in saturated FC-72. *International Journal of Heat and Mass Transfer*. 40:4437-47.
- [86] Chang JY, You SM. Enhanced boiling heat transfer from microporous surfaces: effects of a coating composition and method. *International Journal of Heat and Mass Transfer*. 40:4449-60.
- [87] El-Genk MS, Parker JL. Enhanced boiling of HFE-7100 dielectric liquid on porous graphite. *Energy Conversion and Management*. 2005;46:2455-81.
- [88] Parker JL, El-Genk MS. Enhanced saturation and subcooled boiling of FC-72 dielectric liquid. *International Journal of Heat and Mass Transfer*. 2005;48:3736-52.
- [89] Wei JJ, Honda H. Effects of fin geometry on boiling heat transfer from silicon chips with micro-pin-fins immersed in FC-72. *International Journal of Heat and Mass Transfer*. 2003;46:4059-70.
- [90] O'Connor JP, You SM, Chang JY. Gas-Saturated Pool Boiling Heat Transfer From Smooth and Microporous Surfaces in FC-72. *Journal of Heat Transfer*. 1996;118:662-7.

BIOGRAPHICAL SKETCH

Edward McKenna received his bachelor's degree in chemical engineering from the University of Florida in December of 2004. He then went to work for Terronics, a small company in Indiana, designing electro hydrodynamic atomization nozzles until the fall of 2005. Edward received his master's degree in materials science and engineering from the University of Florida in August of 2007. He received his Ph.D. from the University of Florida in the summer of 2011.